

PDF hosted at the Radboud Repository of the Radboud University Nijmegen

The following full text is a publisher's version.

For additional information about this publication click this link.

<http://hdl.handle.net/2066/75369>

Please be advised that this information was generated on 2017-12-06 and may be subject to change.

Muon Identification in the ATLAS Calorimeters

Muon Identification in the ATLAS Calorimeters

EEN WETENSCHAPPELIJKE PROEVE OP HET GEBIED VAN
NATUURWETENSCHAPPEN, WISKUNDE EN INFORMATICA

PROEFSCHRIFT

TER VERKRIJGING VAN DE GRAAD VAN DOCTOR
AAN DE RADBOUD UNIVERSITEIT NIJMEGEN
OP GEZAG VAN DE RECTOR MAGNIFICUS
PROF. MR. S.C.J.J. KORTMANN
VOLGENS BESLUIT VAN HET COLLEGE VAN DECANEN
IN HET OPENBAAR TE VERDEDIGEN OP VRIJDAG 12 JUNI 2009
OM 13:00 UUR PRECIES

DOOR

Gustavo Ordóñez Sanz

GEBOREN OP 02 JULI 1978
te Madrid, Spanje

promotor: Prof. dr. N. de Groot
copromotor: Dr. P. Kluit (Nikhef)

manuscriptcommissie:

Prof. dr. P. Groot
Prof. dr. ing. B. van Eijk (Nikhef/Universiteit Twente)
Prof. dr. T. Peitzmann (Universiteit Utrecht)
Dr. C. Timmermans (Nikhef)
Dr. K. A. Assamagan (BNL)

The work described in this thesis is part of the research programme of the 'Nationaal Instituut voor Subatomaire Fysica (Nikhef)'.

A mis abuelos, padres y hermana.

“La verdadera ciencia enseña, por encima de todo, a dudar y a ser ignorante.”

Miguel de Unamuno

CONTENTS

Introduction	1
1 Theoretical background	3
1.1 The Standard Model	3
1.1.1 Quantum electrodynamics	4
1.1.2 Quantum Chromodynamics	5
1.1.3 Electroweak interactions	6
1.1.4 Spontaneous symmetry breaking and the Higgs mechanism	7
1.1.5 Standard Model Lagrangian	8
1.1.6 Theoretical limits to the Higgs mass	9
1.1.7 Experimental limits to the Higgs mass	11
1.2 Higgs production and searches in ATLAS	12
2 ATLAS and LHC	17
2.1 The Large Hadron Collider	18
2.2 The ATLAS experiment	19
2.2.1 The inner detector	19
2.2.2 The calorimeters	24
2.2.3 Muon spectrometer	28
2.2.4 The forward detectors	29
2.2.5 The magnet system	30
2.2.6 The trigger system	31
3 Muon reconstruction	33
3.1 The ATHENA control framework	33
3.2 Track reconstruction in the inner detector	34
3.3 Track extrapolation	37
3.3.1 Material effects	38
3.3.2 Tracking Geometry	40
3.4 Muon identification	44
3.4.1 Monte Carlo samples	44
3.4.2 Standalone muons	44
3.4.3 Combined muons	51
3.4.4 Muon Taggers	55

4 Muon identification in the calorimeters	59
4.1 Data flow	60
4.2 Monte Carlo samples	61
4.3 Muon tagging	61
4.3.1 Track candidate preselection	62
4.3.2 Measured energy associated to the tracks	66
4.3.3 Track tagging	71
4.4 Performance of CaLoMuonTag	73
4.5 Improvements to the muon reconstruction	76
4.6 Conclusions	78
5 The $H \rightarrow ZZ^{(*)} \rightarrow 4\ell$ analysis	79
5.1 Monte Carlo samples and trigger studies	79
5.1.1 Signal Monte Carlo samples	79
5.1.2 Background Monte Carlo samples	80
5.1.3 Trigger	82
5.2 Electron and muon reconstruction	83
5.2.1 Electron reconstruction performance	84
5.2.2 Adding calorimeter identified muons to the analysis	84
5.3 Reducible background rejection	89
5.3.1 Lepton isolation	89
5.3.2 Impact Parameter	89
5.3.3 Selection Cuts	91
5.4 Event Selection and mass reconstruction	91
5.4.1 Lepton pairing, isolation and vertexing	92
5.4.2 Higgs mass reconstruction	93
5.4.3 Event selection results	93
5.5 Systematics Uncertainties	99
6 Conclusions	101
References	102
Summary	108
Samenvatting	111
Acknowledgements	113
Curriculum Vitae	114

INTRODUCTION

The idea of matter being composed of small elementary particles was already suggested by philosophers such as Leucippus, Democritus or Epicurus in ancient Greece. In the 19th century, John Dalton concluded that all kinds of matter were made up of a single kind of elementary particle. These particles came to be known as atoms. This name derived from the Greek word *atomos* meaning “indivisible”. However, before the turning of the century, scientists had already realised that atoms could be divided into smaller constituents. During the early years of the 20th century, nuclear physics experiments culminated in the discovery of nuclear fission and fusion, which made real (although not profitable) the old alchemist dream of transmuting lead into gold. During the years 1950s and 60s the world of physics was overwhelmed with the discovery of a large number of “elementary particles” which would be known as the *particle zoo*. In the mid 1970s, with the formulation of the Standard Model, the existence of all these particles could be explained in terms of few number of fundamental constituents.

The Standard Model is a relativistic quantum field theory consistent with both quantum mechanics and special relativity. It describes the strong, weak, and electromagnetic fundamental forces which are carried by mediating gauge bosons. These interaction bosons are known as gluons for the strong nuclear force, as W^\pm and Z for the weak nuclear force, and as photons (γ) for the electromagnetic force. In addition, the theory introduces 24 fundamental particles as the constituents of matter. The Standard Model also predicts the existence of another particle, known as the Higgs boson, which gives mass to the other particles. For a basic introduction see [1].

To date, almost all predictions of the Standard Model have been tested experimentally. As an example, the theory predicted the existence of the W^\pm , Z bosons, the gluon and the top or charm quarks well before their existence was confirmed in high energy physics experiments. However, there are still a number of theoretical and experimental limitations to the theory. The most evident being that it only explains three of the four known fundamental forces in nature, leaving out the gravitational interaction. Also recent evidence of oscillations in the neutrino sector, predict that actually neutrinos are not massless, as is commonly assumed in the Standard Model. Other paradoxes like the *hierarchy problem* or the evidence of *dark matter* and *dark energy* are not addressed by the theory. Today the common belief is that the Standard Model is an effective theory valid only up to a certain energy scale, after which, a more general theory would take over. These extensions to the Standard Model are enclosed in what is commonly known as Beyond the Standard Model Physics. Such theories include Supersymmetry, Extra Dimensions or String Theory.

The Higgs boson is the most important piece of the theory that has not been confirmed experimentally. It plays a very important role in the Standard Model since it provides a mechanism whereby particles acquire their mass. The Higgs mechanism can be pictured as a field covering the entire universe. This field would present “resistance” to the passage of

particles, and it would be this “friction” what is perceived as the mass of the particle. The Standard Model, however, does not predict the mass of the Higgs boson, which remains a free parameter of the theory.

The Higgs boson as predicted by the Standard Model is a highly unstable particle. Once enough energy is available to produce the Higgs particle, this will promptly decay through one of the possible decay channels. Some of these channels present special topologies that can be measured in high energy physics experiments. The first attempts to discover the Higgs boson were made at the LEP experiments at CERN, and although they were not successful, they provided many precision measurements that established limits to the Higgs mass. Namely, the LEP experiments excluded the existence of a Higgs mass below $114 \text{ GeV}/c^2$ and put an indirect upper limit to $144 \text{ GeV}/c^2$ both values obtained at a 95% confidence level. Currently, in the Tevatron accelerator at Fermilab, a proton anti-proton collider, the experiments CDF and DØ continue the pursuit of the discovery of the Higgs.

The next generation collider, the LHC, will provide proton-proton collisions with unprecedented luminosity and centre of mass energy. Its two general purpose experiments, CMS and ATLAS, will continue the search for the Higgs. In ATLAS, the channel where the Higgs boson decays into a pair of Z bosons, which further decay into either electrons or muons, presents the cleanest signature for a wide range of possible Higgs masses. The analysis of this channel relies on good lepton reconstruction and identification. This thesis presents an algorithm that attempts to identify muons in the ATLAS calorimeters using their distinctive energy deposition patterns. This algorithm, which is part of the ATLAS offline reconstruction chain, complements the standard muon reconstruction in the muon spectrometer, especially in the regions where the latter presents design limitations.

This thesis is divided into six chapters. Chapter 1 introduces the Standard Model formalism and the concepts of the Higgs boson production mechanisms. Chapter 2 gives a general overview of the LHC particle accelerator and the different ATLAS subdetectors. Chapter 3 presents the concepts of track reconstruction in both the inner detector and the muon spectrometer. It summarises the performance of the different tracking systems and the muon reconstruction algorithms. Chapter 4 introduces a calorimeter muon tagger algorithm that identifies the muon amongst all the inner detector tracks using the energy deposition measurements in the calorimeters. This chapter also presents a comparison study with other lepton reconstruction and identification algorithms. Chapter 5 presents an analysis on the $H \rightarrow ZZ^{(*)} \rightarrow 4\ell$ decay channel where the improvements associated with the use of the calorimeter muon tagger are evaluated. A discussion of the results obtained is given in Chapter 6.

CHAPTER 1

THEORETICAL BACKGROUND

1.1 The Standard Model

The Standard Model [2] is a theory that describes three of the four known fundamental interactions: the electromagnetic, the weak and the strong; leaving out the gravitational interaction. Mathematically, the Standard Model can be regarded as a relativistic quantum field theory [3]. It combines the electroweak and Quantum Chromodynamics theories into a gauge symmetry group $SU(3)_C \times SU(2)_I \times U(1)_Y$. The sub-indices – C , I and Y – stand for the conserved quantities – colour, isospin and hypercharge – respectively. In physics there is a deep connection between symmetries and conserved quantities. The Noether's theorem states that for every symmetry in a system, there is a related conserved physical quantity.

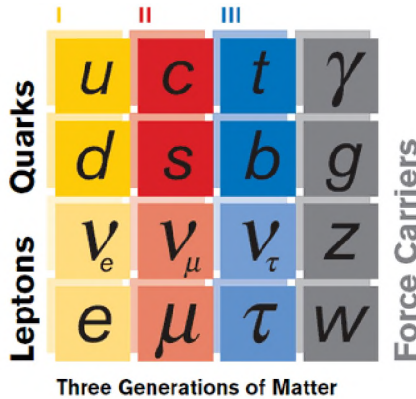


Figure 1.1: The three generation of leptons and quarks and the interaction carriers described in the Standard Model of particle physics.

The theory describes all the known particles, which are divided into leptons, quarks and interaction gauge bosons. Additionally, the particles are grouped into three different mass generations as shown in Figure 1.1. The only physical difference between the leptons: electrons, muons and taus (e , μ , τ); is their respective masses. In addition, each of them have associated massless leptons known as neutrinos. The six quarks are grouped into up-like (u, c, t) and down-like (d, s, b) types, with electrical charges $2/3$ and $-1/3$ respectively. The gauge bosons W^\pm and Z are responsible for the weak interactions, the photon (γ) is re-

sponsible for the electromagnetic, and eight different gluons which carry the strong nuclear interactions.

1.1.1 Quantum electrodynamics

The Quantum Electrodynamics [4] (QED) abelian gauge theory describes the interactions between charged particles and the electromagnetic force carrier, the photon. In the classical electrodynamic theory, the electric (\mathbf{E}) and magnetic fields (\mathbf{B}), in vacuum and in the presence of field sources with charge density ρ and current density \mathbf{J} are described by the Maxwell equations:

$$\begin{aligned}\nabla \cdot \mathbf{B} &= 0; & \nabla \times \mathbf{E} &= -\frac{\partial \mathbf{B}}{\partial t} \\ \nabla \cdot \mathbf{E} &= \frac{\rho}{\epsilon_0}; & \nabla \times \mathbf{B} &= \mu_0 \mathbf{J} + \frac{\partial \mathbf{E}}{\partial t}.\end{aligned}$$

The fields can be expressed in terms of potentials, the electric potential ϕ and the vector potential \mathbf{A} ,

$$\mathbf{E} = -\nabla\phi - \frac{\partial \mathbf{A}}{\partial t}; \quad \mathbf{B} = \nabla \times \mathbf{A}.$$

Also, the Maxwell equations are invariant under gauge transformation on the potentials,

$$A_\mu \rightarrow A'_\mu = A_\mu + \nabla_\mu f(\mathbf{r}, t)$$

here the potentials are grouped into the form of a four-vector $A^\mu(\phi, \mathbf{A})$, to simplify the notation. The term $f(\mathbf{r}, t)$ stands for any arbitrary scalar function. To emphasise the relativistic invariance of the Maxwell equations, it is convenient to introduce the electromagnetic tensor:

$$F_{\mu\nu} = \partial_\mu A_\nu - \partial_\nu A_\mu.$$

Defining the Lagrangian density of a electromagnetic system with source $J^\mu = (\frac{\rho}{\epsilon_0}, \mu_0 \mathbf{J})$ as

$$\mathcal{L} = -\frac{1}{4} F_{\mu\nu} F^{\mu\nu} - \frac{1}{c} J^\mu A_\mu,$$

solving the Euler-Lagrange equations yields,

$$\partial_\mu F^{\mu\nu} = \frac{4\pi}{c} J^\nu,$$

which are again the Maxwell equations in tensor notation.

In quantum mechanics, the potentials A^μ are used to construct the Hamiltonian of a wave function describing a particle of mass m moving through an electromagnetic field at a constant speed:

$$H\psi = i\frac{\partial\psi}{\partial t} = \left[\frac{-1}{2m} (\partial_\mu - i\frac{q}{\hbar c} A_\mu)^2 \right] \psi.$$

In order to keep the equation of motion invariant under local gauge transformations on the fields, the wave function needs to be transformed too. Defining a U(1) gauge transformation on the electric charge as:

$$\psi(\mathbf{r}, t) \rightarrow \psi'(\mathbf{r}, t) = e^{-i\frac{q}{\hbar c} f(\mathbf{r}, t)} \psi(\mathbf{r}, t)$$

and choosing the Lorentz gauge,

$$\partial_\mu A^\mu = 0$$

for the case without field sources, the Maxwell equations reduce to

$$\partial^\mu \partial_\mu A^\mu = 0,$$

which are precisely the Klein-Gordon equations for a massless particle: the photon.

In QED, the charged particles of spin 1/2 interacting with the electromagnetic field carried by spin-1 massless photons, are described by the Dirac equation:

$$i\gamma^\mu \partial_\mu \psi - m\psi = \frac{q}{\hbar c} \gamma^\mu A_\mu \psi$$

Finally, QED combines both results in the Lagrangian,

$$\mathcal{L}_{QED} = \bar{\psi}(i\gamma^\mu D_\mu - m)\psi - \frac{1}{4}F_{\mu\nu}F^{\mu\nu} - \frac{1}{c}J^\mu A_\mu$$

where

- γ^μ are the Dirac matrices.
- ψ are the Dirac spinors.
- $D_\mu = \partial_\mu + i\frac{q}{\hbar c}A_\mu$ is the gauge covariant derivative.

Therefore, QED is a quantum field theory which conserves the electrical charge through the invariance of the $U(1)_Q$ gauge symmetry. Which is an example of the application of Noether's theorem introduced earlier.

1.1.2 Quantum Chromodynamics

It is possible to construct an equivalent of the QED theory for quarks interacting through the strong force. This theory is known as Quantum Chromodynamics [5] (QCD). There are, however, significant differences between the electromagnetic and strong interactions. In QED it is enough to think of two charges of opposite sign; however in QCD, it is necessary to introduce three different charges or “colours” to describe the possible interactions. Also, while in QED the photon is the only responsible for the interaction, in QCD it is necessary to introduce eight different force carriers known as gluons. The gluons are spin-1 massless particles that carry two different colours. All this complicates the QCD Lagrangian considerably,

$$\mathcal{L}_{QCD} = \bar{\psi}_i(i\gamma^\mu (D_\mu)_{ij} - m\delta_{ij})\psi_j - \frac{1}{4}G_{\mu\nu}^a G_a^{\mu\nu}$$

where ψ_j are the Dirac spinors of the quarks, and $G_{\mu\nu}^a$ are the equivalents of the $F_{\mu\nu}$ electromagnetic tensor and represent the eight gluon field tensors. In QED the A_ν operator is commutative, however in QCD this no longer holds,

$$G_{\mu\nu} = \partial_\mu A_\nu - \partial_\nu A_\mu - ig[A_\mu, A_\nu] = \partial_\mu A_\nu - \partial_\nu A_\mu - ig_s \sum_{k=1}^8 f_{ijk} A_\mu^k A_\nu^j$$

or in other words, QCD is a non-abelian gauge theory that can be represented by the $SU(3)$ Lie group, f_{ijk} being the structure functions of the group. In physical terms, this non-commutative property allows the self coupling of gluons in three and four vertices.

It is possible to introduce, in analogy with QED, local gauge invariance in the QCD case, with gauge transformations of the type:

$$\psi(\mathbf{r}, t) \rightarrow \psi'(\mathbf{r}, t) = e^{-ig_s \sum_{i=1}^8 A_i \omega_i(\mathbf{r}, t)} \psi(\mathbf{r}, t)$$

where g_s is the strong coupling constant and ω_i are the wave functions describing the eight different gluons.

1.1.3 Electroweak interactions

The weak interaction [6] allows processes with fermion flavour exchanges. This symmetry can be represented by a $SU(2)$ Lie algebra defining local gauge transformations. The gauge transformations for the $SU(2)$ symmetry group can be written as:

$$\psi(\mathbf{r}, t) \rightarrow \psi'(\mathbf{r}, t) = e^{-ig \sum_{i=1}^3 I_i f_i(\mathbf{r}, t)} \psi(\mathbf{r}, t),$$

$$F_{\mu\nu}^i = \partial_\mu I_\nu^i - \partial_\nu I_\mu^i - ig \sum_{k=1}^3 \varepsilon_{ijk} I_\mu^k I_\nu^j.$$

Where I^i are the weak isospin operators, for which one possible representation are the Pauli matrices. ε_{ijk} is the usual Levy-Civita anti-symmetric tensor.

The corresponding potentials transform as:

$$W_i^\mu \rightarrow W_i'^\mu = W_i^\mu - \nabla f_i + g \sum_{jk} \varepsilon_{ijk} f_j W_k^\mu.$$

With the weak interaction it is possible to explain charge current interactions of the kind $e^- \rightarrow \nu W^-$. The charged currents defined by couplings to the W^\pm bosons involve either left handed fermions or right handed anti-fermions. The left handed and right handed parts of the Dirac spinors are obtained by applying the chirality operators:

$$P_L = \frac{1 - \gamma^5}{2} \quad P_R = \frac{1 + \gamma^5}{2}$$

to the fermion wave functions.

The neutral current terms involving the fourth component of the boson fields (W_3), could explain interactions of the type $e^- \rightarrow e^- W^0$. However, this would imply that both charge and neutral currents are of the same form and intensity, which is not verified experimentally. A beautiful solution is found by unifying the weak and the electromagnetic interactions using a $SU(2) \times U(1)$ gauge theory. For this, it is necessary to introduce the concept of hypercharge Y^W defined in terms of the charge Q as

$$Q = I_3^W + Y^W.$$

Requiring $U(1)$ gauge invariance on this hypercharge, it is possible to introduce scalar and vectorial potentials:

$$\phi^B \rightarrow \phi'^B = \phi^B + \frac{\partial f}{\partial t}; \quad \mathbf{B} \rightarrow \mathbf{B}' = \mathbf{B} - \nabla f.$$

Associating the electromagnetic potentials (ϕ, \mathbf{A}) with an appropriate linear combination of the (ϕ_3, \mathbf{W}_3) and (ϕ^B, \mathbf{B}) fields yields:

$$A^\mu = B^\mu \cos \theta_W + W_3^\mu \sin \theta_W$$

$$Z^\mu = B^\mu \sin \theta_W - W_3^\mu \cos \theta_W.$$

The second combination can be identified as the neutral current observed experimentally. There is one more problem that needs to be addressed before the complete Standard Model Lagrangian can be written. In this derivation, as in the photon and gluon case before, the Z and W^\pm bosons are massless. Experimentally however, it is confirmed that the weak force carriers are massive bosons, which also explains the short interaction range of the weak

force. In order to introduce mass terms for the weak bosons, the concept of spontaneous symmetry breaking mechanism can be used. In this mechanism, the W and B bosons are massless at high energies. At low energies, they interact with the ground expectation value of a new scalar field, the Higgs field. In this interaction the electroweak symmetry is spontaneously broken and the W and B bosons are re-combined into the massive W^\pm and Z massive bosons observed experimentally. This is called the Higgs mechanism which can also be used to give masses to the fermions by adding Yukawa terms to the SM Lagrangian.

1.1.4 Spontaneous symmetry breaking and the Higgs mechanism

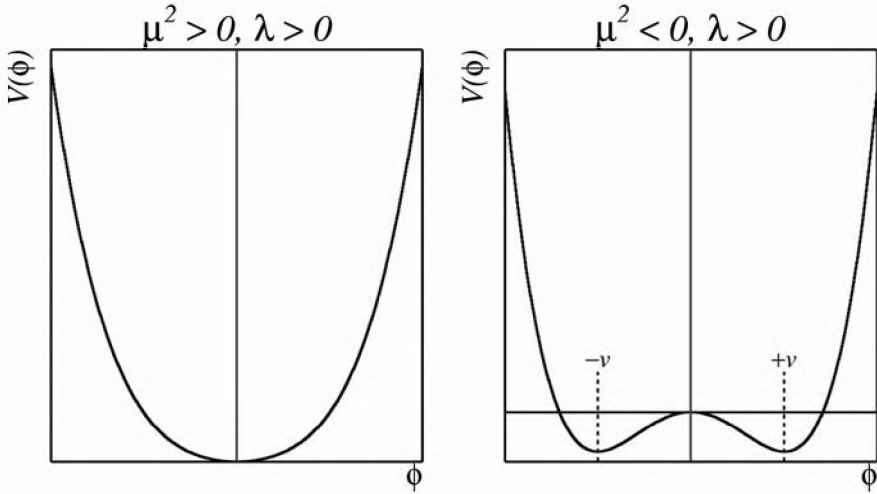


Figure 1.2: Potential function $V(\phi) = \mu^2\phi + \lambda\phi^2$ for different values of μ^2 and λ .

Introducing mass terms of the kind $M^2 W_\mu W^\mu$ would spoil the gauge invariance of the electroweak Lagrangian. However, by adding an additional term of the type

$$\mathcal{L}_H = (\partial^\mu \Phi)^\dagger (\partial_\mu \Phi) - V(\Phi^\dagger \Phi)$$

where Φ is a complex scalar field:

$$\Phi = \begin{pmatrix} \phi^+ \\ \phi^0 \end{pmatrix} = \frac{1}{\sqrt{2}} \begin{pmatrix} \phi_1 + i\phi_2 \\ \phi_3 + i\phi_4 \end{pmatrix},$$

the potential term can be defined as:

$$V(\Phi) = \mu^2 \Phi^\dagger \Phi + \lambda (\Phi^\dagger \Phi)^2$$

where λ is the coupling constant of the interaction which depends on the energy scale considered. λ needs to be positive to avoid negative values of the potential $V(\Phi)$ for large values of Φ . As the Figure 1.2 shows, if the μ^2 constant is chosen to be $\mu^2 < 0$, a non trivial minimum of the potential exists. Where

$$v = \sqrt{\frac{-\mu^2}{\lambda}}$$

is the expectation value of the Higgs field in vacuum: $\langle 0|\Phi|0 \rangle$. When perturbative theory around this minimum is performed, the gauge symmetry is broken, allowing mass terms to emerge. This concept is known as the Higgs mechanism [7][8]. To guarantee that the photon stays massless when the symmetry is broken, ϕ^+ is set to 0. The simplest way to break the gauge symmetry is by choosing $\phi_3 = v$ and $\phi_2 = \phi_4 = 0$. Making this choice and expanding the scalar potential Φ around the ground state gives:

$$\phi(\mathbf{r}) = \frac{1}{\sqrt{2}} \begin{pmatrix} 0 \\ v + H(\mathbf{r}) \end{pmatrix},$$

where $H(\mathbf{r})$ is the Higgs boson field. Considering the $SU(2)$ gauge invariant Lagrangian;

$$\mathcal{L} = (D^\mu \phi)^\dagger (D_\mu \phi) - V(\phi) - \frac{1}{4} W_{\mu\nu}^i W_i^{\mu\nu} - \frac{1}{4} B_{\mu\nu} B^{\mu\nu},$$

with the chosen values for $V(\phi)$ plus a gauge boson term. Expanding around the vacuum state and using the linear combinations for the W and B bosons introduced in the last section, the following Lagrangian is obtained:

$$\begin{aligned} L = & (D^\mu H)^\dagger (D_\mu H) - \mu^2 H^2 - \lambda v H^3 - \frac{1}{4} \lambda H^4 \\ & + (D^\mu \phi)^\dagger (D_\mu \phi) - \frac{1}{4} A_{\mu\nu} A^{\mu\nu} \\ & - \frac{1}{4} W_{\mu\nu}^+ W_-^{\mu\nu} - \frac{1}{4} Z_{\mu\nu} Z^{\mu\nu} \\ & + \frac{1}{2} m_W^2 W_\mu^+ W_-^\mu + \frac{1}{2} m_Z^2 Z_\mu Z^\mu. \end{aligned}$$

The second term is the Higgs mass with $M_H = \sqrt{2\lambda}v$. The third and fourth terms represent the 3-bosons and 4-bosons Higgs self-interactions. The new Lagrangian has mass terms for the W Z linear combinations while the photon potential A_μ stays massless conserving the $U(1)$ gauge invariance. Notice that while the Lagrangian conserves the gauge symmetry, expansions made at low enough energies around the ground state do not. In other words, bosons acquire mass in their interaction with the non-zero vacuum value of the Higgs field.

1.1.5 Standard Model Lagrangian

It is possible now to write the complete Lagrangian of the Standard Model. Before the electroweak symmetry breaking the Lagrangian reads:

$$\mathcal{L}_{SM} = \mathcal{L}_{YM} + \mathcal{L}_f + \mathcal{L}_Y + \mathcal{L}_H,$$

where

$$\mathcal{L}_{YM} = -\frac{1}{4} W_{\mu\nu}^i W_i^{\mu\nu} - \frac{1}{4} B_{\mu\nu} B^{\mu\nu} - \frac{1}{4} G_{\mu\nu}^a G_a^{\mu\nu}$$

is the Yang-Mills term which contains the interaction between gauge bosons. The index a runs from 1 to 8, whilst the index i runs from 1 to 3. The term

$$\mathcal{L}_f = i\bar{\psi}_L \gamma^\mu D_\mu \psi_L + i\bar{\psi}_R \gamma^\mu D_\mu \psi_R,$$

is the fermionic part of the Lagrangian where the L doublets and the R singlets of the $SU(2)$ electroweak gauge, are written separately. The covariant derivative D_μ is defined as:

$$D_\mu = \partial_\mu + i\frac{g_1}{2} Y B_\mu + ig_2 I_i W_\mu^i - ig_3 G_\mu^a \lambda_a.$$

The Yukawa part of the Lagrangian [9]

$$\mathcal{L}_Y = -ig_f \bar{\psi}_L \Phi \psi_R - ig_f \bar{\psi}_R \Phi \psi_L$$

allows the fermions to acquire mass interacting with the field Φ . The \mathcal{L}_H is the Higgs Lagrangian introduced in the previous section. Once the electroweak symmetry is spontaneously broken, the interaction bosons acquire mass. This mass can be expressed in terms of the coupling constants and the Higgs zero expectation value v :

$$M_W^\pm = \frac{v}{2} g_2 \quad M_Z = \frac{v}{2} g_2 \sqrt{g_1^2 + g_2^2}.$$

In terms of the fermion coupling constants and v , the fermion masses become:

$$m_f = \frac{v}{\sqrt{2}} g_f.$$

Therefore, using the experimental results for the measurement of the W and Z masses and the coupling constants, the value of v as well the electroweak mixing angle ($\cos \theta_W = M_W/M_Z$) can be determined. Their current experimental values are $M_W^{exp} = 80.392 \pm 0.039$ and $M_Z^{exp} = 91.1876 \pm 0.0021$. These are in very good agreement with the SM predictions: $M_W^{SM} = 80.376 \pm 0.017$ and $M_Z^{SM} = 91.1874 \pm 0.0021$. The Higgs boson vacuum expectation value is then $v \approx 246$ GeV.

1.1.6 Theoretical limits to the Higgs mass

The Higgs mechanism allows all the particles of the SM to acquire mass. However, the exact value of the Higgs boson mass is not determined by the theory. As shown in the previous section the Higgs boson mass [10] is

$$M_H = v\sqrt{2\lambda}$$

where v can be calculated using electroweak precision measurements. However, the value of λ remains unknown. In gauge theories such as the Standard Model, perturbation theory is used as an approximation to perform calculations of quantities like particle masses, coupling constants or cross sections. When applying perturbation theory in orders above *tree level*, which means solving Feynman diagrams containing loops, the integrals involved are often divergent. These divergences spoil the predictability of the SM. A technique known as *renormalisation* can be used to “swap” these divergences into bare particle masses and coupling constants. The SM then becomes an effective theory depending on a cut-off energy scale. When the physical constants are renormalised, they become functions of the energy scale considered. After renormalisation λ becomes:

$$\lambda(\Lambda^2) = \frac{\lambda(v^2)}{1 - \beta \ln\left(\frac{\Lambda^2}{v^2}\right)}$$

where Λ is the renormalisation scale at which the predictions are calculated, and β is the renormalisation group equation, which at next-to-leading (NLO) calculation becomes:

$$\beta = \frac{12\lambda(v^2)}{16\phi^2}.$$

Choosing the Λ scale at the Landau pole Λ_L where the renormalisation scale is no longer valid the function λ blows up:

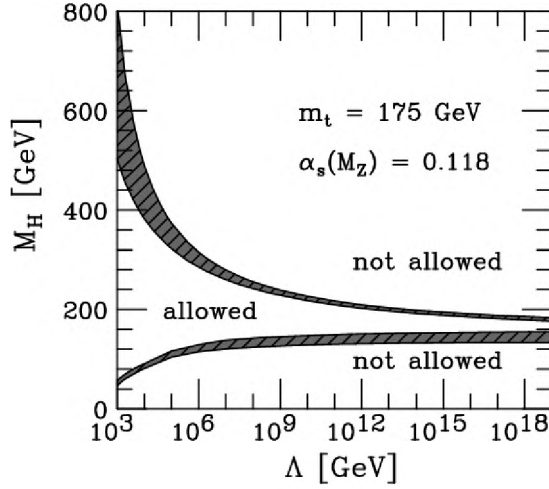


Figure 1.3: Theoretical limits on the Higgs boson mass M_H as a function of the Landau pole Λ_L [10].

$$\ln\left(\frac{\Lambda_L^2}{v^2}\right) = 1/\beta = \frac{16\phi^2}{12\lambda(v^2)}$$

or

$$\lambda(v^2) = \frac{16\pi^2}{12\ln\left(\frac{\Lambda_L^2}{v^2}\right)},$$

Choosing an energy scale below the Landau pole makes it possible to set an upper bound for the Higgs mass:

$$M_H^2 = 2\lambda(\Lambda)v^2 < 2\lambda(v^2)v^2$$

then

$$M_H^2 < 2v^2 \frac{16\pi^2}{12\ln\left(\frac{\Lambda_L^2}{v^2}\right)}.$$

A theoretical lower limit on the Higgs mass can be found by looking at small values of the running constant λ . It was already noticed that λ needs to be positive in order to prevent the Higgs potential from diverging. It can be seen that for small values of λ , the most dominant term in its dependence with the energy scale is through the Higgs boson coupling to the top quark,

$$\frac{\partial\lambda}{\partial(\ln\Lambda^2)} \propto -g_t^4.$$

Here

$$g_t = \sqrt{2}\frac{m_t}{v}$$

is the top Yukawa coupling and m_t the top quark mass. To first order calculations this means that

$$\lambda(\Lambda_L^2) = \lambda(v) - \frac{12}{16\pi^2}g_t^4 \ln\left(\frac{\Lambda_L^2}{v^2}\right) > 0,$$

thus

$$M_H^2 > \frac{12}{16\pi^2}v^2g_t^4 \ln\left(\frac{\Lambda_L^2}{v^2}\right).$$

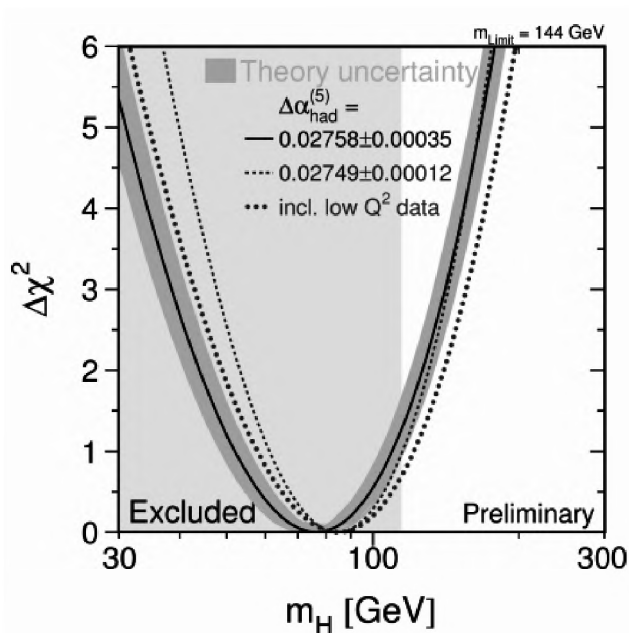


Figure 1.4: $\Delta\chi^2$ fit of the electroweak parameters measured experimentally as a function of possible Higgs masses [11].

Figure 1.3 shows the theoretical upper and lower limits on the Higgs mass as a function of the breakdown scale Λ_L . Hence, these theoretical arguments exclude Higgs masses above 1 TeV.

1.1.7 Experimental limits to the Higgs mass

The experimental lower limits set to the Higgs boson mass [12] come mainly from direct searches performed at LEP [11]. The LEP experiment was an electron-positron collider which achieved centre of mass energies above 200 GeV. At that energy the primary source of the Higgs production is $e^+e^- \rightarrow ZH$. The actual analysis performed at LEP, searched for Higgs decays of the type $H \rightarrow b\bar{b}$, with the Z boson decaying in all possible channels; and $H \rightarrow \tau^+\tau^-$, with Z decaying hadronically. Using the combined data of all four LEP experiments a lower limit to the Higgs mass was found: $M_H > 114.4$ GeV at a 95% confident level (CL).

Since most of the electroweak parameters are sensitive to the Higgs mass via corrections involving loop diagrams, precision measurements of 18 of these parameters can be combined in a global χ^2 fit. Figure 1.4, shows the $\Delta\chi^2(M_H) = \chi^2(M_H) - \chi_{min}^2$ using data from LEP, SLC (Stanford Linear Collider) and Tevatron combined. This fit sets an upper limit on $M_H < 144$ GeV at a 95% CL. The largest sources of uncertainty in this fit are the errors in the measurements of the W and t-quark masses. Figure 1.5 shows such uncertainties in relation to the possible masses for the Higgs boson. Searches for light Higgs bosons continues at the Tevatron experiments, DØ and CDF, at Fermilab [13].

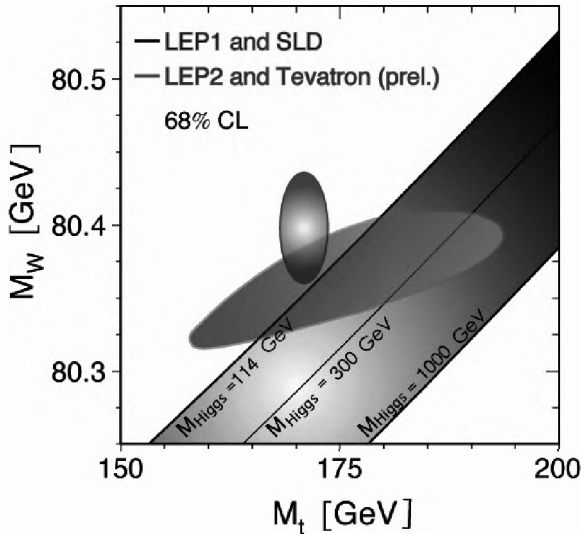


Figure 1.5: The figure shows the experimental results on the measurement of the mass of the W^\pm bosons as a function of the top quark mass m_t . Precision electroweak measurements can be used to set limits on the Higgs boson mass [11].

1.2 Higgs production and searches in ATLAS

The next generation of experiments that will join the search of the Higgs are CMS and ATLAS at the Large Hadron Collider (LHC) at CERN. In high energy physics experiments, the processes cross sections are measured in barns, where 1 barn (b) equals 10^{-24} cm^2 . At the design luminosity and centre of mass energy the LHC, the Higgs boson production cross section will be of the order of tens of pb , depending on the production mechanism as shown in Figure 1.6. The first on the top left corner, known as *gluon-gluon fusion* has the largest cross section, followed by the *vector boson fusion* (VBF), on the upper right corner in the figure. The other two processes are the $t\bar{t}$ fusion, bottom left; and the *Higgs-strahlung*, bottom right. Figure 1.7 shows the cross sections for these mechanisms as a function of the Higgs mass calculated at NLO.

Searches for the Higgs boson in the ATLAS experiment are performed in a number of different channels. A detail study of this channels can be found in the Higgs chapter of the Physics part in [14]. Since the Higgs coupling is proportional to the mass of the particle considered, the Higgs boson will decay with more probability to particles with bigger masses as shown in Figure 1.8. A detailed study on the Higgs cross sections and branching ratios in ATLAS is found at [15]. A brief introduction to these channels main backgrounds and the expected signal significance follows.

$H \rightarrow \gamma\gamma$

This is a relevant channel for Higgs masses below $150 \text{ GeV}/c^2$. Its main background is the $\gamma\gamma$ continuum. Other potential backgrounds are γ /jet and two-jet events (a jet is a group hadrons and other particles found in a narrow cone and produced by the hadronization of

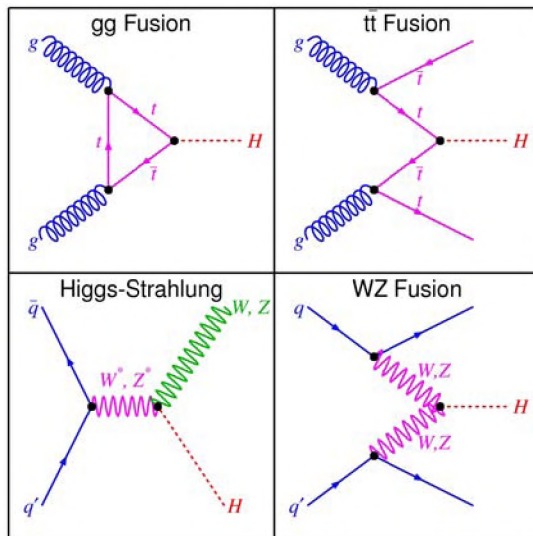


Figure 1.6: Feynman diagrams for the Higgs boson production channels.

a quark or gluon, or in τ decays). The jet backgrounds can be reduced using isolation cuts and pion rejection. The resolution of the electromagnetic calorimeter and the accuracy in determining the primary vertex are very important for this channel. At a luminosity of $2 \cdot 10^{33} \text{ cm}^{-2} \text{ s}^{-1}$, it will be possible to fit the primary vertices using tracks from the underlying event. For this a precision of $40 \mu\text{m}$ along the direction of the beam can be achieved. However, at the design luminosity of $10^{34} \text{ cm}^{-2} \text{ s}^{-1}$, with an average of 27 interaction vertices, a good photon identification in the calorimeters will be required. At high luminosity, a vertex reconstruction resolution of 1.6 cm will be possible using the EM calorimeter information. A significance of 4.6σ for an integrated luminosity of 30 fb^{-1} is expected for a Higgs mass of $120 \text{ GeV}/c^2$.

$H \rightarrow \tau\tau$

For the VBF production in combination with two jets, the main background for this channel would be Z +jets. A central jet veto in the case of the QCD contribution, and $\tau\tau$ mass reconstruction for the electroweak production can be used to reduce this background. It is possible to reconstruct the Higgs mass peak using the collinear approximation of the τ decays, which is dominated by the resolution in missing transverse energy (E_T^{miss}). With a Higgs boson mass of $130 \text{ GeV}/c^2$, a combined significance of 5.7σ can be expected for the $\tau\tau \rightarrow \ell\ell$ and $\tau\tau \rightarrow \ell h$ channels at an integrated luminosity of 30 fb^{-1} .

$H \rightarrow WW$

This channel has very good discovery potential for Higgs bosons with masses ranging from 125 up to $190 \text{ GeV}/c^2$. Possible analyses in the decay channels are $W \rightarrow \ell\nu jj$ and $WW \rightarrow \ell\nu\ell\nu$. The main background for these channels are the $t\bar{t}$ +jets, W +jets and WW +jets. Although it is not possible to reconstruct a mass peak in this channel, a transverse mass defined as $M_T = \sqrt{2p_T^{\ell} E_T^{\text{miss}} (1 - \cos(\Delta\phi))}$ can be used as a discriminant. The

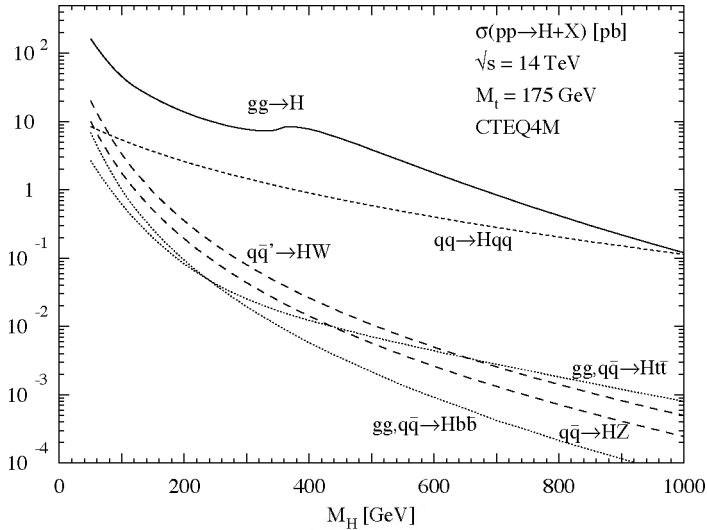


Figure 1.7: Higgs boson production cross sections at the LHC as a function of its mass [16].

signal significance is above 5σ for $30 fb^{-1}$ in the entire $125 - 190 GeV/c^2$ range.

$H \rightarrow b\bar{b}$

In the associated production of a Higgs boson in combination with a $t\bar{t}$ pair, the Higgs decaying to $b\bar{b}$ has discovery potential in the case of a light Higgs. The main reducible backgrounds are $t\bar{t}$ +jets, which can be reduced through b-tagging cuts, and $WWbbjj$ with a $W+6$ jets signature. The irreducible backgrounds $t\bar{t}b\bar{b}$ can be rejected using kinematic differences with the signal through multi-variable methods. The expected signal significance for this channel at an integrated luminosity of $30 fb^{-1}$ is 2.8σ for a Higgs mass of $120 GeV/c^2$

$H \rightarrow ZZ^{(*)} \rightarrow 4\ell$

Although its cross section is rather small, this channel offers a clean signature over the full range of Higgs masses above $120 GeV/c^2$. The main backgrounds for this channel are the irreducible $ZZ^{(*)}/\gamma \rightarrow 4\ell$, and the reducible $Zb\bar{b}$ and $t\bar{t}$. Lepton isolation and cuts on the impact parameter significance can be used to reduce these backgrounds. The reconstructed Higgs mass resolution in this channel is defined by the resolution of the momentum reconstruction for electrons and muons. A full study of this channel is presented in Chapter 5.

Figure 1.9 shows the ATLAS The median discovery significance for the various channels and the combination with an integrated luminosity of $10 fb^{-1}$.

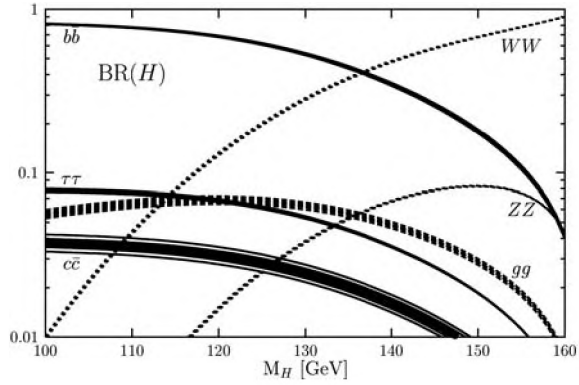


Figure 1.8: Branching ratios for the different Higgs boson decay channels as a function of its mass. Calculated using the HDECAY program [17]

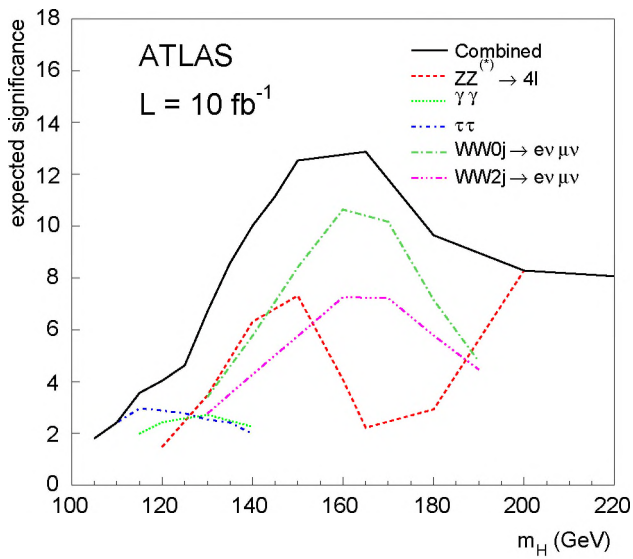


Figure 1.9: Higgs boson discovery potential, as a function of its mass, in the different decay channels independently and for their combination [14].

CHAPTER 2

ATLAS AND LHC

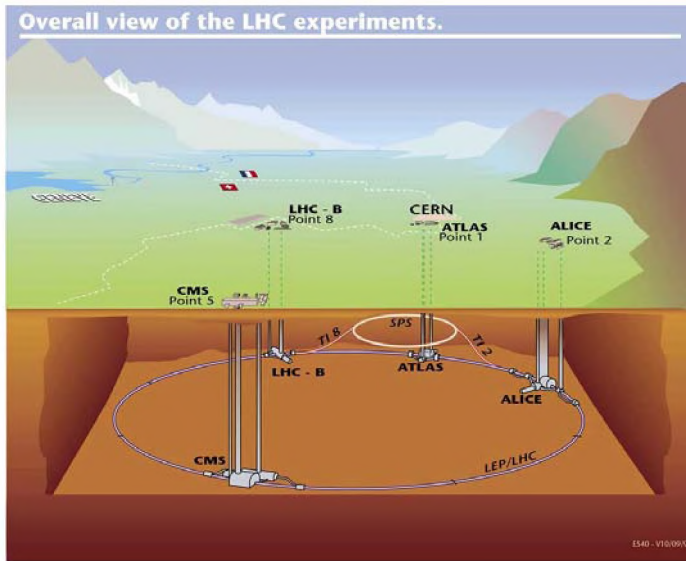


Figure 2.1: Overview of the situation of the LHC and different experiments.

The Large Hadron Collider (LHC) [18], the world's largest particle accelerator, is being assembled in the tunnel left by its predecessor, the LEP experiment at CERN. Bunches of up to 10^{11} protons (p) will collide every 25 ns (i.e 40 million times per second) at a centre of mass energy of 14 TeV. Alternatively, the LHC will also collide heavy ions with an energy of 5.5 TeV per nucleon pair.

Figure 2.1 shows an schematic situation of the LHC accelerator below the Swiss-French border near Geneva. Several experiments will profit from the LHC collisions. Two general purpose detectors ATLAS [19] (A Toroidal LHC ApparatuS) and CMS [20] (Compact Muon Solenoid). ALICE [21] designed to study strongly interactive matter such as quark-gluon plasma in heavy ion collisions. LHCb [22] a B-physics experiment aiming to study CP-violation. In addition other smaller experiments will also run at the LHC. TOTEM [23] will measure the p-p cross section and elastic scattering. LHCf [24] will study

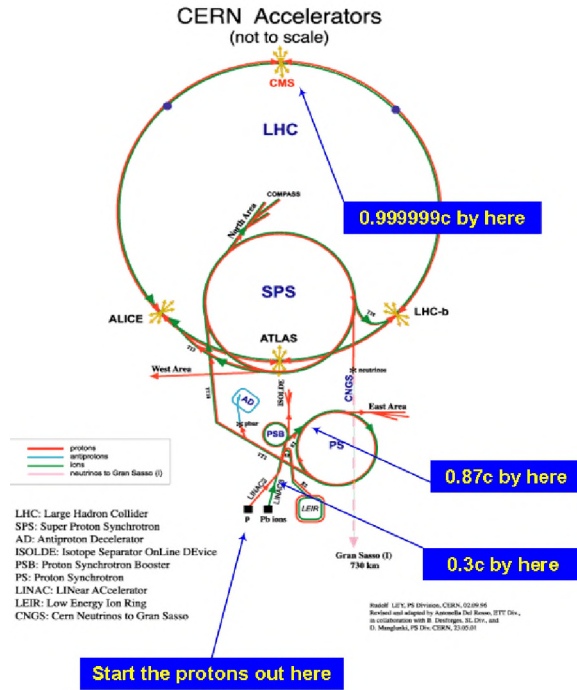


Figure 2.2: Overview of the LHC accelerator at CERN.

energy distributions in very forward physics, almost parallel to the injected beam.

2.1 The Large Hadron Collider

At the LHC two beams of protons will be accelerated in opposite directions. Each beam will achieve energies up to 7 TeV. Once the beams reach the desired energy they will be collimated and will be collided at four different points of the tunnel. ATLAS, CMS, ALICE and LHCb are located at these four points. Figure 2.2 shows the different stages needed in order to accelerate the beams up to the required energy. In the first stage, the protons are accelerated in a linear accelerator (LINAC) before being passed to the Proton Synchrotron (PS) for further boosting. The beams enter then the Super Proton Synchrotron (SPS) where the protons gain an energy of 450 GeV. Finally, the particles are injected into the LHC tunnel, which has a circumference of 26.7 km, where the beams are collided at a centre of mass energy of 14 TeV. The beams follow circular trajectories inside the tunnel thanks to the field generated by superconducting magnets. Each beam line consist of 1232 superconducting dipole bending magnets generating a magnetic field of 8.36 Tesla. To accelerate the protons in opposite directions, two separated vacuum beam lines are used. In one of the lines the protons move clockwise and in the other they move anti-clockwise.

The LHC will provide a total luminosity of $10^{34} \text{ cm}^{-2} \text{ s}^{-1}$ when running at the design luminosity. At this luminosity there will be an average number of 27 interaction per bunch crossing, therefore the total number of proton-proton interactions will be of about 10^9 per second. This high luminosity will allow studies of physics processes with very small cross sections.

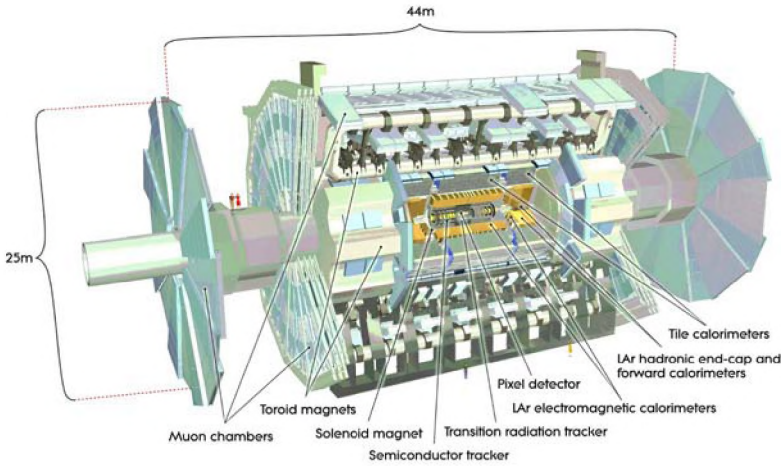


Figure 2.3: View of the ATLAS detector.

2.2 The ATLAS experiment

ATLAS is a general purpose detector designed to profit from the entire discovery potential of the LHC. Figure 2.3 shows a schematic view of the ATLAS detector and subdetectors. ATLAS is about 45 meters long, more than 25 meters high and has an overall weight of approximately 7000 tonnes. The inner detector represents the inner most part of ATLAS. It is built around the beam pipe and is designed especially for tracking and vertexing. It is formed by the Pixel, SCT (Semiconductor Tracker) and TRT (Transition Radiation Tracker) detectors. It measures the trajectories of charged particles created in the collisions. The inner detector is embedded in a solenoidal magnet which generates a magnetic field of 2 Tesla. The curvature of the trajectories which results from the the magnetic field bending power, is used to calculate the momentum of the particles. Additionally, the TRT provides electron identification measuring transition radiation photons generated in its radiator material.

The electromagnetic and hadronic calorimeters surround the solenoid magnet. The calorimeters are designed to measure the energy of the different kinds of particles. The last layer of the detector is formed by the muon spectrometer and the toroid magnets. The muon tracking system measures the trajectories of charged particles leaving the calorimeters. The trajectories are bent by the magnetic deflection provided by three superconducting air-core toroid magnets, which generate a field of 0.5 Tesla.

2.2.1 The inner detector

The coordinate system of the ATLAS detector is defined in cartesian coordinates with the z-axis running along the beam pipe, the x-axis pointing to the outside of the LHC ring, and the y-axis pointing up. The origin of the coordinate system is located at the centre of the detector. However, often spherical coordinates are used to describe the subdetector and physics processes. The azimuthal angle $\phi = [0, 2\pi]$ is the angle formed with the x-y plane.

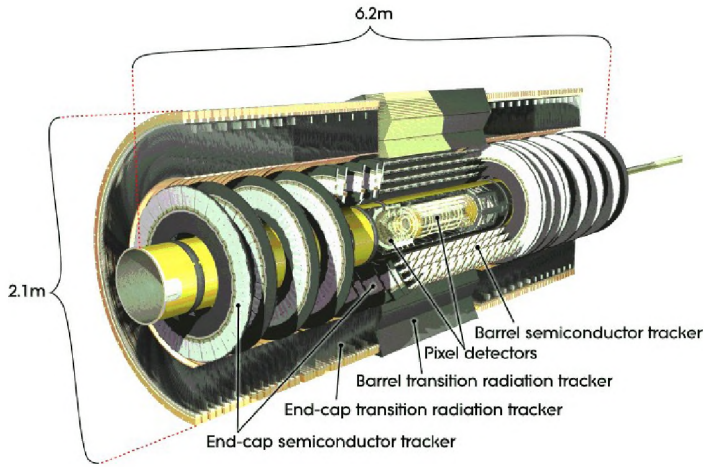


Figure 2.4: The ATLAS inner detector.

The polar angle $\theta = [0, \pi]$ is the angle formed with the z-axis. θ is often replaced by the pseudorapidity η defined as

$$\eta = -\ln(\tan(\theta/2)).$$

At design luminosity more than 1000 particles will pass through the inner detector [25] each bunch crossing. In order to achieve the high-precision measurements imposed by the physics processes it is necessary to have a very fine granularity. The charge, momentum, track direction and the impact parameter (shortest distance to the z-axis) are measured in the inner detector. It can also identify the origin of the particle (vertexing), and determine if the track originated from the interaction point or at some distance from this (secondary vertex), as is the case for B-mesons and converted photons. Figure 2.4 shows a layout of the inner detector.

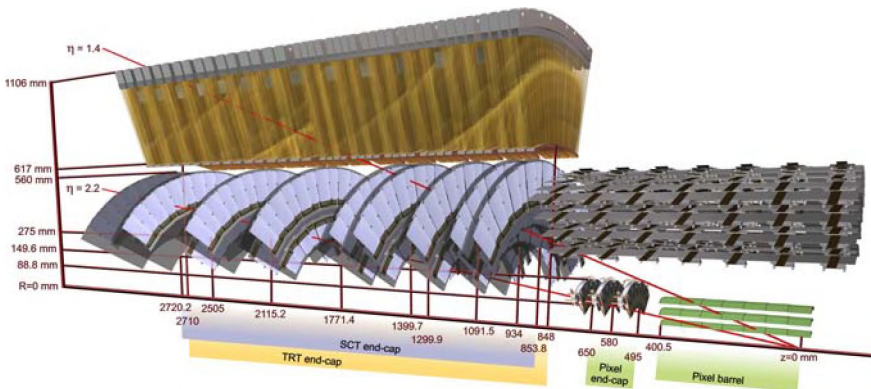


Figure 2.5: Two charged tracks of $p_T = 10 \text{ GeV}/c$ in the endcap inner detector with $\eta = 1.4$ and 2.2 respectively, transverseing different detector components.

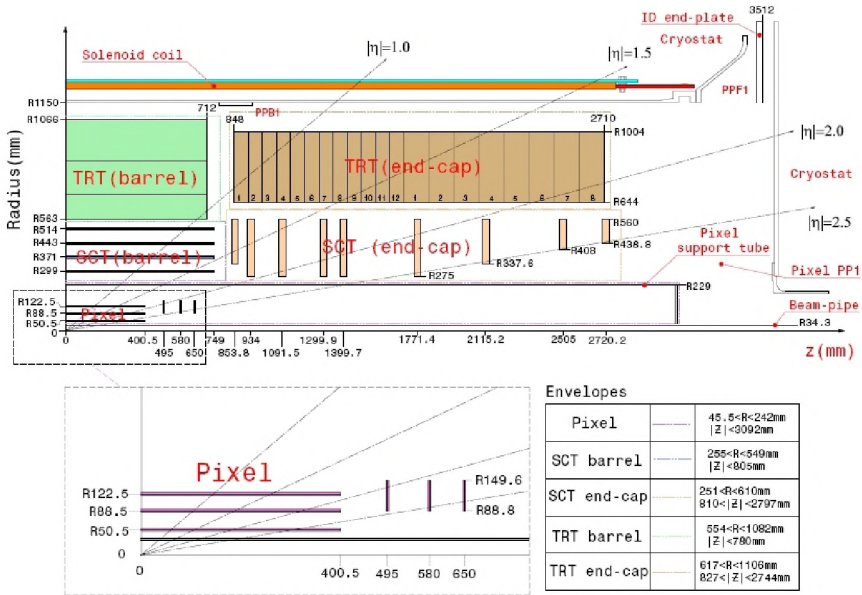


Figure 2.6: $R-z$ cut of the ATLAS inner detector with the different dimensions and η coverage of the different subdetectors.

The inner detector extends up to $|\eta| < 2.5$ and it presents very good performance for central tracks up to $|\eta| < 2.0$, where the coverage of the TRT ends. As an example, Figure 2.6 shows two charged tracks with $p_T = 10$ GeV/ c in the inner detector endcap with $\eta = 1.4$ and 2.2 respectively. The track with $\eta = 1.4$ traverses the three cylindrical pixel layers, four of the endcap discs, and approximately 40 straws of the endcap TRT wheels. The track at $\eta = 2.2$ only traverses the first of the cylindrical pixel layers, two endcap pixel discs and the last four endcap discs. Figure 2.7 shows a view of the different subdetectors in their nominal positions, stating their dimensions and η coverage.

The pixel detector

The pixel detector [26] is located closest to the beam pipe. It consists of three cylindrical barrel layers and three discs in each endcap. A charged particle traversing the detector produces electron/hole pairs in the semiconductor sensors [27]. The free charge is collected applying a bias voltage. If the collected charge is above 0.5 fC, which is equivalent to ~ 3000 electrons, the readout electronics writes out both the pixel address and the time over threshold (ToT). Later, the ToT is used to recover the amount of charge that was deposited in the sensor.

All of the 1744 pixel sensors are identical with a thickness of 250 μm . The minimum dimensions for each pixel are 50×400 μm^2 with a precision of 10 μm in the $R-\phi$ coordinate and of 115 μm in the transverse direction. The barrel layers are perpendicular to the R coordinate whilst the endcap discs are perpendicular to the beam axis. The pixel detector has approximately 80.4 million readout channels.

The sensors consist of oxygenated n-type wafers with readout pixels on the implanted n^+ side of the detector. This design was chosen since highly oxygenated material presents high radiation tolerance. Due to the intense radiation damage that the first vertexing layer (B-layer) of the pixel detector has to endure, it will be replaced after 3 years of operation at

design luminosity. In order to minimise the radiation damage and the consequent leakage current, both the pixel and SCT sensors are cooled down to an operation temperature range of 5 to 10°C.

The alignment tolerances for the B-layer are 10 μm in the radial coordinate R , 20 μm in the axial coordinate z and a tolerance of 7 μm in the $R\text{-}\phi$ coordinate. In the case of the other two cylindrical layers, the same tolerances are allowed with the exception that in the R coordinate the leverage is risen to 20 μm . In the pixel endcap discs, an alignment tolerance of 20, 100 and 7 μm in R , z and $R\text{-}\phi$ are allowed respectively.



Figure 2.7: Installation of the pixel detector in ATLAS on June 2007.

The SCT detector

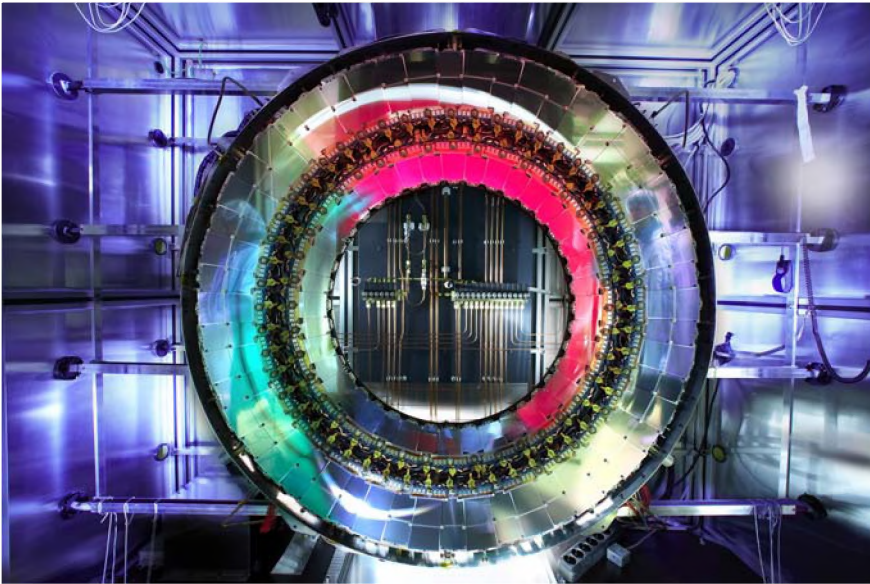


Figure 2.8: SCT endcap disc inside text-box at Nikhef.

The SCT detector surrounds the pixel detector. It consists of one cylindrical barrel and two endcaps. The SCT measurements are very important for the final tracking resolution, impact parameter calculation and the positioning of the z -coordinate of the vertex. The SCT has a total of 4088 modules, 2112 modules distributed in four coaxial layers in the barrel and 988 modules distributed among nine discs in each endcap. Each barrel module [28] consists of two pairs of sensors, which are bonded together on the top and bottom, with a stereo-angle of ± 20 $m\text{rad}$. The endcap modules [29] consist of only two sensors per module. The SCT silicon sensors are segmented in *strips*, therefore only one coordinate is measured accurately with a resolution of about 23 μm . In addition, each sensor is connected to binary signal readout chips, pro-

viding binary information. However, the small stereo-angle around the geometrical centre of the module, makes it possible to measure the second coordinate by finding the intersection of the strips in the top and bottom layers of the sensor. The resolution for the second coordinate is approximately $800\ \mu\text{m}$. In total there are 15912 SCT sensors and 786 strips per sensor, which gives more than 6 million read out channels.

The sensor will initially operate at a bias voltage of $150\ \text{V}$. However, due to the expected radiation damage during the 10 years of operation, this voltage will have to be risen gradually up to $400\ \text{V}$. The sensor thickness of $285 \pm 15\ \mu\text{m}$ was chosen as the best compromise between the required operating voltage, the signal ionisation and simplicity of fabrication. The chosen strip pitch was determined by the requirements in precision and the noise level tolerance of $5 \cdot 10^{-4}$ for a tracking efficiency above 99% [30].

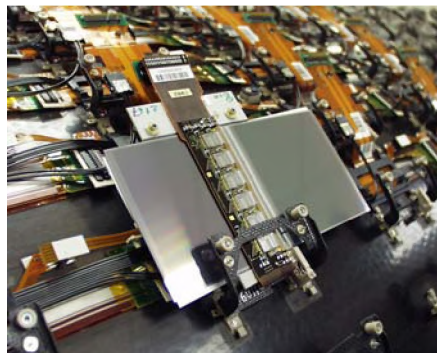


Figure 2.9: Closeup of SCT module mounted on the barrel.

Figure 2.9 shows a section of the SCT barrel with a mounted module. The barrel modules have a rectangular size with dimensions of $6 \times 12\ \text{cm}^2$. The strips run parallel to the long side of the sensor. The readout electronics are mounted on top of the module. In the endcap, the modules are mounted following a “fan” geometry, with the strips in each module pointing towards the centre of the disc. Depending on the type of module considered, the strip length is either 6 or 12 cm. Figure 2.8, shows one of the endcap discs being tested at Nikhef.

The TRT detector

The TRT [31] is the outermost layer of the inner detector. It is central to the track momentum estimation. Additionally, the transition radiation properties of the TRT material allow electron identification. The TRT modules are made of polyimide drift tubes called *straws*. Each straw has a diameter of $4\ \text{mm}$ and is positioned along the beam pipe in the barrel modules and radially in the endcaps. The straw tube wall is made of multi-layer films with a thickness of $35\ \mu\text{m}$ bonded together back-to-back. This design guarantees that the straws have good electrical and mechanical properties. The anodes are $31\ \mu\text{m}$ in diameter and made of tungsten wires plated with 0.5 to $0.7\ \mu\text{m}$ of gold. Their resistance is approximately $60\ \Omega/\text{m}$ and their capacitance is less than $10\ \text{pF}$. The signal attenuation length is about $4\ \text{m}$ and the propagation time is $4\ \text{ns}/\text{m}$. The anodes are supported at each end by a plug and the tubes are filled with a gas mixture of 70% Xe, 27% CO_2 and 3% O_2 with a pressure of 5 to 10 mbar. The cathode is operated at $-1530\ \text{V}$, with a gain of $2.5 \cdot 10^4$.

When a charged particle crosses the straw tube, the gas is ionised and the charge produced is collected in the anode. Measuring the time it takes to collect the charge, the distance of the track to the anode can be estimated. This distance is known as the *drift radius*, which can be measured with a resolution of $170\ \mu\text{m}$. The entire TRT contains 73 straw layers in the barrel with a total number of 52,544 straws. Each endcap consists of 18 wheels with 160 straw planes and with a total of 159,744 straws. Figure 2.10 shows a picture a barrel module.

Tracks with a transverse momentum above $0.5\ \text{GeV}/c$ typically pass through at least 36 straws, except in the barrel-endcap transition where a minimum of 22 straws are crossed.

Transition radiation photons are produced in the radiator material which fills up the space between the straws. The number of predicted photons is related to the amount of energy and mass of the interacting particle. The electrons produce significantly more photons than other kinds of particles. The mixture of gas filling the straws is sensitive to these transition photons, which can be used to identify tracks as electrons. Efficiencies up to 90% with a pion rejection of 100:1 can be achieved for energies above 1 GeV. Due to the length of the straws, the mean occupancy is much higher than for the SCT or pixel detectors. This makes pattern recognition in the TRT challenging.

2.2.2 The calorimeters

The calorimeters are responsible for measuring the energy carried by the different particles traversing the ATLAS detector. ATLAS makes use of different technologies for calorimetry purposes. Identification of particles that interact only through electromagnetic processes such as electrons or photons, present different requirements than particles that interact hadronically. The calorimeters use dense material to force the incoming particle to interact with the nuclei in the media producing *showers* of particles. The showers are initiated in the *absorber* material and extend into the *active* material where the energy of the shower produced is measured. The total signal collected is used to recover the energy of the incoming particle. There are two different kinds of active materials used in ATLAS, liquid argon (LAr) and tiles of scintillating plastic. LAr detectors are used in the electromagnetic (EM) calorimeters, in the Hadronic Calorimeter Endcaps (HEC) and in the Forward Calorimeter (FCal). Plastic scintillators are used in the hadronic barrel Tile Calorimeter (TileCal). The calorimeters

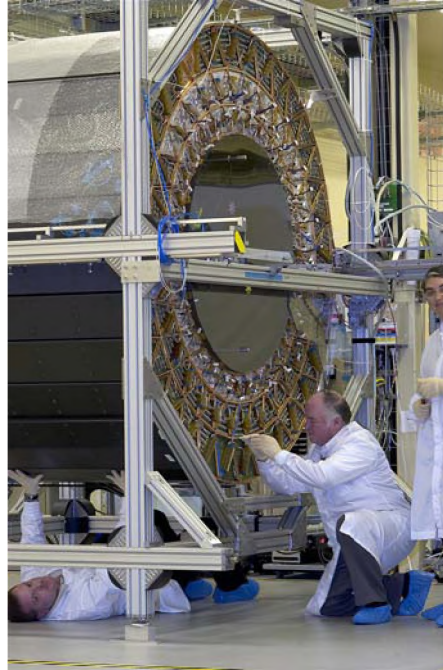


Figure 2.10: Photograph of the TRT barrel.

use different absorbing materials such as lead, iron, copper or tungsten. The calorimeters need to provide good electromagnetic and hadronic shower containment. In addition, the hadronic calorimeters must limit the amount of punch-through particles into the muon spectrometer. Figure 2.11 shows the different calorimeter systems.

Electromagnetic calorimeter

The EM calorimeter [32] surrounds the inner detector and is designed to identify and measure the energy of electrons and photons. It is divided into a barrel, situated within $|\eta| < 1.475$, and two endcaps found within $1.375 < |\eta| < 3.2$. Its granularity is especially fine in the region closest to the inner detector, making it possible to distinguish between

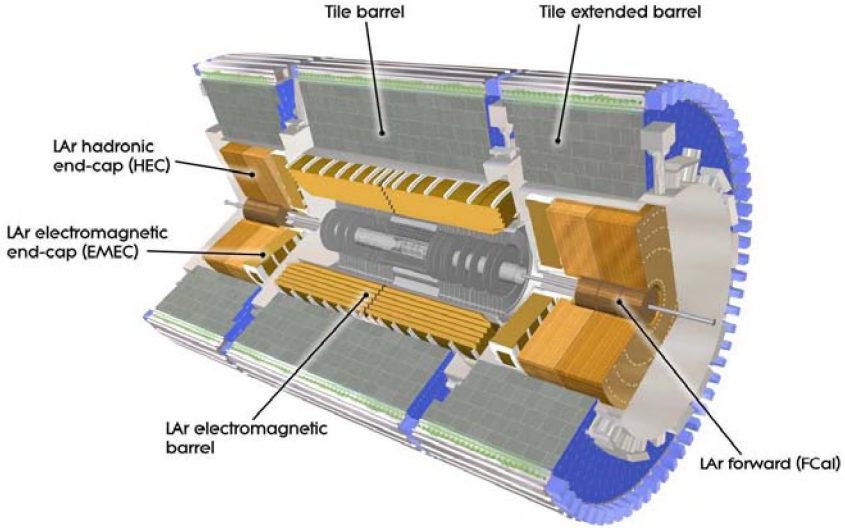


Figure 2.11: The ATLAS calorimeter system.

showers originating near to each other. In general, its granularity is enough to satisfy the criteria required for jet reconstruction and missing transverse energy E_T^{miss} estimations in ATLAS. The barrel and endcap modules are divided into three longitudinal compartments also called samplings. The first sampling has the finest granularity which allows precise cell clustering. The second sampling is thicker and is where the electrons and photons deposit the largest amount of energy. The last sampling is used to recover high energetic showers that extend beyond the second sampling, which allows to discriminate between electromagnetic and hadronic showers. In the central η region before the EM calorimeter, a presampler is located. This presampler contains 1.1 cm of LAr in the barrel and 0.5 cm in the endcaps. The energy measured in the presampler is used to correct for the energy loss of electrons and photons upstream of the calorimeter.

The EM calorimeter uses lead plates as absorbers, sandwiched between two stainless steel sheets. In the barrel the absorbers have a thickness of 1.53 mm inside $|\eta| < 0.8$ and 1.13 mm for $|\eta| > 0.8$. In the endcap, their thickness is of 1.77 mm for $|\eta| < 2.5$ and 2.20 mm for $|\eta| > 2.5$. LAr is the active material used in the EM calorimeter, filling the space between electrodes, which have an accordion-shape structure. The electrodes consist of three conductive copper layers separated by insulating polyimide sheets. The accordion geometry guarantees a complete ϕ coverage without gaps, as well as a fast extraction of the signal at the electrodes. The electrodes are separated from the lead tiles using plastic meshes. The thickness of the lead plates was optimised in order to get the best possible energy resolution measurement. Figure 2.12 shows a sketch of one of the modules on the barrel where the accordion structure is visible. The expected energy resolution of the EM calorimeter is:

$$\frac{\sigma_E}{E} = \frac{10\%}{\sqrt{E}} \oplus 0.7\%$$

where the energy E is expressed in GeV. The first term of the quadratic sum accounts for the statistical fluctuations in the shower development. Such fluctuations are due to differences in the number of particles in the shower or in the fraction of particles lost in the absorbers. The second term which is energy-independent accounts for possible calibration errors and

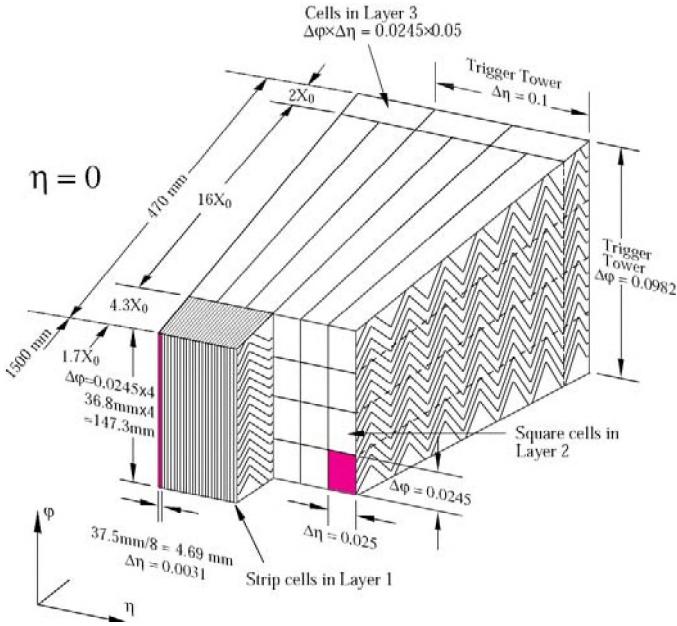


Figure 2.12: Sketch of a module of the EM LAr barrel.

non-uniformities in the electronic readout.

Hadronic Calorimeters

The hadronic calorimeter is build around the EM calorimeter. It is used to measure the energy deposited by jets of particles formed in the hadronisation of gluons and quarks as well as in hadronic decays of τ 's. The hadronic showers are much longer and wider than their EM counterparts, therefore the hadronic calorimeter needs to be much thicker than the latter. The total thickness of the hadronic calorimeter is above 10λ ; where λ , the interaction length, is the mean free path of the hadron in the given material. This amount of material is enough to stop almost all kinds of particles originating in the proton collisions, the main exceptions being the muons and the weakly interacting neutrinos. However, the hadronic interaction of high energetic particles in the calorimeter absorbers, produce a large number of slow neutrons and low energy photons that form a dense cavern background in the muon detector. The required energy resolution of the hadronic calorimeters is:

$$\frac{\sigma_E}{E} = \frac{50\%}{\sqrt{E}} \oplus 3\%$$

TileCal. The tile calorimeter [33] is placed directly outside the EM calorimeter envelope. It consists of a central barrel covering up to $|\eta| < 1.0$ and two extended barrels on each side covering the range $0.8 < |\eta| < 1.7$. The TileCal uses iron plates as absorbers. The iron plates also acting as return yokes for the solenoid magnetic field. The active material is formed by scintillating tiles that are read on two opposite sides by optical fibres. The tiles are grouped together in readout cells. The cells are almost projective in η towards the interaction point. The Tile calorimeter is separated in three different samplings. The cells in the first two samplings have a granularity of $\Delta\eta \times \Delta\phi = 0.1 \times 0.1$ and of 0.2×0.1 in the third sampling. The total number of readout channels is about 10,000. Figure 2.13 shows a



Figure 2.13: Section of the TileCal during assembling.

section of the TileCal being assembled.

HEC. The hadronic endcap calorimeter, consists of two wheels per endcap situated behind the EM endcaps. It extends from $|\eta| > 1.5$ up to $|\eta| < 3.2$, hence overlapping with both the TileCal and the FCal. This overlap ensures that the gaps in the transition regions are minimised. The HEC uses LAr as the active material for its higher tolerance to the increasing radiation doses found at large η values. It uses copper plates as absorbers. In the wheels, closest to the interaction point, the plates have a thickness of 25 mm , while in the wheels situated farthest from the interaction point they have a thickness of 50 mm . The copper plates have 8.5 mm gaps between them divided by three 1.8 mm thick electrodes. The drift spaces between the electrons are filled with LAr. These small drift spaces allow the application of small voltages, hence reducing the risk of ion build-up.

Forward calorimeter

The FCal [34] is a combination of an EM and a hadronic calorimeter. It uses copper and tungsten as absorbers and LAr as the active material. It covers the region $3.1 < |\eta| < 4.9$. It breaks up longitudinally into one EM module made of copper and two hadronic modules made of tungsten. Each module consist of a metal grid filled with concentric electrodes shaped into tubes and rods parallel to the beam axis. The gap between each rod and tube is filled with LAr. The FCal is integrated inside the same cryostat as the TileCal and HEC, reducing the amount of inert material present, hence also reducing the amount of cavern background in the muon spectrometer. The energy resolution of the FCal is:

$$\frac{\sigma_E}{E} = \frac{100\%}{\sqrt{E}} \oplus 10\%$$

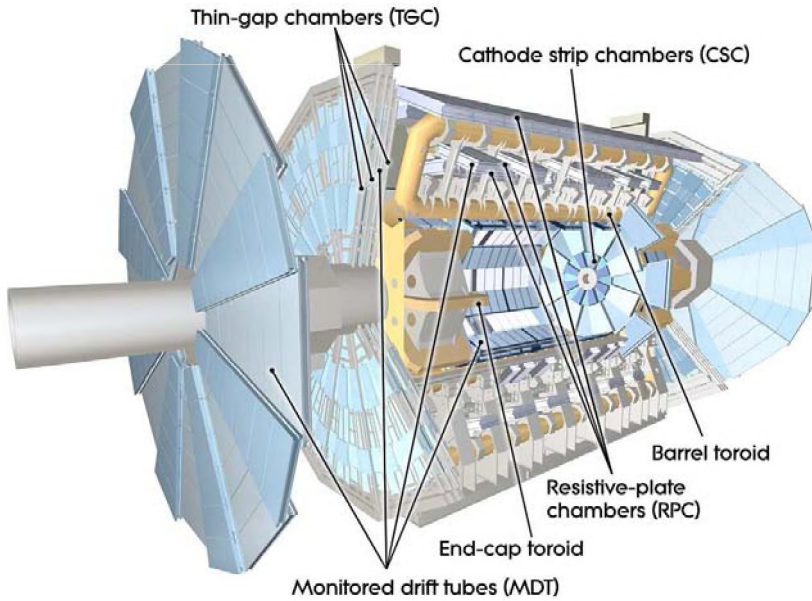


Figure 2.14: The muon spectrometer subdetectors.

2.2.3 Muon spectrometer

The layout of the muon spectrometer system [35] is shown in Figure 2.14. It is designed to detect the charged particles exiting the calorimeter. When charged particles reach the muon system their trajectories are deflected by the magnetic field created by the superconducting toroid magnets. Thus, their momentum can be measured. In the barrel region ($|\eta| < 1.4$), the trajectories are measured in three cylindrical layers of chambers arranged parallel to the beam pipe. In the endcap ($1.6 < |\eta| < 2.7$), the chambers are aligned in planes perpendicular to the beam axis. In the barrel, the deflection is caused by the large toroid coils, while in the endcap region the tracks are bent by the field generated in the endcap magnets. In the transition region $1.4 < |\eta| < 1.6$ a combination of the two types of field exist. The magnetic field is therefore mostly orthogonal to the incoming particles. The high luminosity that will be achieved in the LHC had a major impact on the design of the spectrometer instrumentation.

Four different technologies are used in the muon system. Precision-tracking chambers: Monitored Drift Tubes (MDTs) and Cathode Strip Chambers (CSCs); and trigger chambers: Resistive Plate Chambers (RPCs) and Thin Gap Chambers (TGCs). The purpose of the precision-tracking chambers is to determine the track coordinate in the plane where the trajectories are bent by the magnetic field.

The MDTs provide precision measurements over most of the pseudorapidity range $\eta < 2.7$ except for the inner most endcap wheel where they only cover up to $\eta < 2.0$. The rest of the wheel is covered by the CSC chambers. MDTs consist of aluminium tubes of 30 mm diameter, which contain a central wire working as an anode. The tubes are filled with a gas mixture of 97% Ar and 3% CO₂ at a pressure of 3 bar. A muon crossing the tube will cause the ionisation of the gas producing a net charge that will drift towards the anode. The distance between the traversing muon and the anode is measured using the time spent for the collected charge to reach the anode. This time is known as the *drift time*. The resolution of the MDT chambers is about 80 μm per tube, or 35 μm for the entire chamber.

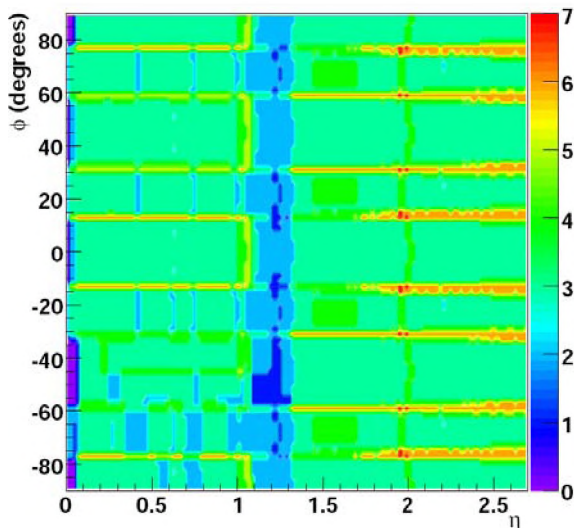


Figure 2.15: Number of MDT or CSC stations crossed by a muon for different values of ϕ and η [35].

Hits measured in the MDTs and the trigger chambers are matched ensuring a maximum of one precision measurement per triggered event.

The forward region ($2.0 < |\eta| < 2.7$) is where the particle flux is more intense. This region is covered with multi-wire proportional chambers called CSCs. Although the CSCs have a higher granularity than the MDTs, they are capable of withstanding the demanding radiation rate in this region. CSCs can measure both chamber coordinates at the same time. The first coordinate is measured using cathode strips, whilst the second is measured using strips parallel to the anode wires. The spatial resolution of the CSCs is about $60\mu\text{m}$. Multi-track ambiguities are reduced by correlating the amount of charge collected in the two planes of orthogonal strips.

For triggering purposes two kinds of multi-wire proportional chambers are used in the muon system: RPCs in the barrel and the TGCs in the endcaps. The RPCs are made of two superimposed Bakelite plates with narrow gaps filled with $\text{C}_2\text{H}_2\text{F}_4$ gas and covered with readout strips. The strips on the two plates are orthogonal to each other, allowing the measurement of both coordinates at the same time. The trigger chambers provide bunch crossing identification and well defined p_T triggering thresholds.

In the regions occupied by the muon system services, especially around $|\eta| < 0.1$ and $1.2 < |\eta| < 1.4$, the spectrometer presents limitations. Figure 2.15 shows these limitations as the number of stations in precision chambers being traversed by a muon track as a function of both ϕ and η .

2.2.4 The forward detectors

Three small detectors are situated in the forward region of ATLAS. Two of these detectors are used to measure the luminosity delivered at the LHC. The LUCID detectors (Luminosity measurement using Cerenkov Integrating Detectors) are situated at 17 m outside both ends of the ATLAS cavern. They are designed to measure inelastic $p-p$ scattering in the forward direction. The ALFA (Absolute Luminosity For ATLAS) detectors are located at $\pm 240\text{ m}$ of the ATLAS cavern and consists of tracker fibre scintillators mounted inside Roman pots.

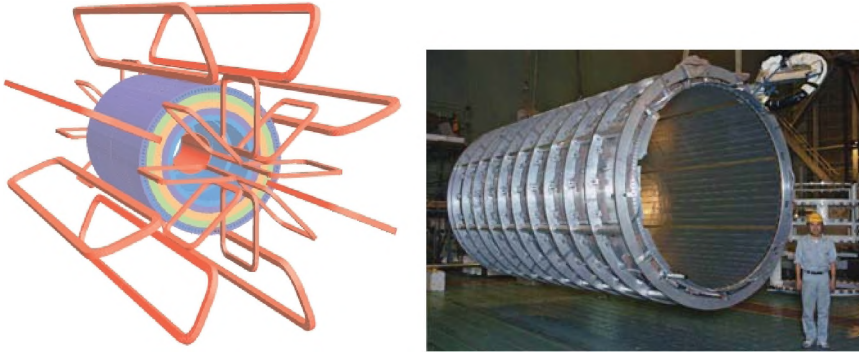


Figure 2.16: Schematic view of the complete magnet system including the calorimeter steel (left) and a picture of the solenoid magnet (right).

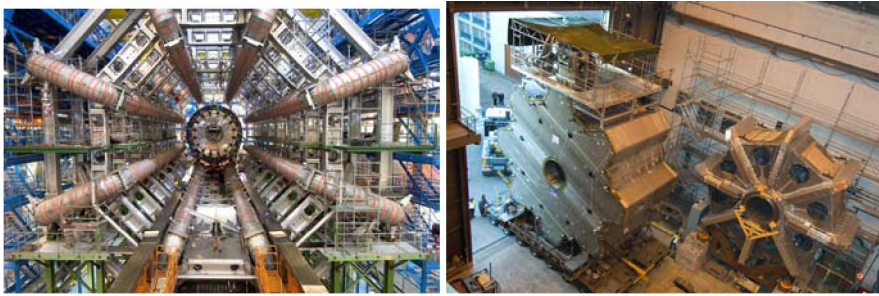


Figure 2.17: The toroid magnet barrel (left) and endcaps (right).

They are designed to get as close to the beam as 1 mm . The ZDC (Zero Degree Calorimeter) is located at $\pm 140\text{ m}$ and is designed to measure the energy of neutral particles in pseudo-rapidities above $|\eta| > 8.2$. The ZDC measurements are used to determine the centrality of the heavy ion collisions.

2.2.5 The magnet system

The ATLAS magnetic system [36] is formed by four superconducting magnets. A solenoid magnet [37, 38] which surrounds the inner detector is responsible for the bending force inside the inner tracker system. The toroidal magnetic field [39] that bends the trajectories of charged particles in the muon system. It is formed by a toroidal barrel [40] and two endcaps [41]. The total dimensions of the magnet system are 22 m in diameter and 26 m in length, being capable of storing a total amount of energy of 1.6 GJ . Figure 2.16 shows a schematic view of the ATLAS magnet system and a picture of the solenoid magnet. Figure 2.17 shows pictures of both the barrel and endcaps toroid magnets. The bending power of the toroid magnetic field is fairly smooth through η except for the barrel-endcap transition (see Figure 2.18).

The central solenoid provides a 2 T axial magnetic field and was designed to keep the amount of material before the calorimeters as low as possible. The contribution of the solenoid to the total material thickness is only 0.66λ [42]. The toroid barrel magnet consists of eight coils encased in stainless steel vacuum vessels. The overall size of the barrel toroid magnet is 25.3 m in length, with an inner radius of 9.4 m and an outer radius of 20.1 m . The

toroid endcap magnets generate the magnetic field required to measure the track momentum in the muons spectrometer endcaps. Each endcap consists of a single cold mass made of eight squared coils and eight keystone wedges. The same technology is used for the barrel and endcap toroids and is based on a pure Al-established Nb/Ni/Cu conductor wound into pancake-shaped coils. A total of five weeks are required to cool down the 360 tonnes toroid barrel to the working temperature of 4.6 K.

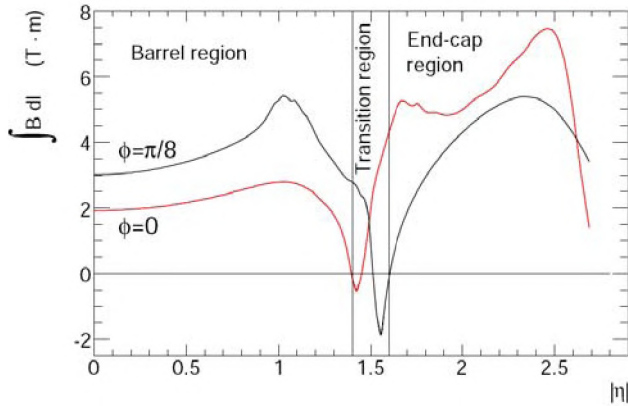


Figure 2.18: The toroid integrated magnetic field as a function of η for two different ϕ angles [39].

2.2.6 The trigger system

The LHC will provide a bunch crossing rate of 40 MHz while the average event in ATLAS has a size of 1 MB. It would be impossible to store all that data. However, the vast majority of the collisions do not produce any interesting physics process and therefore do not need to be recorded. The trigger system in ATLAS has been designed to bring the rate down to about 100 MB/s while keeping as many of those precious events as possible. Figure 2.19 shows the two levels in which the trigger system is divided: the hardware based Level-one trigger [43] (L1) and the software based High Level Trigger [44] (HLT). The HLT consisting of two subsystems: Level-two trigger (L2) and Event Filter (EF).

The high rate requires very fast decision making, hence, the L1 trigger algorithms are required to run within 2 μ s. Both the calorimeter and muon system information are used by the L1 algorithms. However, to speed up the process, the L1 trigger only uses reduced granularity areas in $\Delta\eta \times \Delta\phi$ known as Region of Interests (RoI). In the muon spectrometer, a rough estimate of the muon transverse momentum is obtained using the hits in the RPC and TGC chambers. The calorimeter trigger is based on the total and missing transverse energies measured in the event. If the established criteria is passed, the pre-processed data for all subdetectors is stored in Read-Out Buffers (ROBs). The L1 trigger is able to bring down the rate from 40 MHz to 75 kHz.

The algorithms running as part of the L2 trigger have access to all the data in the event, including the inner detector information. However, for time performance purposes, the L2 trigger only retrieves the data corresponding to the RoI defined by L1. Depending on how busy an event is, the total latency time of the L2 trigger may vary from 1 up to 10 ms. The L2 trigger reduces the rate to 1 kHz.

The EF is based on the offline reconstruction algorithms and uses the full granularity of

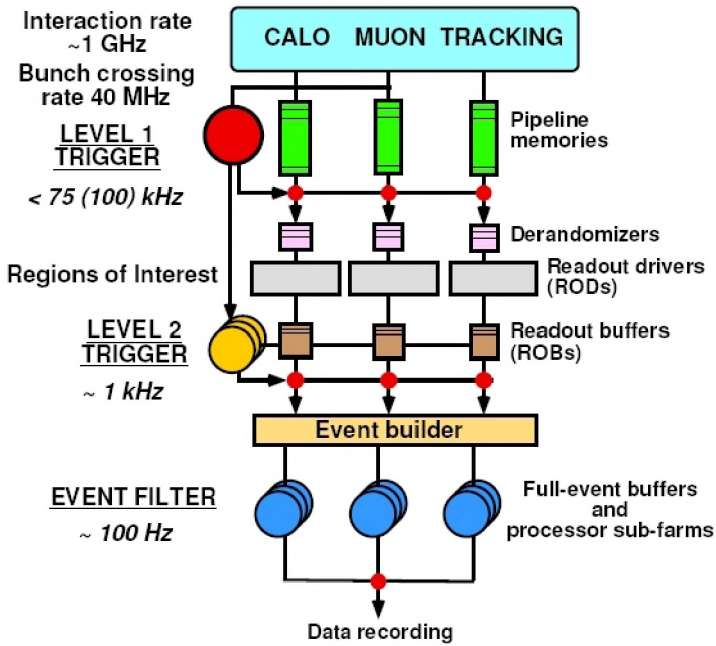


Figure 2.19: Schematic view of the ATLAS trigger system.

the event. The EF algorithms reduce the rate to 200 Hz, taking an average of 4 s to process every event. So 100 MB/s are finally stored on tape for subsequent process by the offline reconstruction software .

CHAPTER 3

MUON RECONSTRUCTION

The ATLAS muon spectrometer is designed to achieve good reconstruction efficiency and momentum resolution for muons with energies ranging from a few GeV up to 1 TeV. The development of dedicated software ensures the reconstruction of the measured position, direction and momentum of the muons. This chapter presents the different strategies that are part of the ATLAS reconstruction software. In this chapter, the tracking procedure is discussed for both tracking systems, the inner detector and the muon spectrometer. Also a study of the performance of the different muon reconstruction and identification algorithms is discussed. In order to understand the different aspects of the ATLAS reconstruction software, it is essential to be familiar with the general concepts of the software control framework ATHENA [45].

3.1 The ATHENA control framework

The results presented in this thesis are obtained using ATHENA version 13.0.30. ATHENA is a concrete implementation of an underlying architecture called Gaudi [46]. The Gaudi project, which was originally developed for the LHCb experiment, was adopted as the kernel of ATLAS reconstruction software. The framework provides a set of defined interfaces:

- All classes inheriting from the `Service` class, are controlled by the central `ExtSvc` manager, which handles their initialisation and finalisation. The instances of this kind of classes are designed to provide functionalities that might be required at any stage of the program execution. Examples of such functionalities are, to provide access to the central data storage, or the message and histogramming services.
- Instances of classes inheriting from the `Algorithm` class are meant to run actions that will take place once for every event and are registered to the `ApplicationMgr`. This task manager controls the initialisation, execution and finalisation of the instances. Examples of actions that are typically done by `Algorithm` classes are the retrieving of data collections from the transient storage, data preparation and running of `AlgTool` classes.
- Finally, instances for `AlgTool` classes provide algorithm tools that will be executed a number of times for every event. `AlgTool` instances are retrieved from the detector store. These instances can be owned by the `Algorithm` class where they are executed, or can be retrieved from the central `ToolSvc`, where all public tools are registered, allowing `AlgTool` instances to be shared by more than one `Algorithm` class.

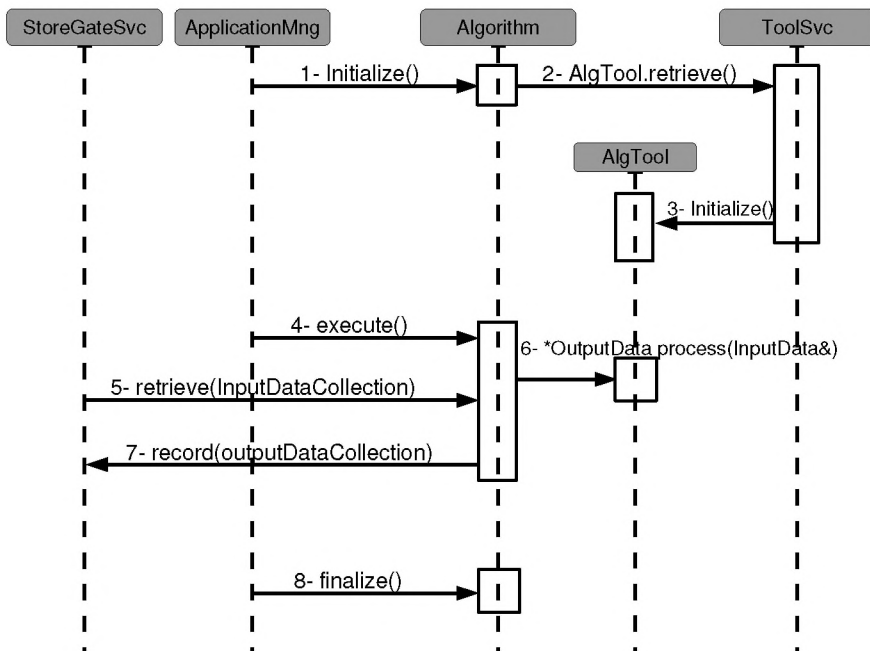


Figure 3.1: A simplified diagram for the data flow and algorithmic sequence within the ATHENA framework. The *Algorithm* classes are registered to the *ApplicationMgr* that executes the *initialize()* interface method at the beginning of the run, the *execute()* is called for every event and the *finalize()* method in the job termination phase. The *initialize()* call to the *Algorithm* may trigger the retrieval of an *AlgTool* from the *ToolSvc*, if the instance of the *AlgTool* is not owned by the algorithm.

An *Algorithm* typically retrieves input and writes output data collections to the transient event store. This action is done using the service *StoreGateSvc*. The *ApplicationMgr* is responsible for running each algorithm in the correct order, defining the reconstruction sequence. Figure 3.1 shows a schematic view of a simple process.

3.2 Track reconstruction in the inner detector

The ATLAS track reconstruction strategy in the inner detector [47], combines the classical concepts of *pattern finding* and *track fitting*. The reconstruction starts with a global pattern search, followed by a local pattern recognition and track fitting. Therefore, local pattern recognition only runs on the reduced output produced by the global search. The primary pattern recognition follows an inside-out strategy to find the track candidate.

The first step in track reconstruction is the creation of a three-dimensional representation of the *hits* in the pixel and the SCT silicon detectors. For pixel hits this is simple, since the measurement already gives a two-dimensional hit in each detector surface. In the case of the SCT clusters, the silicon sensors have a sandwich structure; with one or two pairs glued together in parallel, but rotated by a fixed stereo angle. This angle difference makes it possible to reconstruct a three-dimensional hit. Since two simultaneous measurements are required in each SCT module, the three-dimensional object reconstruction also works as a noise reduction mechanism.

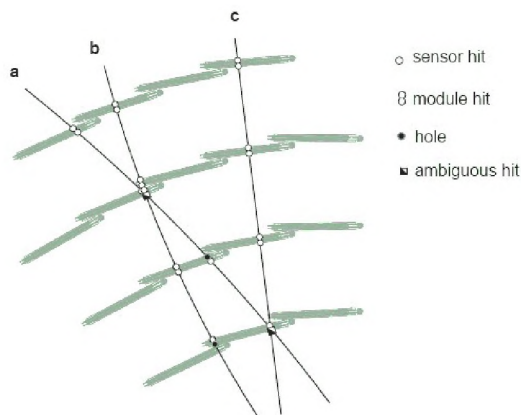


Figure 3.2: Possible ambiguity in the hit association to the different tracks. A scoring strategy is used to solve this ambiguity [47].

The next step is the track seed finding. First, pairs of pixel hits are used to build z vertex candidates. This information is used to perform a fast primary vertex reconstruction, which constrains further the seeds, making it possible to associate three or more hits to them. Once the seeds are found the silicon pattern recognition starts. There is already enough directional information in the seeds to begin the building of the paths through the different detector elements and to associate other hits to the track candidate. SCT measurements that were not used during the building of the three-dimensional hits, and are located in the path laid out by the seed, are also used in this first track fitting. For this, the algorithm `GlobalChi2Fitter` [48] is used.

The `GlobalChi2Fitter` algorithm is based on the scattering angle formulation of the track fit. It needs an initial estimate of the covariance matrix but not of their errors, which is an advantage over traditional Kalman fitters. Additionally, the fit yields the scattering angles that can be used in alignment procedures. On the other hand, the algorithm needs to invert large matrices making it desirable to limit the amount of track parameters used.

The `GlobalChi2Fitter` algorithm delegates a number of tasks to other modules inside the common tracking framework. The propagation of the track parameters is performed by the `Propagator AlgTool`. This is the same tool used by the `Extrapolator` package that will be described in Section 3.3. The material effects are included through the `DynamicLayerCreator` which gets the material information from a dynamic configuration of the `TrackingGeometry`. The `TrackingGeometry` [49] will be described in detail in Section 3.3.2.

The seed search results in a high multiplicity of track candidates. Their number needs to be reduced before any extension into the TRT detector can be attempted. The candidates may be incomplete, share hits among them or describe fake tracks. To resolve these ambiguities the candidates are ranked in their likelihood of describing the real trajectories of

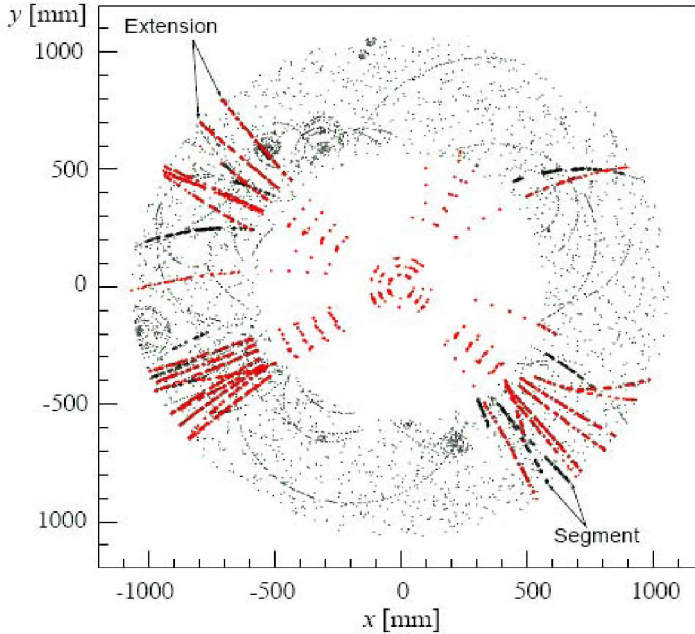


Figure 3.3: Example of the extension of the silicon seed candidate track into the TRT hits [47].

particles. First, the track is refitted using more accurate geometry information that includes a detailed material description. Then, a scoring strategy is deployed.

The scoring procedure gives different weights to hits in different subdetectors, e.g. preferring the more accurate pixel clusters over the SCT strips. Figure 3.2 shows an example of a possible scenario where there is an ambiguity in assigning hits in the SCT Barrel to different tracks. Tracks *a*, *b*, and *c* share several hits. In this example, a module hit representing measurements on both sides of the SCT silicon detector score relatively higher than two single hits with no associated backside module. Also, hits in an overlap region are preferred, as in the case of track *b*. Holes on track (no hit is found where expected) lead to a penalty in the track score. Shared hits are associated to the candidates with the higher score.

Once the collection of track seeds is created, they are extended to incorporate the TRT hits. This is done on a track by track basis without any modification of the silicon seeds. The extension follows a classical approach of track finding through track extrapolation. A line fit decides which hits are compatible with the track seed. Once all the possible hits are associated to the track, a complete refit together with a new scoring analysis is performed. If the score after the refitting is lower than in the initial silicon seed, only the original silicon seed is kept.

The track reconstruction strategy has some limitations. Ambiguous hits can shadow the track seed in the silicon detectors and render the scoring strategy useless. Particles originating in secondary vertices, or photon conversions, may not have enough silicon hits to accurately build the silicon seed. In order to overcome these limitations an outside-in reconstruction is also performed. A dedicated segment recognition algorithm runs over the TRT hits and the seed candidates are back-tracked towards the silicon hits.

A global pattern search is used to find the segments in the TRT. Since the TRT does not provide information in the direction of the drift tubes, the pattern recognition runs in

projective planes ($r - \phi$ planes in the barrel and $r - z$ in the endcap). Here, it regards tracks with a transverse momentum above 500 MeV/c as straight lines. A Hough transform [50] clusters the hits lying in straight lines into one single cell on a two-dimensional histogram. The segment search is reduced to find the local maximum of the histogram. Figure 3.3 shows an example of the tracks that are extended to the TRT modules in a $t\bar{t}$ event. The brighter hits are associated to the silicon seeds and their extensions into the TRT. The black dots represent the TRT hits that have been associated to segments by using a pattern recognition directly on the TRT hits.

Reconstructed tracks are generally expressed as a set of parameters and their covariance matrix with respect to a reference surface. The set of parameters chosen to describe the tracks near the interaction point $P = (x_P, y_P, z_P)$ are referred to as *perigee parameters*:

- d_0 , signed transverse impact parameter. $d_0 = \pm \sqrt{x_P^2 + y_P^2}$.
- z_0 , longitudinal impact parameter.
- ϕ , azimuth angle of the track direction at P.
- θ , polar angle of the track direction at P. $\cot \theta = \frac{p_z}{\sqrt{p_x^2 + p_y^2}} = \frac{p_z}{p_T}$.
- $\frac{q}{p}$, signed charge over the track momentum. $\frac{q}{p} = \frac{q}{|\vec{p}|}$.

Other reference surfaces are also possible, like the entrance to the calorimeters or the muon spectrometer.

3.3 Track extrapolation

The ATLAS reconstruction software uses the Extrapolator [51] package in many different contexts. The Kalman fitter formalism utilises extrapolated silicon seeds to extend the tracks to the TRT detector. Global fitting techniques rely on the correct treatment of the effects caused by the particle interaction with the detector material. Vertex finders iteratively estimate the track vertex position until they reach convergence. The parameters of the track on a destination surface in the calorimeter are used to match the track to active cells. Finally, if the destination surface is the entrance of the muon spectrometer, the information can be used to match the inner detector track with muon segments.

The extrapolation transports the track through the magnetic field by solving the equations of motion of the particle. Since the magnetic fields in ATLAS are highly inhomogeneous, it is necessary to use numerical methods to solve the second order differential transport equations

$$\frac{d^2 \mathbf{r}}{ds^2} = \frac{q}{p} \frac{d\mathbf{r}}{ds} \times \mathbf{B}(\mathbf{r}) + g(p, \mathbf{r}) \frac{d\mathbf{r}}{ds},$$

which include an energy loss function. r represents the position of the particle along the trajectory s , and \mathbf{B} is the magnetic field.

The extrapolation software uses the Runge-Kutta-Nyström [52] formalism to solve these equations. A distance cut-off determines the last step of the numerical iteration. A Taylor expansion is used to make the final propagation to the destination surface. Figure 3.4 shows an example of a typical extrapolation process.

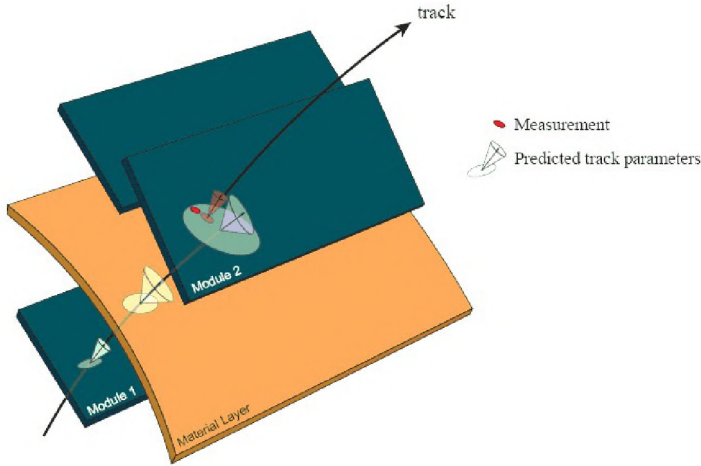


Figure 3.4: Example of the extrapolation process. The track parameters and covariance matrices in the detector module 1 are propagated to a destination surface in module 2. All the material effects responsible for increasing the uncertainty in the extrapolated parameters are associated to a single material layer [51].

3.3.1 Material effects

There are two main processes that describe the interactions of the particles traversing material: energy loss and multiple Coulomb scattering. Multiple scattering can be regarded as a stochastic process of zero mean, i.e. the extrapolation only modifies the track parameter covariance matrices and not the parameters themselves. The calculation is done using the Highland formula [53], which is an empirical correction to Molière’s solution of the transport equation [54]. Highland expanded the model by adding an empirical logarithm term to the expression of the root mean square projected scattering angle (σ_{rms}^{proj}):

$$\sigma_{rms}^{proj} = \frac{13.6MeV}{\beta cp} Z \sqrt{t/X_0} [1 + 0.038 \ln(t/X_0)]$$

X_0 is the radiation length and t is the thickness of the material. This additional term corrects for the underestimation in the Coulomb screening. Figure 3.5, shows a possible multiple scattering process.

Ionisation is the main cause for the energy loss for muons traversing the material with energies ranging from 1-100 GeV. Ionisation is an effect of the order α^2 , where $\alpha \approx 1/137$ is the fine structure constant. Other processes such as *bremstrahlung* (α^3), direct pair production (α^4) and photo-nuclear interactions have minor contributions. This energy loss is typically small in comparison to the initial momentum of the particle and it can be regarded as mean average energy loss with a small variance. The Bethe-Bloch formula [56]:

$$\frac{dE}{dx} = \alpha^2 2\pi N_a \lambda_e^2 \frac{Z m_e}{A \beta^2} \left[\ln \frac{2m_e \beta^2 \gamma^2 E'_m}{I^2(Z)} - 2\beta^2 + \frac{E'_m}{4E^2} - \delta \right],$$

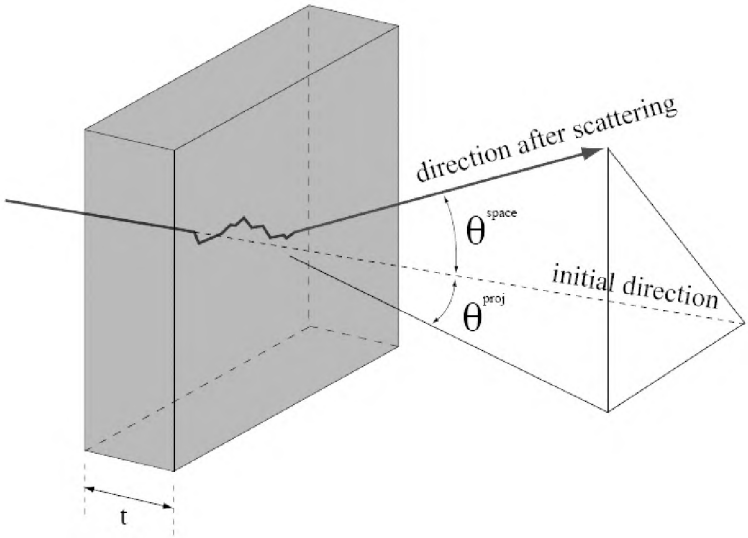


Figure 3.5: Representation of a multiple scattering process for a muon traversing dense material [51].

describes the mean energy loss of a muon per unit of length x due to ionisation loss. N_a is Avogadro's number. Z and A are the atomic number and weight of the medium. m_e is the electron mass. $\beta = p/E$ is the particle's momentum over energy ratio. $\gamma = E/m$. $\lambda_e = 3.8616 \cdot 10^{-11} \text{ cm}$ is the Compton wavelength of the electron. $I(Z)$ is the mean ionisation potential of the electron. δ is the density correction [57]. Finally, E'_m :

$$E'_m = 2m_e \frac{p^2}{m_e^2 + m_\mu^2 + 2m_e \sqrt{p^2 + m_\mu^2}}$$

is the maximum energy that can be transferred to the electrons in the medium.

Figure 3.6 shows the range of energies where the Bethe-Bloch approximation can be used to describe the energy loss of muons in copper. Similar behaviour can be expected in other materials such as iron or liquid argon. Muons with energies ranging from a few, and up to several hundreds GeV, can be regarded as *minimum ionising particles* when traversing the material in the different subdetectors.

The Bethe-Bloch formula gives a value for the mean energy loss of the muons. A Landau distribution [58] is used to find the most probable value (MPV) of the energy loss of a particle traversing a thin material:

$$MPV = \frac{ZN_a kt}{\beta^2} \left[\ln \frac{2mc^2 \beta^2 \gamma^2}{I} + \ln \frac{ZN_a kt}{\beta^2 I} + 3.647 \right]$$

In order to simplify the calculations gaussian distributions can be used model the Landau distributions as is shown in Figure 3.7 . It presents the energy loss distribution for single muons with an energy of 5 GeV traversing 4.68 mm (i.e. 5% X_0) of silicon.

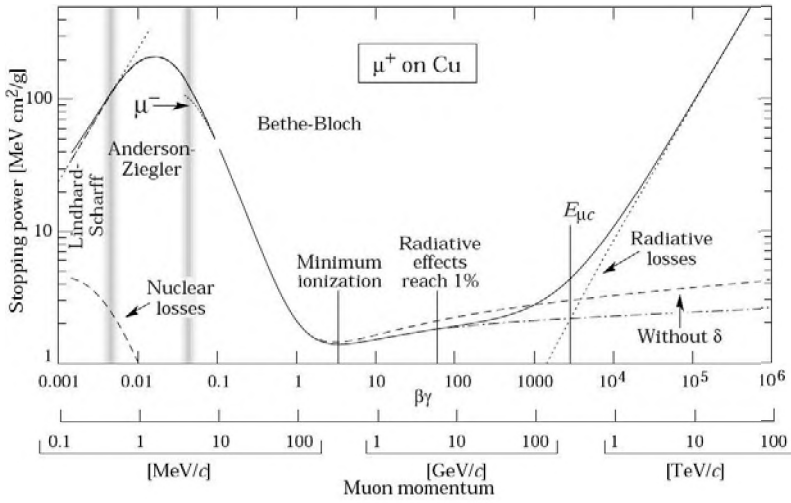


Figure 3.6: Mean energy loss ($\langle -dE/dx \rangle$) per unit length (in g/cm^2) for muons in copper [55].

3.3.2 Tracking Geometry

When a particle traverses dense material, it interacts with the atoms in the medium. These effects need to be taken into account in order to perform an accurate extrapolation. During the extrapolation process the positions and dimensions of the sensitive detector elements need to be known. The extrapolation software gathers the necessary information about the amount and type of material traversed by the track from the `TrackingGeometry` tool. The `TrackingGeometry` is a simplification of the `GEANT4` geometry [59]. The direct use of the `GEANT4` or the ATLAS detector description `GeoModel` [60] in the tracking algorithms, would impose an unbearable burden in terms of CPU time. Thus, a simplified geometry description is used in the extrapolations through the detector.

All the geometrical objects, such as `Layer` and `Volume`, defined in the `TrackingGeometry`, are based on the `Surface` class. The `Surface` objects are the input of the track extrapolation. Thus, they are the natural reference frame for the representations of the track parameters. Additionally, the coordinate transformations made during track finding and fitting are also delegated to the `Surface` class. This guarantees consistency between the different coordinate systems. In addition, the `Surface` class is used to build the interface of the reconstruction algorithms with `GeoModel`. The `Surface` objects represent measurement surfaces as obtained from `GeoModel` and therefore are linked to the ATLAS detector description database. This guarantees the correct alignment of the surfaces with respect to the latest conditions data. The different shapes of surfaces (e.g. planar, cylindrical, disc) are based on intrinsic local coordinate systems in each part of the subdetectors. Hence, establishing a coherent definition of the track parametrisation with respect to the measured coordinates in each subdetector. The different subdetector volumes are then characterised by a set of confining boundary surfaces.

Since the material information is still missing in the `Surface` and `Volume` classes, they are pure geometrical entities which cannot describe any physical or logical objects in the detector model. Relevant information is also missing when a `Volume` is used to represent the magnetic field. As is the case when a parametrised field description is used during tracking.

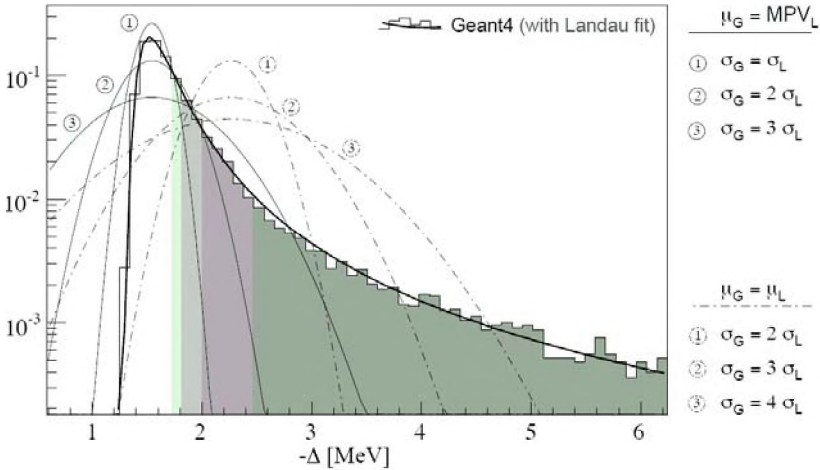


Figure 3.7: The energy loss distribution for single muons with an energy of 5 GeV traversing 4.68 mm of silicon [51]. The arbitrary units in the vertical axis were scaled such that the sum of weights is the unity.

The use of such parametrisation of the field is necessary to reduce the CPU time spent in algorithms that need to access the field information very often. In order to overcome these limitations, the concept of Layer is introduced. A Layer object is simply a combination of a Surface together with the material description. TrackingVolume extends the Volume class incorporating information about both material and magnetic field descriptions. In addition, a TrackingVolume may contain a set of confined layers or volumes. These definitions are useful in order to create hierarchical structure of the TrackingGeometry.

The navigation actions inside the TrackingGeometry can be either static or dynamic. The static navigation consists of an alternating sequence of navigation layers and material layers. The navigation layers are just place holders pointing to the next material layer in the extrapolation. In a dynamic navigation style, the different layers are created on demand during the track extrapolation. This allows the user to define the level of detail for the geometry used in the extrapolation process. Figure 3.8 shows an example of a static configuration implemented to represent the geometry of the SCT barrel.

The TrackingGeometry class is situated on the top of the tracking geometry hierarchy. It holds the different TrackingVolume objects that represent the entire detector. This schema guarantees a unique association between local and global coordinate systems. When building TrackingGeometry specific information about detector structures is gathered from GeoModel.

When all the systems are enabled the tracking geometry is build inside-out. The inner detector is built first, then the calorimeters, and finally the muon system is wrapped around them. However, this model is versatile in the sense that each system geometry is independent from the other two, making it possible to build only one or two of the three geometries. Additionally, a call-back mechanism enables an to update the alignment information during

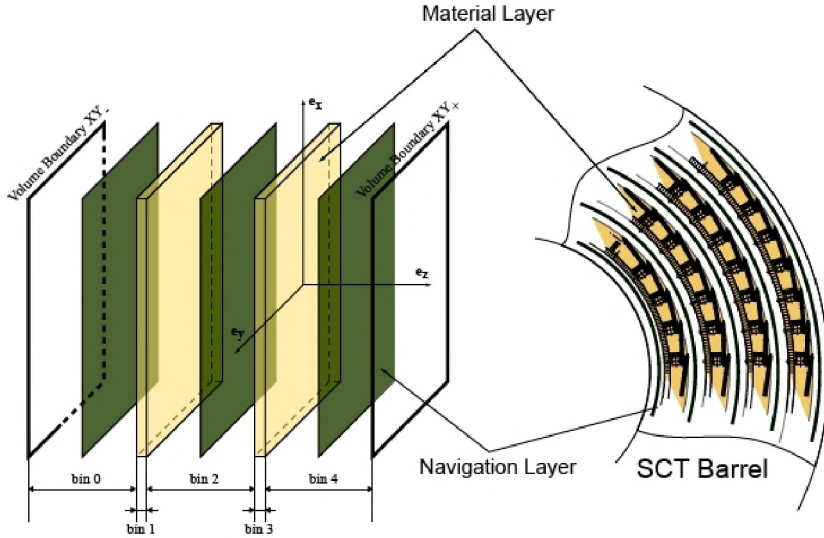


Figure 3.8: Example of a *TrackingVolume* containing three material layers (bright) and four navigation layers (dark). The figure on the right shows the implementation for the SCT Barrel layers[51].

the reconstruction run.

The inner detector *TrackingGeometry*

The building of the inner detector starts by building the pixel and SCT subdetector geometries. The overall dimensions of the silicon detector are determined from *GeoModel*, and the *Layer* objects created accordingly. The inner detector *TrackingGeometry* can be adapted to different layouts and misalignment configurations. The *Layer* objects for the TRT are, in general, not built by parsing the sensitive detector elements from *GeoModel*. The material in the TRT is almost continuously distributed, hence it is possible to simplify the TRT geometry placing a set of layers along its volume. The inert material in the TRT subdetector is modelled by inserting layers with condensed material information.

The calorimeter *TrackingGeometry*

It is possible to build the calorimeter *TrackingGeometry* following static or a dynamic configurations:

- The static configuration is very detailed and in fact very close to the actual *GeoModel* description. It includes several volumes that can be either continuous (i.e. *TrackingVolume* based) or point-like (i.e. *Layer* based). Both types are provided with material update mechanisms. The positions of the inserted layers are retrieved directly from GEANT4. This allows algorithms that need to extrapolate tracks to, or through the calorimeter, to get the exact position for the samplings as described in the *TrackingGeometry*. This also guarantees an optimal description of the calorimeter material for extrapolations between sensitive samplings

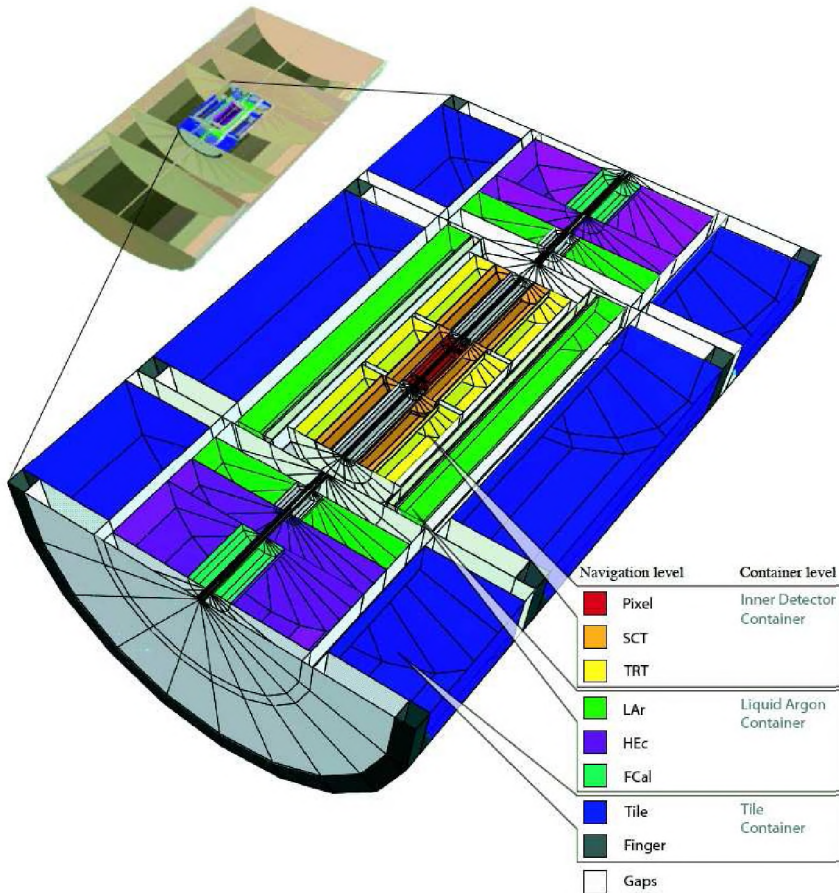


Figure 3.9: Schematic representation of the Tracking Geometry. Both the inner detector tracker and the different calorimeter sub-detectors are shown.

- Alternatively, a dynamic configuration can be used. In this configuration the Layer objects used in the extrapolation are created on demand, allowing the user to specify the level of detail required.

Figure 3.9 shows a schematic view of the combined inner detector and calorimeter tracking geometries in the static configuration. The Layer objects are omitted in this illustration, only the volumes are shown.

The tool `TrackingGeometryValidation` can be used to automatically validate the calorimeter `TrackingGeometry`. It outputs the material description in the `TrackingGeometry` in a format identical to that of GEANT4's, which is stored in the database, making their comparison easier.

The muon `TrackingGeometry`

The muon `TrackingGeometry` is built around the calorimeter volume. When building the muon geometry alone, a dummy volume is built to represent the calorimeter envelope. In the muon system the material objects are represented by detached volumes. The active material

is made of `Layer` objects in a way that allows a unique association of the layers with the surface positions in `GeoModel`. The passive material is represented by `Volume` objects.

3.4 Muon identification

The ATLAS software implements different strategies for muon reconstruction and identification. The more direct approach is the *standalone* muon reconstruction. It finds tracks in the muon spectrometer and then extrapolates them back to the beam pipe. Track reconstruction in the spectrometer is even more challenging than in the inner detector. Firstly, there is more material that needs to be accounted for. Secondly, the distance between hits can go up to several meters, increasing the risk of inaccuracies during the extrapolations. In addition, the magnetic field map has large variation gradients making the fitting procedure especially difficult near the coils.

Combined Muons are found matching the standalone and inner detector tracks, then refitting the result into a global track. *Tagged* muons are found by extrapolating the inner detector tracks to the spectrometer and searching for hits associated to the track. Calorimeter tagging algorithms identify inner detector tracks using the distinctive energy deposition pattern associated to minimum ionising particles.

Several independent algorithms that implement these strategies have been developed. The algorithms are grouped into families and the output data intended to be used in the physics analysis include three different collection of muons: The `Staco` [61] and the `Muid` [62] are the main families and include standalone, combined, and tagging algorithms. The last family, `CaloTrkMuid`, includes calorimeter based muon tagging algorithms. The implementation and performance of one of such algorithms will be discussed in depth in the next chapter.

3.4.1 Monte Carlo samples

To evaluate the performance of the algorithms an inclusive $Z \rightarrow \mu^+ \mu^-$ and a $t\bar{t}$ samples are used. The $Z \rightarrow \mu^+ \mu^-$ was generated with PYTHIA [63]. During the generation process, in the $t\bar{t}$ sample case, the presence of at least one lepton (electron, muon or tau) was required. This sample was generated using MC@NLO [64] and Herwig [65]. The sample contains muons produced through two different mechanisms: *direct* muons produced in the leptonic decay of a W -boson and *indirect* muons produced in the decay tree of b or c quarks. The results which follow make use of the direct muons only.

3.4.2 Standalone muons

There are two algorithms for track reconstruction in the muon spectrometer. `Muonboy` [61] is the standalone algorithm belonging to the `Staco` family and `MOORE` [66] which belongs to the `Muid` family. Their purpose is to determine the momentum and trajectories of the muons passing through the spectrometer. This reconstruction is performed in different steps. The first step is the pattern recognition. Its aim is to group the hits that belong to the same trajectory thus giving a first estimate of the track parameters. This first estimate is necessary to perform the track fitting, which attempts to find the best possible parameters for a given trajectory.

The muon spectrometer has a coverage of $|\eta| < 2.7$, which is larger than the coverage of the inner detector ($|\eta| < 2.5$). The muon reconstruction algorithms have to cope with a number of difficulties due to the layout of the spectrometer:

- A track typically traverses three stations in its way through the spectrometer. Although the position at those three points is known with good accuracy, the large distances in between stations result in large extrapolation errors.
- The large inhomogeneity of the toroidal magnetic field, especially near the coils, causes inaccuracies in the extrapolation of the particles through the field.
- A very detailed knowledge of the inert material in the toroids and support structure is required to obtain a good estimate of the amount of material traversed by the particle. Notice that the inert material accounts for most of the material present in the spectrometer.
- The large amount of cavern background, which consists mainly of thermalised slow neutrons and low-energy photons increases the spectrometer occupancy, complicating the pattern recognition.
- The MDT chambers only measure the η coordinate, requiring synchronisation with the trigger chambers (RPC and TGC) in order to obtain the ϕ coordinate measurement.

Therefore, the standalone algorithms need an accurate geometry description to correctly take into account the amount and type of material in the tracking procedure. Alignment and deformation corrections to the nominal position of the chambers is performed by the alignment services. Access to the calibrated data is obtained through the subdetector calibration services. The intensity of the magnetic field needs to be known in great detail during tracking. Dedicated sensors are installed all through the spectrometer to accurately measure the magnetic field. Again, the algorithms can obtain the magnetic field map through a dedicated software service.

The first step in the track reconstruction is the definition of a *hit* in each technology. For example, in the MDTs a hit is produced after converting the TDC (time to digital converter) measurement into a space coordinate. In the CSCs, the hit is produced after applying the appropriate clustering methods to the digitised measurements.

Muonboy, defines regions of activity (ROA) of $\Delta\eta \times \Delta\phi = 0.4 \times 0.4$ around hits found in the RPCs and TGCs trigger chambers. Afterwards, all the MDT chambers intersecting the ROA are used in the segment finding, generating two-coordinate (η, ϕ) pair points. The pairs are required to roughly point towards the interaction vertex in order to suppress the combinatorial possibilities and reduce the chances of fitting fake tracks. The track candidates are then extrapolated to the remaining tubes of the MDT stations and matched with the recorded hits to remove ambiguities. A segment is fitted using a straight line minimisation, and considered valid if it contains at least two hits in each of the two multi-layers and if the fitted χ^2 is below a certain value.

The momentum of the candidate track can be estimated from the position and direction of segments found in the outer and middle stations. The segments are then extrapolated through the magnetic field to the first middle or inner station. In this extrapolation different values around the the momentum estimate are used, which is known as *momentum scan*. The best matching segment, in both position and direction, found in the next station is included in the candidate track. The track is then fitted using a minimisation procedure, leading to a more accurate estimate of the momentum. The material in the chambers and the inert material traversed by the muon, are separated into a set of scattering centres. The corresponding scattering angles are free parameters in the fit, and their gaussian distribution added as a constraint in the χ^2 function. A second momentum scan around the improved

momentum estimate is performed and the track candidates are extrapolated to other potentially traversed stations. Any matching segment in these stations is included in the candidate track. The candidate is kept only if it contains a minimum of two segments. A global fit is performed using the results obtained. However, this time the raw information (i.e. the TDC values and hit strips) is used in the fit. The final selection of the reconstructed tracks is made using the value of the χ^2 per degree of freedom obtained in this last global fit.

The MOORE muon reconstruction starts with the CSC segment making. The hits are clustered fitting the charge deposition on several strips of one chamber. The η and ϕ clusters are fitted separately using a straight line fit. The seeding is performed combining clusters from each of the four layers. These combinations produce two-dimensional segments with a direction in space. The obtained 2D segments are then combined into full 3D segments. In the MDTs, the η hits are combined into segments using a χ^2 minimisation procedure. These segments need to have a minimum of three hits to be accepted. If the χ^2 per degree of freedom for a given segment is above 10, the hit with the largest contribution is dropped, and the segment is refitted. In this refit new hits can be associated to the segment. When the segments are successfully built, the hits found in the trigger stations (RPCs and TGCs) are associated to them.

Once the collection of segments is obtained, a segment selection is performed in order to remove ambiguities (such as hits shared by more than one segment). The track fitting procedure starts after the ambiguities are removed. The first step in the MOORE track fitting is a combination of the 3D segments into track candidates. The track candidates are required to be formed by at least two segments. For segments built in regions where chambers overlap and in the middle-outer endcap region, a straight line fit is performed. For the segments found in the rest of the chambers a curved fit with an impact parameter constraint is used. The track candidates are built segment by segment starting from those built in the outer stations. The track candidates are then fitted using the `GlobalChi2Fitter`. For the extrapolations performed in the tracking procedure, the detailed information provided by the muon `TrackingGeometry` is used.

Once the tracks have been reconstructed by either algorithm, they are extrapolated back to the beam pipe. The track parameters are then given at three points: the entrance of the spectrometer, the entrance of the calorimeters and the perigee. This extrapolation to the beam pipe accounts for the multiple scattering and energy loss corrections due to the material in the calorimeters. For this, Muonboy uses its own energy loss and multiple scattering parametrisation. To describe the material effects, MOORE makes use of the `Muid` algorithm. `Muid` uses its own parametrisation of the energy loss with a set of scattering planes inside the calorimeters. If the track is well isolated and the measured energy is larger than the most probable value of the parametrisation, `Muid` uses the energy measured in the calorimeters [67].

Figures 3.10 and 3.11 show the efficiency and expected fake rate for the standalone algorithms using $Z \rightarrow \mu^+ \mu^-$ and $t\bar{t}$ samples. There is a loss in efficiency where the detector coverage is poor ($|\eta| < 0.1$ and $1.2 < |\eta| < 1.7$). This degradation in the efficiency is explained by the reduced number of stations traversed by the track at such angles, therefore leaving fewer hits for the pattern recognition. Otherwise the efficiencies are close to 100% for both Muonboy and MOORE, although slightly higher for Muonboy. On the other hand, the number of fakes produced by the MOORE algorithm is lower than in the Muonboy case. In addition, the presence of the extra material of the endcap toroid is also a burden to the reconstruction algorithms [39]. Figure 3.12 shows the momentum resolution as a function of η and p_T for both algorithms. Notice that MOORE in general obtains better momentum resolution than Muonboy. A less intense magnetic field in the overlap between barrel and endcap

toroids (see Figure 2.18), also contributes to the efficiency and the momentum resolution degradation.

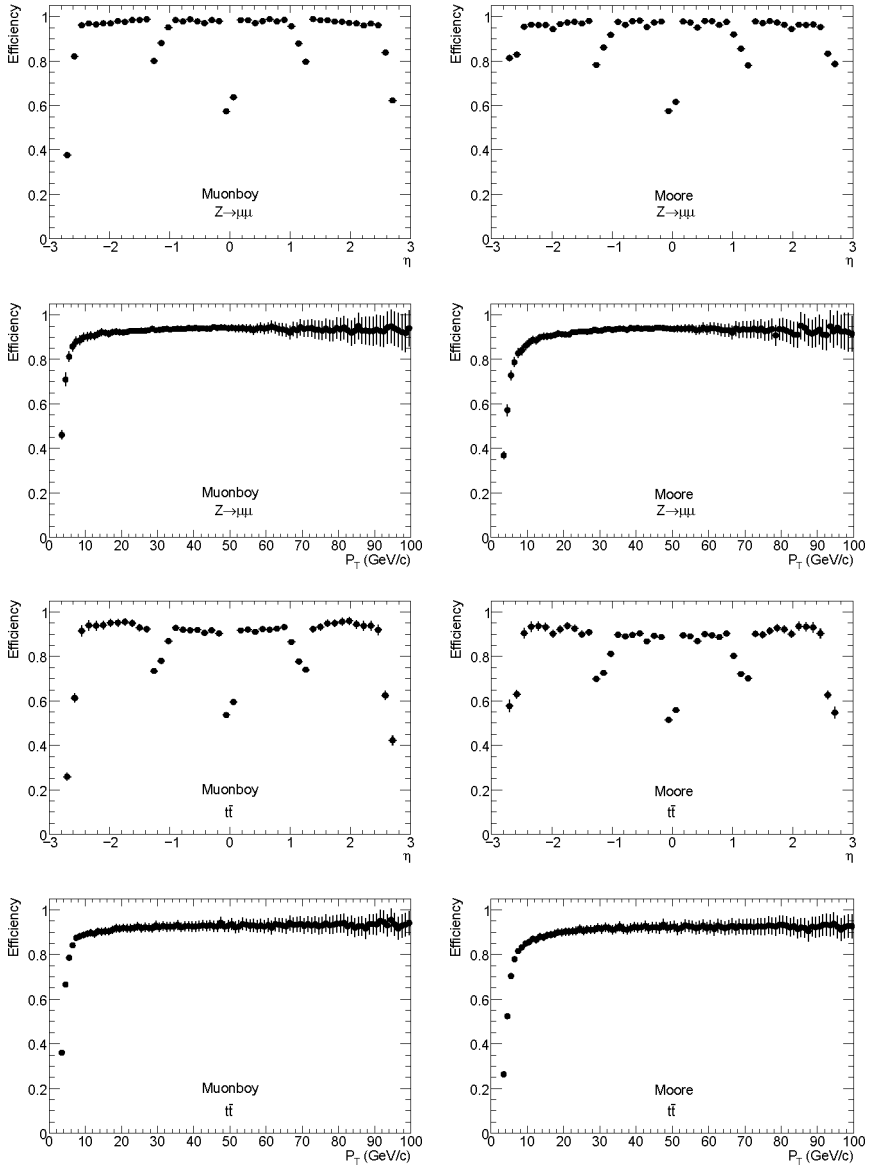


Figure 3.10: Standalone muon reconstruction efficiency as a function of η and p_T for muons in a $Z \rightarrow \mu\mu$ sample and for direct muons in a $t\bar{t}$ sample. These results were obtained with version 13.0.30 of the ATHENA reconstruction software. The errors shown are the square root of the sum of squares of weight for each bin.

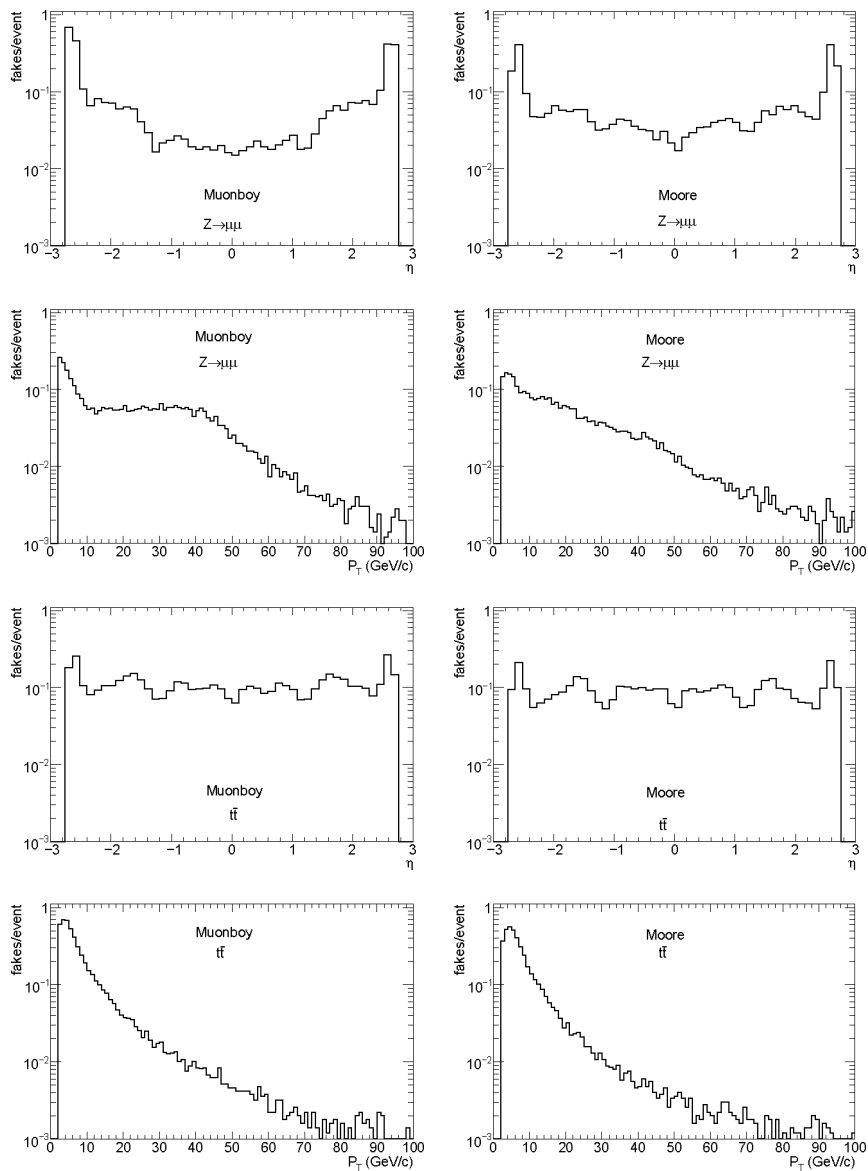


Figure 3.11: Standalone muon reconstruction fake rate as a function of η and p_T for muons in a $Z \rightarrow \mu\mu$ sample and for direct muons in a $t\bar{t}$ sample. These results were obtained with version 13.0.30 of the ATHENA reconstruction software.

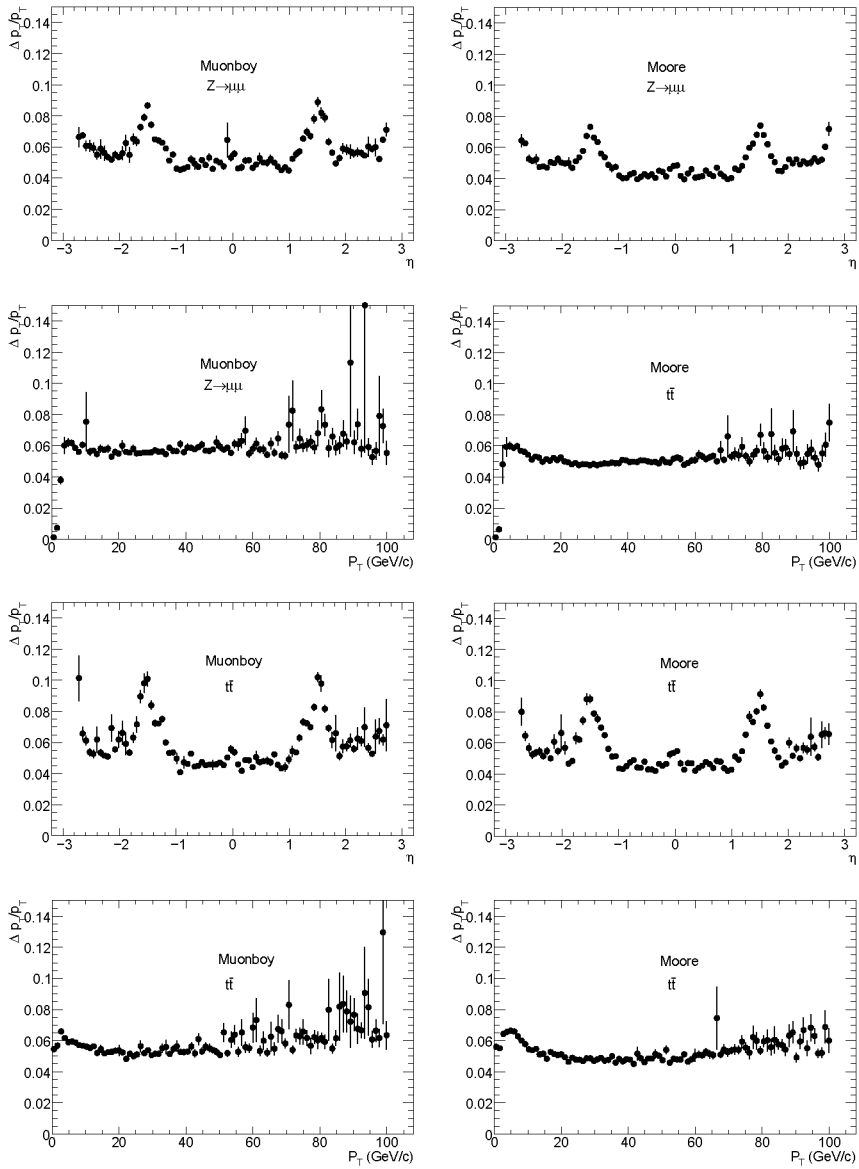


Figure 3.12: Standalone momentum resolution ($\Delta p_T/p_T$) as a function of η and p_T for muons in a $Z \rightarrow \mu\mu$ sample and for direct muons in a $t\bar{t}$ sample. These results were obtained with version 13.0.30 of the ATHENA reconstruction software.

3.4.3 Combined muons

The two families of algorithms perform combinations of the inner detector and the muon spectrometer tracks in a similar way. They both build a χ^2_{match} defined as the difference between the track parameter vectors (\mathbf{T}) weighed by their combined covariance matrix (\mathbf{C}):

$$\chi^2_{match} = (\mathbf{T}_{MS} - \mathbf{T}_{ID})(\mathbf{C}_{ID} + \mathbf{C}_{MS})^{-1}(\mathbf{T}_{MS} - \mathbf{T}_{ID})$$

Staco performs a statistical combination of both track parameter vectors to obtain the combined track vector. This statistical combination is defined as

$$\mathbf{T} = (\mathbf{C}_{ID}^{-1} + \mathbf{C}_{MS}^{-1})^{-1}(\mathbf{C}_{ID}^{-1}\mathbf{T}_{ID} + \mathbf{C}_{MS}^{-1}\mathbf{T}_{MS})$$

The track combination is tried first of all for pairs of tracks that show a good ϕ and η matching. The track combination is accepted only if the χ^2 of the global fit is below a maximum value. When ambiguities are found, a simple algorithm is applied: only the pair giving the best combined χ^2 is kept and the corresponding tracks are removed from the set of the tracks yet to be combined. This procedure is iterated until no more combinations are possible.

Muid fits the combined track using inner detector tracks as seeds, iteratively adding hits belonging to the spectrometer tracks. In a first step, the *MOORE* tracks are extrapolated back to the interaction region. The track is propagated through the magnetic field to obtain the track parameters and their associated covariance matrix at the perigee. The multiple scattering in the calorimeters is parametrised with a set of scattering planes. The interaction with the calorimeters is represented by five additional parameters, two scatterers (with η and ϕ information) and an energy loss parameter. Two scatterers are sufficient to give the deflected position and direction distributions and correlations. The energy loss measurement and errors are obtained either from the observed calorimeter energy deposition or from a parametrisation. This parametrisation is a function of η and the muon momentum.

In the next step, inner detector and muon spectrometer tracks are matched using a χ^2 with five degrees of freedom. The χ^2 is built from the differences in the five track parameters and their summed covariance. Fitting attempts are performed for all combinations with a χ^2 probability below a given value. When no matches are found that satisfy this criterion, a combined fit is attempted to obtain the best match within a certain distance around the muon spectrometer track. Tracks are then refitted using the measurements and scatterers from the inner detector, calorimeter, and muon spectrometer systems. The matches giving a satisfactory combined fit are identified as muons.

Figures 3.13 and 3.14 show the efficiency and fake rate of the combined muon reconstruction algorithms as a function of η and p_T , for muons in a $Z \rightarrow \mu^+\mu^-$ sample and direct muons in a $t\bar{t}$ sample. When the results are compared to the performance of the standalone algorithms, it can be noticed that both *Staco* and *Muid* show a significant drop in the fake rate, whilst maintaining the high efficiencies of the standalone algorithms. Again, *Staco* presents slightly higher efficiency than *Muid* with larger fake rate.

Figure 3.15 shows the muon momentum resolution as a function of both η and p_T for the samples considered. It can be seen that the resolution is significantly better after the combined refit than in the standalone case. Notice that *Muid* presents a slightly better momentum resolution than *Staco*.

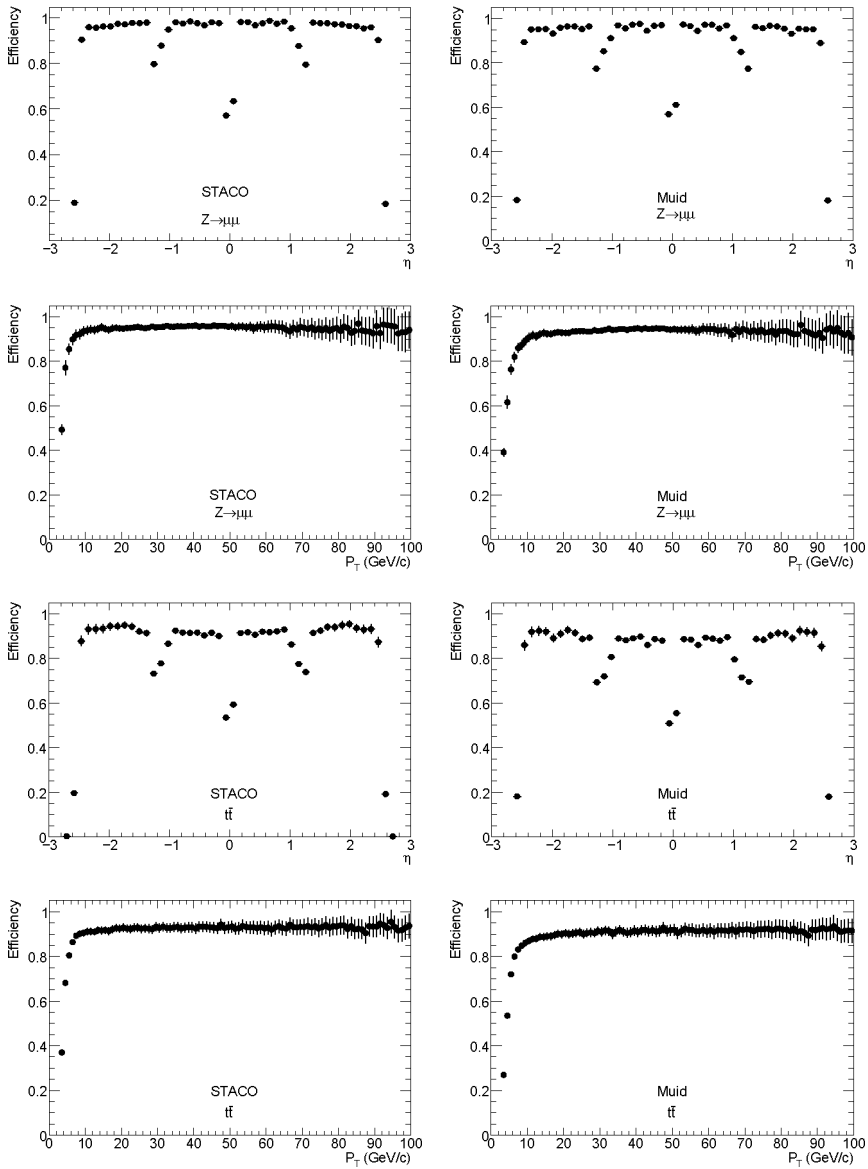


Figure 3.13: Combined muon reconstruction efficiency as a function of η and p_T for muons in a $Z \rightarrow \mu\mu$ sample and for direct muons in a $t\bar{t}$ sample. These results were obtained with version 13.0.30 of the ATHENA reconstruction software.

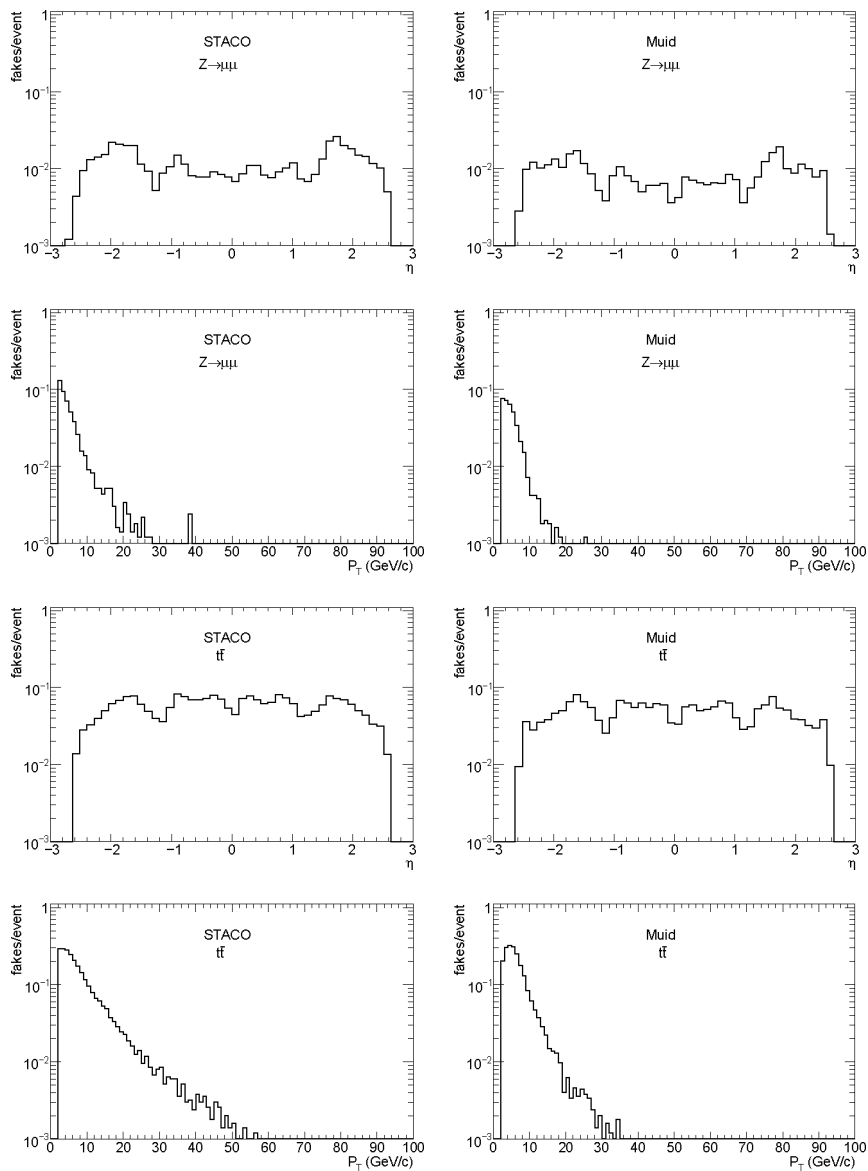


Figure 3.14: Combined muon reconstruction fake rate as a function of η and p_T for muons in a $Z \rightarrow \mu\mu$ sample and for direct muons in a $t\bar{t}$ sample. These results were obtained with version 13.0.30 of the ATHENA reconstruction software.

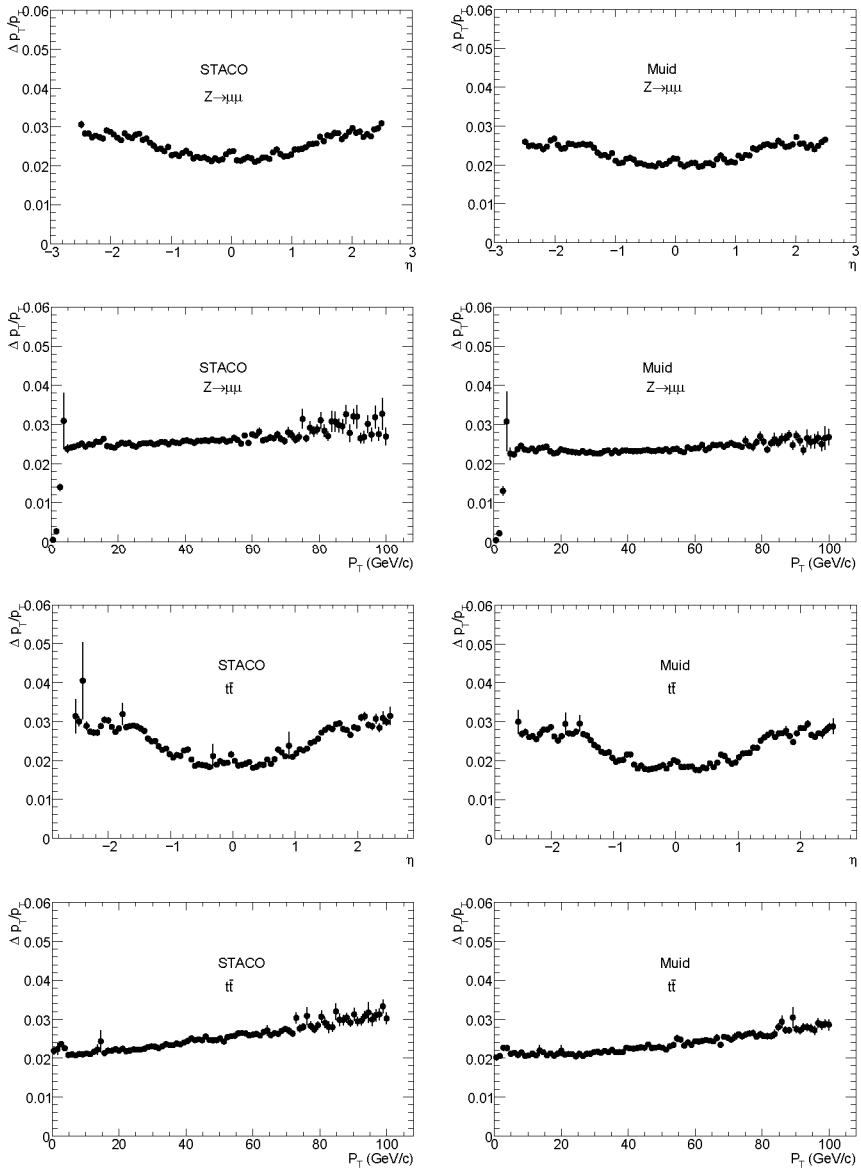


Figure 3.15: Combined momentum resolution ($\Delta p_T/p_T$) as a function of η and p_T for muons in a $Z \rightarrow \mu\mu$ sample and for direct muons in a $t\bar{t}$ sample. These results were obtained with version 13.0.30 of the ATHENA reconstruction software.

3.4.4 Muon Taggers

The spectrometer based tagging algorithms: MuTag [61] (from the *Staco* family), MuGir1 [68] and MuTagIMO (belonging to the *Muid* family), use the inner detector tracks as seeds to search for matching segments in the muon spectrometer. MuTag complements *Staco* regions where its efficiency is reduced. While MuGir1 and MuTagIMO can be used as standalone muon identification algorithms. The taggers can also be used to recover low p_T muons that only cause marginal activity in the spectrometer. Thus, the muon taggers increase the overall robustness of the muon identification software.

MuGir1 extrapolates the tracks to the first or middle stations before the matching. It utilises a neural network to define a discriminant. Additionally, MuGir1 can be configured to add more weight to tracks that have also been tagged by the calorimeter based identification algorithms. MuGir1's performance results can be found elsewhere [68].

MuTagIMO [69] is a recent addition to the muon identification algorithms in ATLAS. It extrapolates inner detector tracks to surfaces that correspond to the positions of the inner, middle and outer stations. MuTagIMO searches for nearby segments performing a loose matching on the η and ϕ of the track and segment parameters. The algorithm can refine the muon identification by assigning multiple segments to the track. It originally developed using cosmic ray muon data gathered in the ATLAS detector commissioning runs. The good results obtained, encouraged its introduction in the standard reconstruction chain.

MuTag complements the combination algorithms, using only those spectrometer segments that were not used during the track matching. MuTag extrapolates the tracks to the inner most muon stations, only extrapolating to the middle stations in the regions where there is a station overlap. The algorithm defines a tag procedure based on the value of a χ^2 , defined as the difference between the nearby segments and the extrapolated parameters. Since the next chapters will focus solely on the *Staco* family, only results for the MuTag algorithms are presented in this section.

Figure 3.16 shows the MuTag segment tagger complementary efficiency and fake rate, versus η and p_T , for muons in a $Z \rightarrow \mu^+ \mu^-$ sample and direct muons in a $t\bar{t}$ sample. Since MuTag is meant as a complement to *Staco*, it shows good performance in the case of low- p_T tracks and where the muon spectrometer presents limitations ($1.0 < |\eta| < 1.4$). Notice however that MuTag is restricted to $|\eta| < 2.0$ to reduced the addition of fake identifications. Even so, the fake rate that MuTag presents is much higher than for *Staco*, especially in busy events such the $t\bar{t}$ sample case.

Figure 3.17 shows the momentum resolution of the inner detector muon tracks for the samples. Since the tagger algorithms do not perform any track refitting, the distributions shown are the expected momentum resolutions for the muon taggers.

Figure 3.18 shows the performance when muons found by MuTag are combined with *Staco*'s. Notice that both algorithms complement each other and provide high precision measurements through η and p_T for the considered samples.

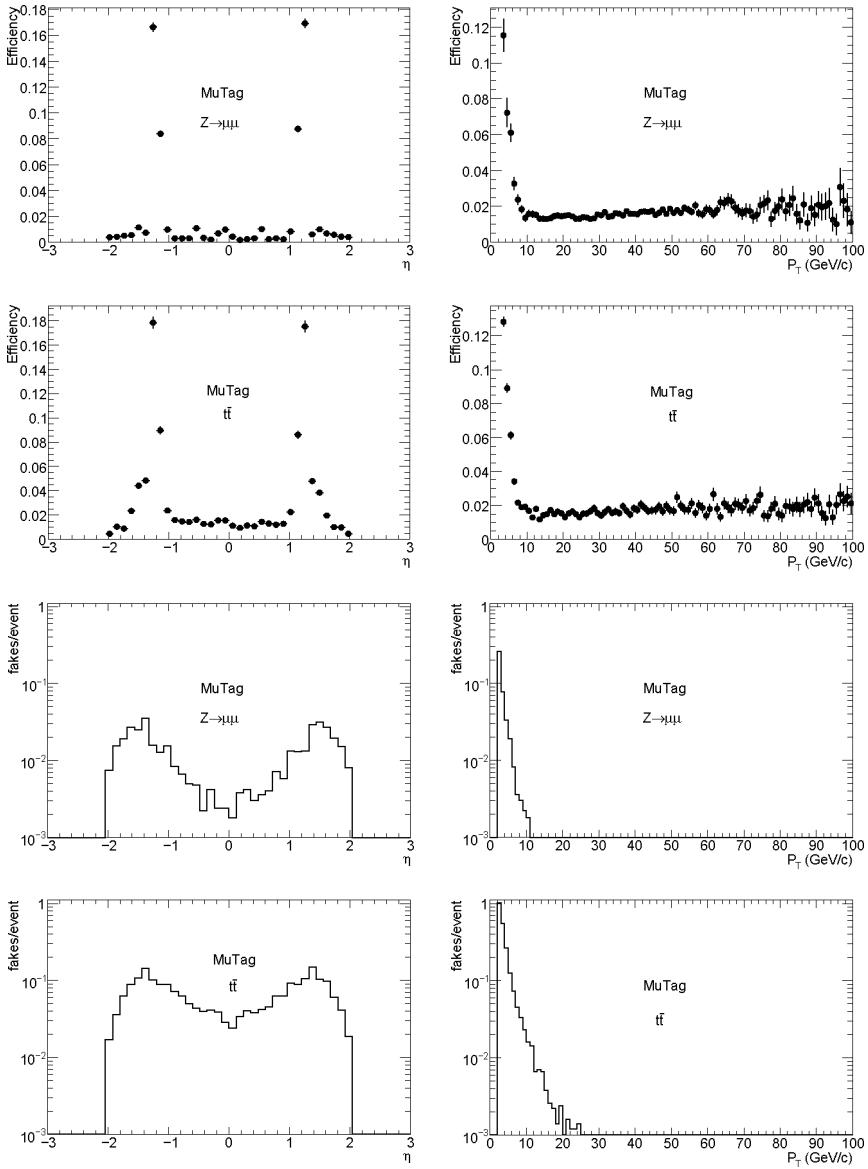


Figure 3.16: MuTag complementary efficiency and fake rate as a function of η (left) and p_T (right) for muons in a $Z \rightarrow \mu\mu$ sample and for direct muons in a $t\bar{t}$ sample. These results were obtained with version 13.0.30 of the ATHENA reconstruction software.

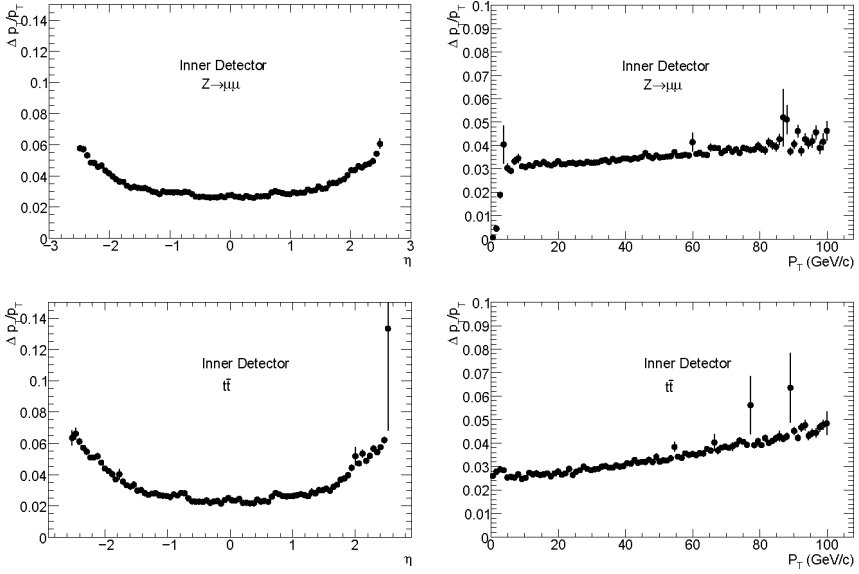


Figure 3.17: Inner detector muon reconstruction resolution ($\Delta p_T/p_T$) as a function of η (left) and p_T (right) for muons in a $Z \rightarrow \mu\mu$ sample (top) and for direct muons in a $t\bar{t}$ sample (bottom). these results were obtained with version 13.0.30 of the ATHENA reconstruction software.

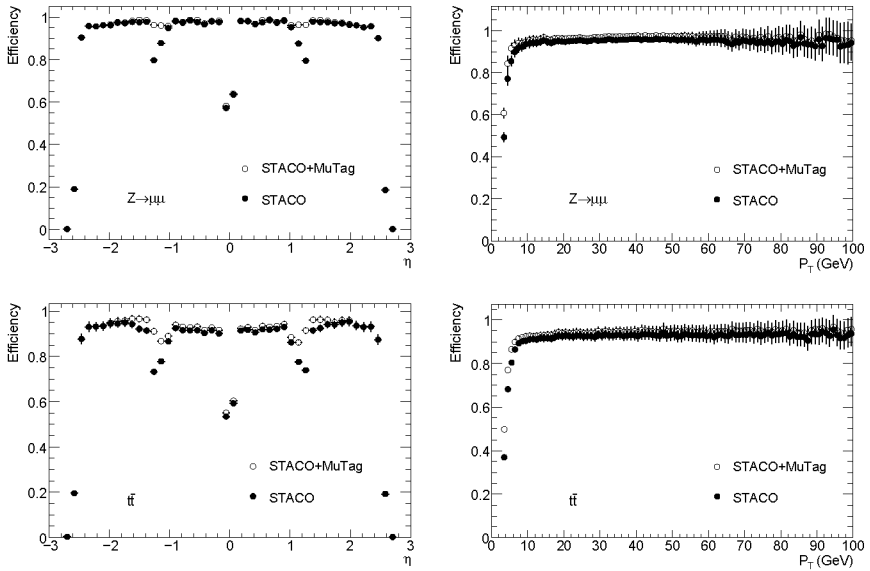


Figure 3.18: Combined reconstruction efficiency with and without the muon tagger *MuTag* as a function of η (left) and p_T (right) for muons in a $Z \rightarrow \mu\mu$ sample (top) and for direct muons in a $t\bar{t}$ sample (bottom). these results were obtained with version 13.0.30 of the ATHENA reconstruction software.

CHAPTER 4

MUON IDENTIFICATION IN THE CALORIMETERS

The distinctive energy deposition pattern in the calorimeters can be used to identify isolated muons amongst the tracks reconstructed in the inner detector tracker. Muon identification in the calorimeters can be used to recover low momentum ($p_T = 2 - 5 \text{ GeV}/c$) muons, which produce marginal activity in the muon spectrometer. In addition, it can recover the efficiency loss in the regions where the spectrometer acceptance is limited.

In this chapter, the `CaloTrkMuId` and `CaloTrkMuIdTools` software packages are introduced. These packages are implemented in the ATHENA framework. They provide tools such as: track candidate preselection, collection of the energy measured in the calorimeters and the calculation of the parametrised energy in each sampling. They also run the tools needed for building the muon objects used in physics analysis. `CaloTrkMuIdTools` includes two different algorithms for muon identification in the calorimeters. The first, `CaloMuonLikelihoodTool`, builds a likelihood discriminant using different energy ratios and is described elsewhere [70]. The second, `CaloMuonTag`, is discussed in this chapter. Finally, an efficiency and fake rate study is performed and compared with the muon reconstruction algorithms presented in the previous chapter. More details about this algorithm can be found in the Muon section of [14] under “Muon in Calorimeters: Energy Loss corrections and Muon Tagging”.

The tasks performed by the `CaloTrkMuId` algorithm can be divided in several steps:

- **Track preselection.** This is the selection of inner detector tracks that will be used as candidates. The algorithm performs a selection of candidates, keeping those tracks whose origin is found in the primary vertex and that pass certain isolation criteria.
- **Energy deposition in traversed cells.** The tracks are extrapolated through the electromagnetic and hadronic calorimeter samplings collecting the energy deposited in the traversed cells.
- **Tagging.** For each candidate, the algorithm looks for patterns consistent with a *minimum ionising particle*. For this, it applies threshold cuts above the calorimeter electronic noise and vetoes tracks with large energy deposits associated.

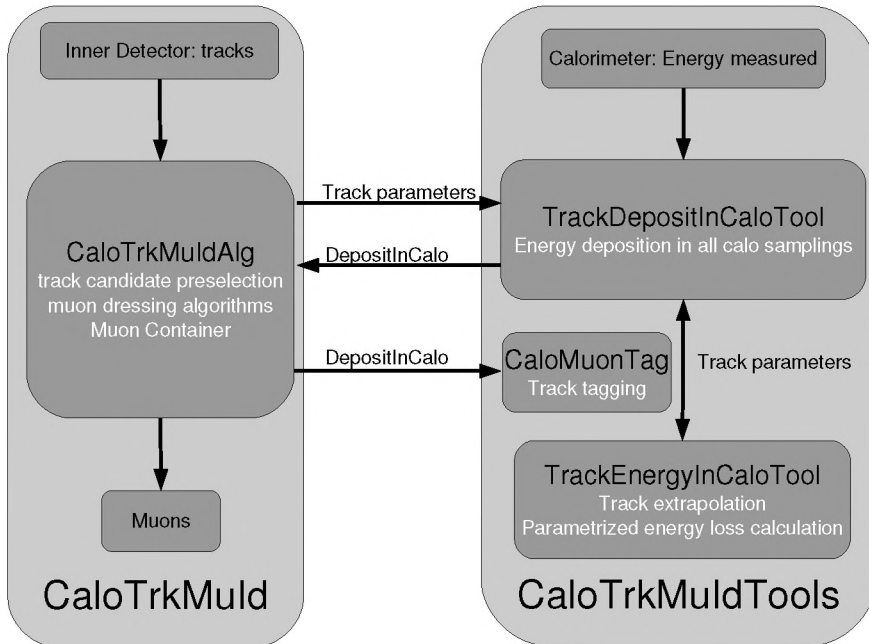


Figure 4.1: Data flow for the algorithms and tools in the `CaloTrkMuId` and `CaloTrkMuIdTools` packages.

4.1 Data flow

Figure 4.1 shows a schematic view of the data flow sequence for `CaloTrkMuId` and `CaloTrkMuIdTools`. The `CaloTrkMuId` package holds the ATHENA algorithm `CaloTrkMuIdAlg`. This algorithm is responsible for retrieving the inner detector `TrackParticle` data collection from the transient data store. It runs the different algorithms to build the muon objects, and writes the output back to the store. `CaloTrkMuIdAlg` performs a track candidate preselection and then runs the following `AlgTool` instances that are found in the `CaloTrkMuIdTools` package:

- `TrackDepositInCaloTool` collects the energy deposited in the cell crossed by the extrapolated tracks, as well as the parametrised energy loss in every calorimeter sampling. It uses `TrackEnergyInCaloTool` for the extrapolations and the parametrised energy loss calculation. The data is stored in a collection of `DepositInCalo` objects which hold, for every sampling traversed by the track, the sampling name, the energy measured and the parametrised energy loss.
- `TrackEnergyInCaloTool` is a wrap-up over the `Extrapolator AlgTool`, it also provides a method to calculate the parametrised energy loss using the extrapolated track parameters.
- `CaloMuonTag` is where the actual tagging is performed. It uses the information collected in the `DepositInCalo` objects to identify the muons amongst the preselected tracks. It first applies a energy veto per sampling cut, then applies noise threshold cuts on the last hadronic calorimeter sampling, only descending to previous samplings in the regions where there are gaps in the pseudorapidity (η) acceptance.

Finally, CaloTrkMuIdAlg runs other tools that are common to all muon algorithms, such as calorimeter energy isolation, and calorimeter cell association for different cone sizes.

4.2 Monte Carlo samples

For the studies presented in the next sections the following physics samples are used:

- $pp \rightarrow J/\psi \rightarrow \mu^+ \mu^-$. A direct production of a J/ψ decaying into two muons with the following cuts at generation level: one muon with $p_T > 6$ GeV/ c and the other with $p_T > 4$ GeV/ c . This sample was generated with PYTHIA.
- $H \rightarrow ZZ^* \rightarrow 4\ell$. A Higgs generated with an invariant mass of 130 GeV/ c^2 is forced to decay into two Z 's (one of them offshell) which further decay into leptons. This sample was also generated with PYTHIA.
- $t\bar{t}$. A sample of pair produced top quarks requiring at least one lepton (electron, muon or tau). This sample was generated using MC@NLO and Herwig.

These samples were chosen since they provide a good representation of the possible scenarios that a muon identification algorithm will face. Muons in J/ψ decays present typically low transverse momentum and relatively well isolated tracks. On the other hand, muons in $H \rightarrow ZZ^*$ decays tend to have higher transverse momentum and present a better isolation. Muons in $t\bar{t}$ decays present a wide range of transverse momentum tracks which can either be non-isolated (muons associated with b -quarks decays) or well isolated (muons in W decays). In addition, $t\bar{t}$ events tend to be very busy presenting a high multiplicity of tracks that can be source of potential mis-identifications.

At design luminosity, ATLAS will have a high multiplicity of interactions per beam crossing (pile-up), as well as a significant cavern background in the muon spectrometers. More information about the composition of the cavern background can be found in [71]. To account for these effects in the reconstruction algorithms performance, the physics samples were overlaid with pile-up and cavern background. The $H \rightarrow ZZ^* \rightarrow 4\ell$ and $t\bar{t}$ were overlaid with five times the nominal value of pile-up and cavern background expected at a luminosity of $10^{33} \text{ cm}^{-2} \text{ s}^{-1}$ (i.e safety factor 5). The $pp \rightarrow J/\psi \rightarrow \mu^+ \mu^-$ sample was overlaid with twice the nominal value (safety factor 2). Although there is a large uncertainty in the calculation of the pile-up and cavern background, the results could be considered as a rough estimate of the possible effects at high luminosity.

The figures shown in next section, were obtained running the ATHENA reconstruction on a combination of the three samples mentioned above in the following proportion: 10000 $H \rightarrow ZZ^* \rightarrow 4\ell$ events, 5000 $pp \rightarrow J/\psi \rightarrow \mu^+ \mu^-$ events and 5000 $t\bar{t}$ events. To obtain the results presented in this chapter, the event reconstruction was performed manually (except for the samples used in the last section), so the different reconstruction stages could be analysed in detail, however this means that the available amount of statistics is limited.

4.3 Muon tagging

Identification of muons in the calorimeter is a balance between efficiency and fake rate. Muons interact with matter mainly through electromagnetic processes, such as e^+e^- pair production and bremsstrahlung, thus producing narrow showers. The amount of energy deposited depends only on the path length of the muon through the different samplings,

which results in a characteristic energy deposition pattern. Other electromagnetic interactive particles, such as electrons and photons, lose most, if not all, of their energy in the electromagnetic calorimeter. Hadronic particles, such as pions, typically lose more energy in the first samplings of the hadronic calorimeter, the energy deposition being spread in broader solid angles. In ATLAS there are different calorimeter technologies [72] [73] with different levels of electronic noise. Algorithms for muon identification in the calorimeters need to set cuts above this noise to avoid mis-identifications. For a detailed study of the measurement of the muon energy in the ATLAS calorimeters refer to [70].

4.3.1 Track candidate preselection

The track multiplicity in the inner detector, especially in the presence of pile-up, is too high to consider all the tracks as candidates for tagging. In order to ensure a good performance in terms of CPU time, as well as to discard final state radiation tracks, is essential to perform a track preselection. This preselection applies cuts to different track parameters such as transverse momentum (p_T), impact parameter (d_0) and impact parameter significance (d_0/σ_{d_0}). After, cuts in the track isolation and calorimeter isolation are also applied.

Figure 4.2 shows the transversed momentum distributions for muon and non-muon tracks. Notice that most of the non-muons tracks have a very low p_T . The track preselection starts with a first cut of 2 GeV/ c in p_T . Muons which originate in secondary vertices tend to be non-isolated, since they are typically produced inside jets. The purpose of this algorithm is to tag isolated tracks, hence only candidates which originate in a primary vertex are considered. For this, the candidates are required to have at least 2 hits in the Pixel and 6 hits in the SCT subdetectors. Distributions for number of hits in the different subdetectors are shown in Figure 4.3 for muon and non-muon tracks. In addition, the cuts $d_0 < 1.2$ mm and $d_0/\sigma_{d_0} < 7$ are also applied. This selection also eliminates most of the final state radiation tracks which typically only present associated hits in TRT. Figure 4.4 shows distributions for these quantities.

Two possible isolation criteria can be applied to tracks. In the inner detector tracker, the sum of the p_T of the tracks inside a given cone around the candidate track defines the tracking isolation (p_T^{iso}). In the calorimeters, the transverse isolation energy (E_T^{iso}) is defined as the sum of the energy deposited in every sample inside a cone around the track. A very useful discriminating variable is the logarithm of the ratio of the sum of p_T of the tracks inside a cone with a solid angle of 0.45, divided by the candidate p_T ($\log_{10}(p_T^{\text{iso}}/p_T)$). A distribution of this variable for muon and non-muon tracks is shown in Figure 4.5. The value of the cut applied is $\log_{10}(p_T^{\text{iso}}/p_T) < 0.7$. The track isolation cut is applied before applying the more time consuming calorimeter isolation criteria.

In order to obtain the value for E_T^{iso} , the candidate is extrapolated through the calorimeters and the collection of calorimeter cells needs to be retrieved from the detector store. The energy in the cells found inside a cone with a solid angle of 0.45 is then added up. Three different regions in η corresponding to the barrel ($|\eta| < 1.5$), barrel-endcap transition region ($1.5 < |\eta| < 1.8$) and endcap ($|\eta| > 1.8$) are identified, where different cuts are applied: 15 GeV, 8 GeV, 12 GeV respectively. In addition, cuts on the discriminating variable $\log_{10}(E_T^{\text{iso}}/p_T)$ of, 0.4, 0.1, 0.2 in the same η regions are also applied. Figure 4.6 shows distributions for these variables.

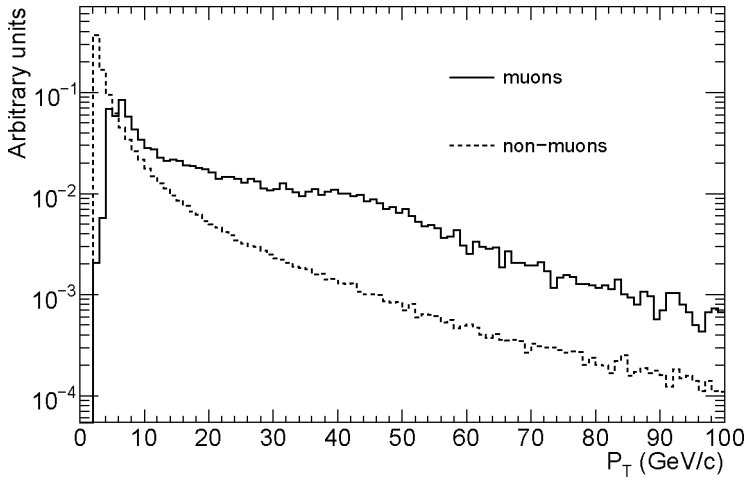


Figure 4.2: Distributions of transverse momentum p_T , for muon and non-muon tracks.

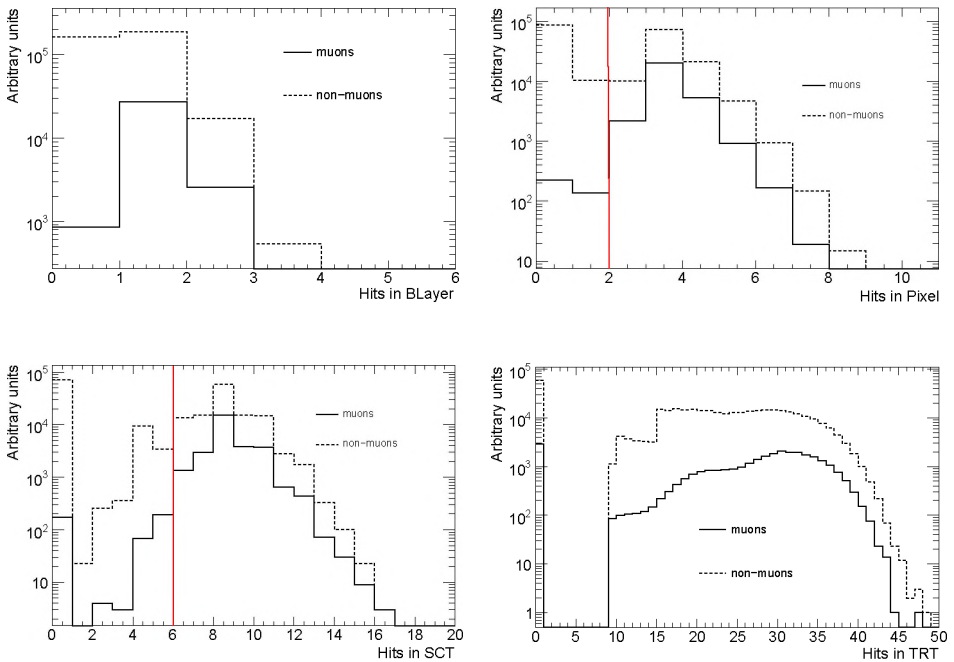


Figure 4.3: Comparison on the number of hits in each inner detector subdetector for muon and non-muon tracks. The vertical line represent the value of the cut applied during the track candidate preselection.

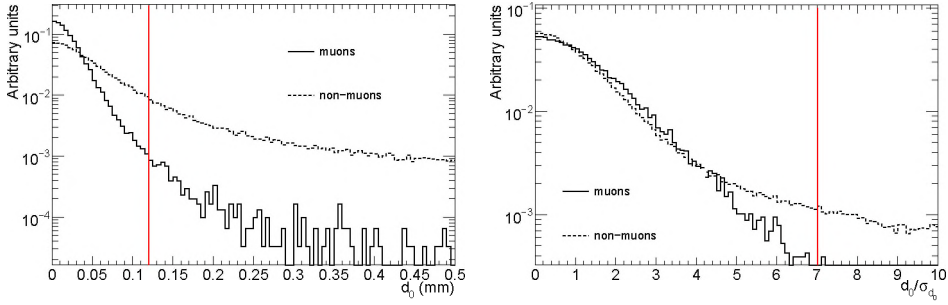


Figure 4.4: Distributions of d_0 and d_0/σ_{d_0} for muon and non-muon tracks. The vertical lines represent the value of the cuts applied during the track candidate preselection.

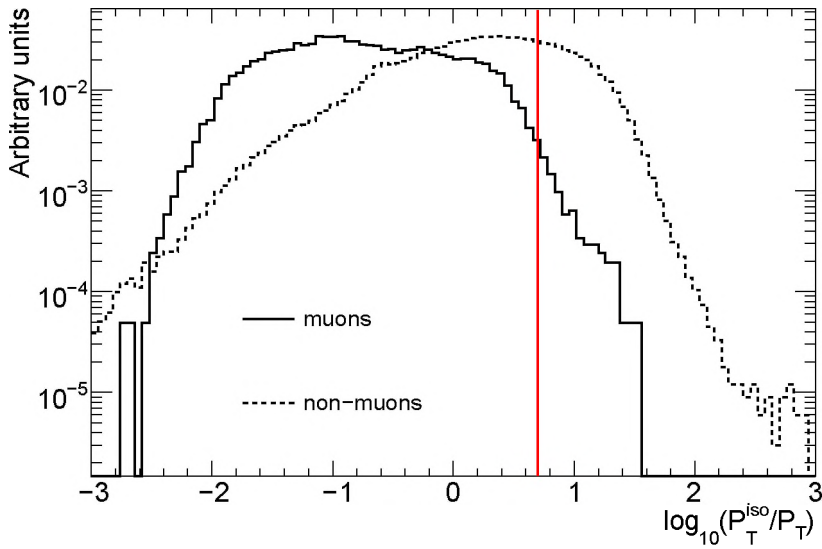


Figure 4.5: Distribution for the isolation in transverse momentum for muon and non-muon tracks. The vertical line represent the value of the cut applied during the track candidate preselection.

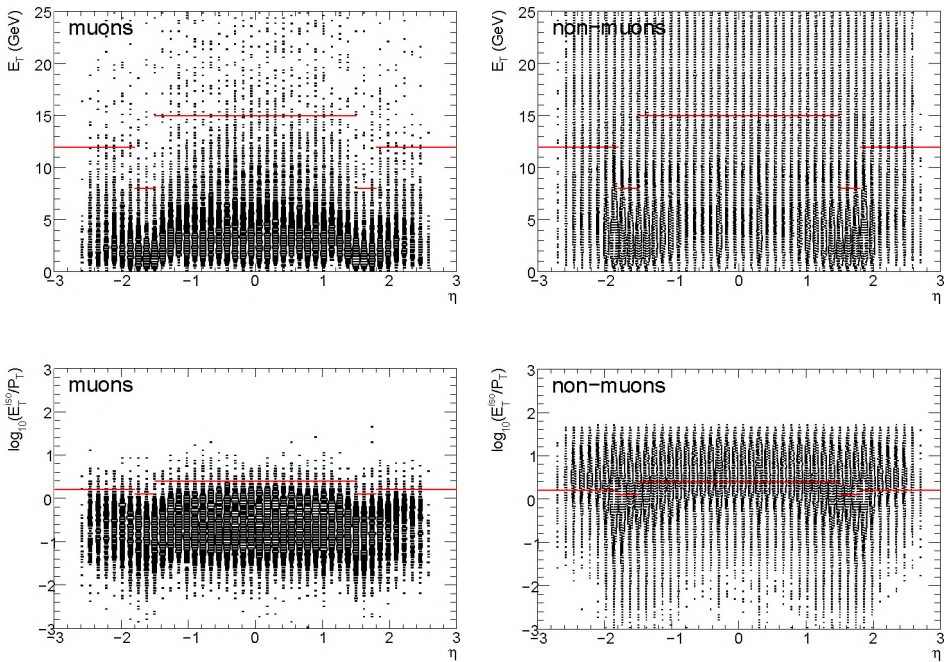


Figure 4.6: Distributions for E_T^{iso} and $\log_{10}(E_T^{\text{iso}}/p_T)$ as a function of η for muon and non-muon tracks. The horizontal lines represent the value of the cuts applied during the track candidate preselection.

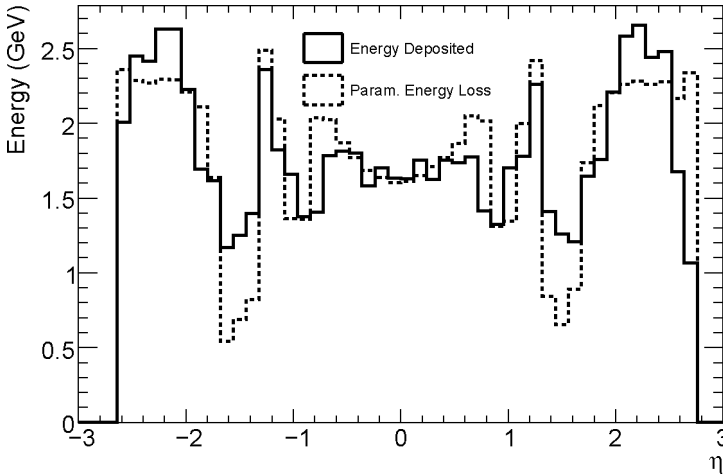


Figure 4.7: Energy deposited and energy loss parametrisation as obtained from *CaloTrkMuIdTools*.

4.3.2 Measured energy associated to the tracks

The preselected track candidates are extrapolated through the calorimeters, collecting the energy in the cell closest to the extrapolated track for each traversed sampling. The extrapolation is performed to surfaces created according to the information in *GeoModel*. These surfaces correspond to the ones used to build the calorimeter *TrackingGeometry*. Each tracking volume corresponds to a calorimeter sampling and contains all the material associated with it. This detailed description of the calorimeter geometry allows accurate extrapolations from sampling to sampling in the calorimeters. This also allows to calculate the parametrised energy loss used in the extrapolations. However, in the case of the EM calorimeters, the different length of the cells, depending on the value η considered [32], makes it very difficult to determine the exact amount of material that has to be associated to each sampling. Therefore, although *CaloTrkMuId* provides the values of the parametrised energy loss per sampling in the EM calorimeter, only the sum over all the traversed samplings can be considered accurate. Figure 4.7 shows the agreement between the energy deposited in the cell traversed by the track in each sampling and the parametrised energy loss as calculated during the extrapolation process. The static representation of the tracking geometry was used to obtain this result. There is a clear mismatch found in the barrel-endcap transition region ($1.2 < |\eta| < 1.8$). This is due to the fact that in the process of building the *TrackingGeometry*, the ITC modules (a part of the extended barrels of the *TileCal*) are not included. The *Extrapolator* does not account for that extra material and therefore the parametrised energy loss used in the extrapolations is lower than it should be. The “excess” of energy found in the endcaps is due to the high level of noise in the HEC. Notice, however that since the parametrised energy loss is not used as a selection criteria in the *CaloMuonTag* algorithm, its performance is not affected in any way by these limitations.

Figure 4.8 shows the energy deposited by the muon in the cell crossed and in the neighbouring cells. Notice that the probability for muons to share their deposited energy in more than one cell in the same sampling of the hadronic calorimeter is rather low. In order

to reduce the amount of electronic noise considered, this algorithm assumes that the muons deposit all their energy in only one cell per sampling.

Figures 4.10 and 4.11 show the energy found in the cell crossed by the muon and non-muon tracks, for the different samplings of the TileCal and HEC. The label Tile2 stands for the outermost sampling, Tile1 for the middle sampling and Tile0 for the inner most sampling. Analogously, HEC3 and HEC2 form the outermost wheel. HEC1 and HEC0 form the inner wheel. The figures show that both Tile2 and HEC3 present the best discriminating power for muon identification. However, as shown in Figure 4.9 there are gaps in η between the barrel and extended barrel modules (as well as between extended barrel and HEC modules). Therefore, in order to have a good coverage in pseudorapidity, the algorithm uses Tile1, Tile2, HEC2 and HEC1 samples for muon identification. Figure 4.12 shows the energy deposited in the cell crossed by the muon and non-muon tracks, in the Electromagnetic Calorimeter Barrel (EMB), and Endcap (EME). Notice that veto cuts in these samplings can be used for further discrimination.

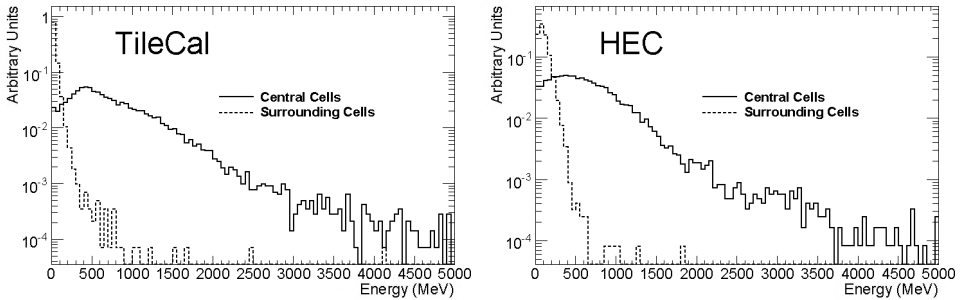


Figure 4.8: Energy found in the cell traversed by the extrapolated track (solid line) and the surrounding cells (dashed line) in the TileCal (left) and in the HEC (right). Distributions obtained for muons with $p_T = 100 \text{ GeV}/c$.

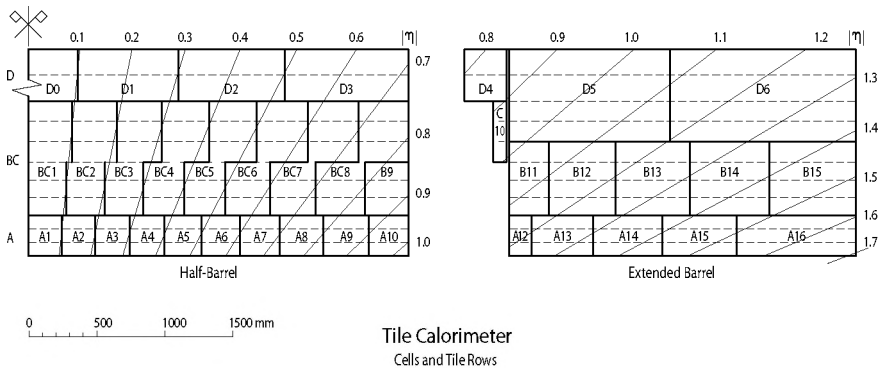


Figure 4.9: Cells and tile-rows in the barrel and extended barrel sections of the TileCal. Horizontal lines delineate the eleven rows of scintillating tiles. The heavy lines show the cell boundaries formed by grouping optical fibres from the tiles that are read out by separate photo-multipliers.

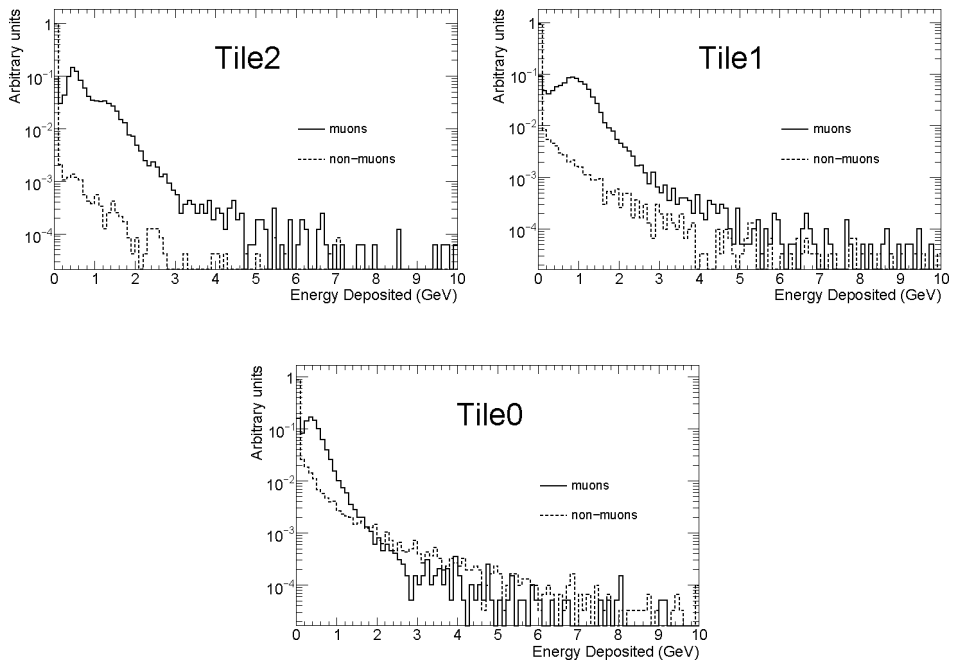


Figure 4.10: Energy deposited in the cell crossed by the track in the different samplings of the TileCal.

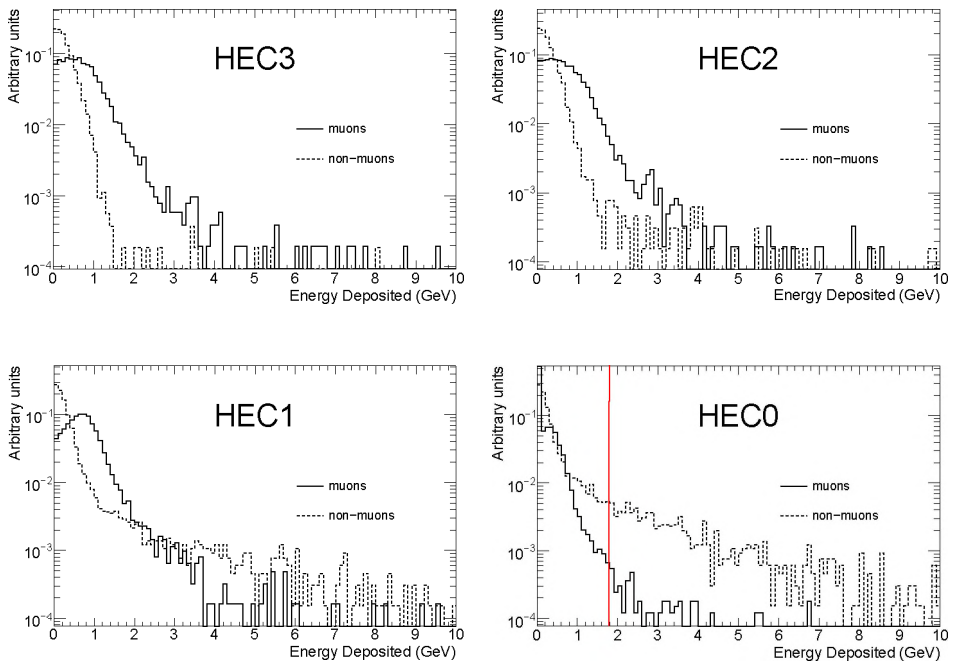


Figure 4.11: Energy deposited in the cell crossed by the track in the different samplings of the HEC. The vertical line in the HEC0 plot, represents the value for the veto cut applied.

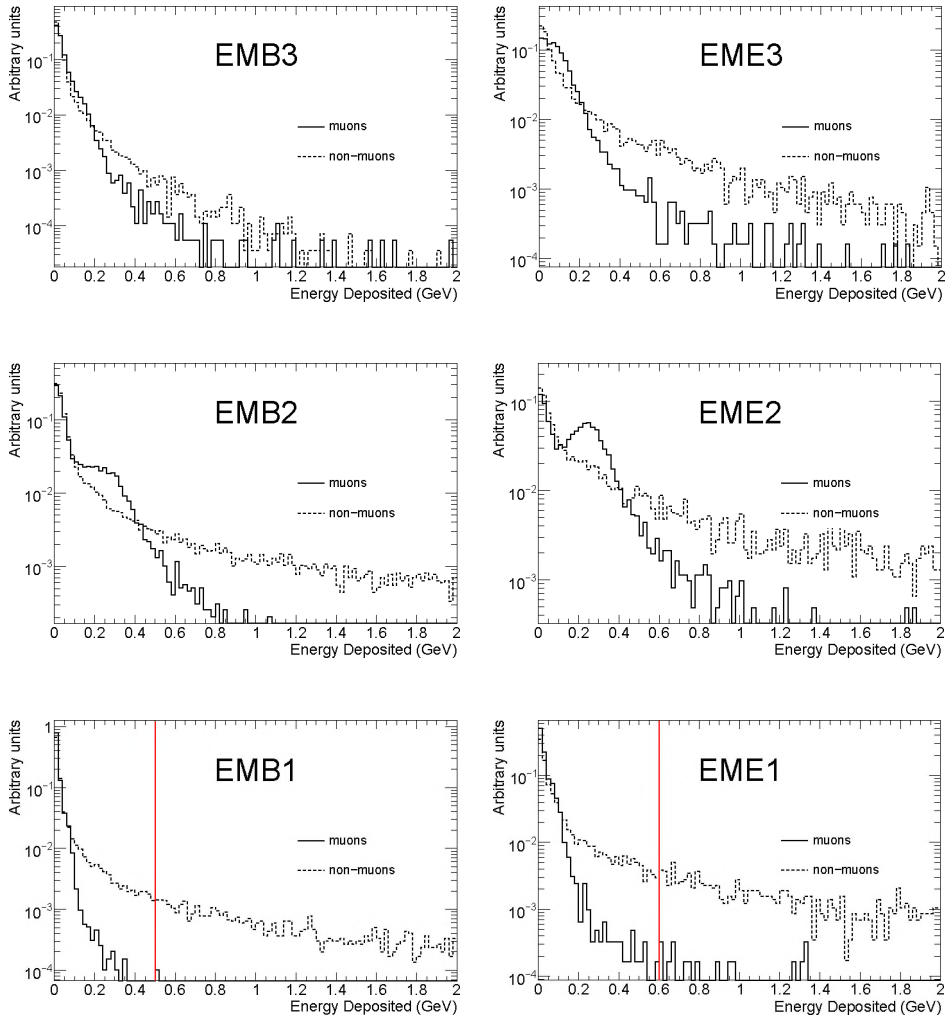


Figure 4.12: Energy deposited in the cell crossed by the track in the different samplings of the electromagnetic calorimeter. The vertical lines in the EMB1 and EME1 plots, represent the value for the veto cuts applied.

Energy veto per sampling (GeV)				
Sampling	0	1	2	3
Tile	10	10	10	-
HEC	1.8	10	8	10
EMB	-	0.5	10	2
EME	-	0.6	3	2

Table 4.1: Energy veto cuts for the different calorimeter samplings.

4.3.3 Track tagging

Once calorimeter cells along the muon trajectory have been identified, the algorithm determines the lower threshold energy cut (E_{th}), that will be used for tagging, as a function of η :

- $E_{\text{th}} = \frac{E_0^{\text{barrel}}}{\sin^2 \theta}$ for $|\eta| < 1.7$,
- $E_{\text{th}} = \frac{E_0^{\text{endcap}}}{(1 - \sin \theta)^2}$ for $|\eta| > 1.7$,

These two equations roughly follow the shape of the measured energy distributions, which increases with the path length of the muon in the cell. The values for E_0^{barrel} and E_0^{endcap} are chosen to be 50 MeV in both cases, to ensure a constant efficiency through η . The value of E_0^{endcap} can be raised in order to reduce the fakes in the HEC caused by the high electronic noise. In particular, for low p_T tracks ($p_T < 10$ GeV), which are the main source of fakes, a cut of 200 – 300 MeV can be applied. Figure 4.13 shows the energy deposited in the last calorimeter sampling and the noise threshold cuts applied for muons and non-muons tracks. Table 4.1 shows the values of the veto energies used in each sampling.

Energy depositions in the “last layer” of the calorimeters (samplings Tile2 and HEC3), give the most reliable muon signals. However, due to the existing gap between the TileCal barrel and extended barrel modules, and the transition region between the TileCal and the HEC, it is necessary to descend into the “last-1” (samplings Tile1 and HEC2) and “last-2” (Tile0 and HEC1) layers, in order to cover the entire η range. If the energy is above the threshold cut E_{th} , the track is tagged as a muon. Different tags are given depending on the “layer” in which the check is successful:

- Tag 1, the track was tagged using the deposits in either Tile2 or HEC3 (last layer).
- Tag 2, the track was tagged using the deposits in either Tile1 or HEC2 (last-1).
- Tag 3, the track was tagged using the deposits in either Tile0 or HEC1 (last-2).

Figures 4.13, 4.14 and 4.15 show the values of the energy deposited in the cell crossed by the track and the value of the cut applied in the three different layers. Notice that these cuts ensure a good tagging efficiency while reducing the chances of mis-tagging.

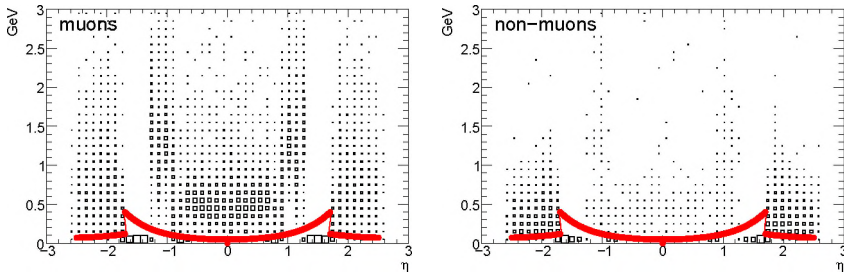


Figure 4.13: Energy deposited in the cell crossed by the track in the last calorimeter sampling and the noise threshold cut as a function of η . Notice the gaps in the pseudorapidity coverage on the “last” layer.

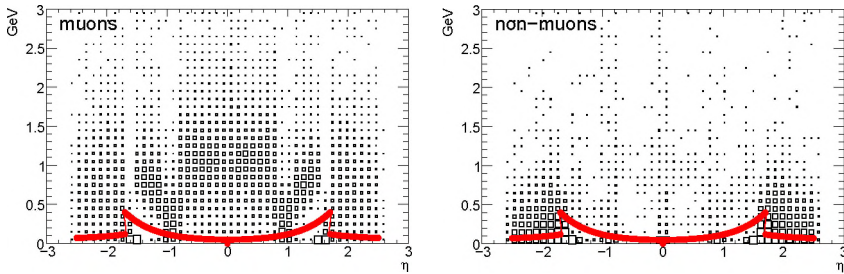


Figure 4.14: Energy deposited in the cell crossed by the track in the “last-1” calorimeter sampling and the noise threshold cut as a function of η . Notice the gaps in the pseudorapidity coverage on the “last-1” layer.

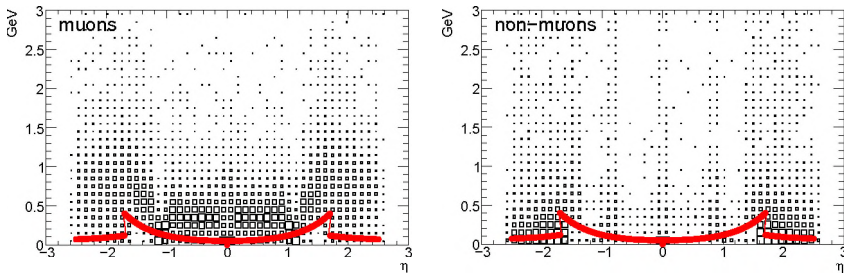


Figure 4.15: Energy deposited in the cell crossed by the track in the “last-2” calorimeter sampling and the noise threshold cut as a function of η .

	$J/\psi \rightarrow \mu^+ \mu^-$	$H \rightarrow 4\ell$	$t\bar{t}$
Efficiency	0.86	0.86	0.84
fakes/event	0.37	0.32	0.42

Table 4.2: Summary of the efficiencies and fakes per event for different physics processes.

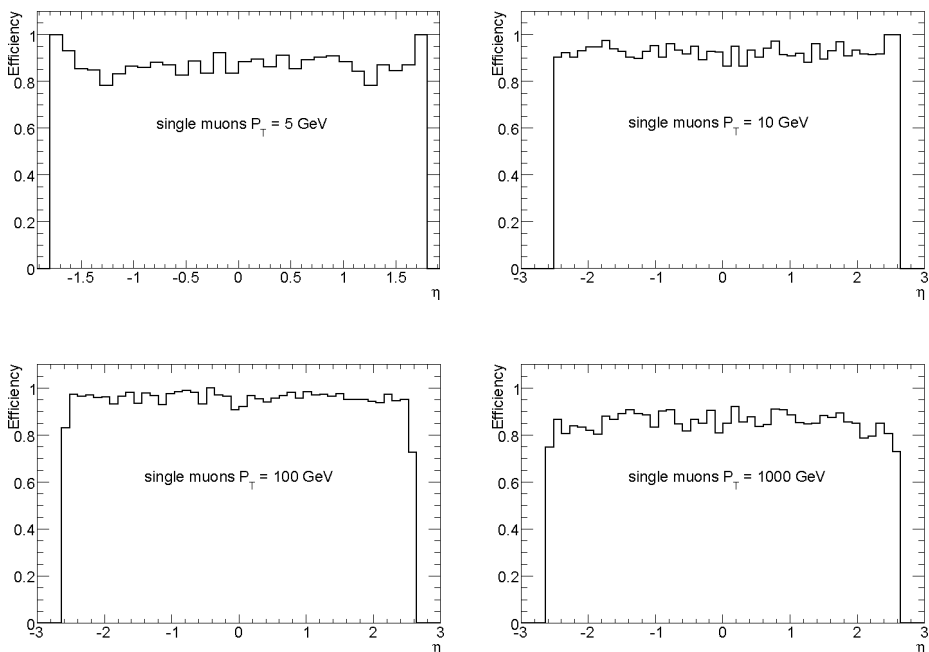


Figure 4.16: Efficiency as a function of η for single muon samples with fixed momentum.

4.4 Performance of CaloMuonTag

The performance of CaloMuonTag is studied first with fixed momentum single-muon samples. The momenta chosen for this validation are 5, 10, 100 and 1000 GeV/c. Figure 4.16 shows the efficiency obtained for these samples. The efficiency is defined as the muons identified by the algorithm that are matched to simulated muons divided by the total number of simulated muons in the sample with $p_T > 2$ GeV.

Figure 4.17 shows the performance of the calorimeter muon tagger algorithm on the selected samples described in Section 4.2. The distributions on the left show the efficiency as a function of η . The distributions on the right present the same efficiency plots showing in which “layer” the muons are tagged and which CaloMuonTag tag the tracks are given. In the case of the $t\bar{t}$ sample, the inhomogeneous structure in the efficiency figure is caused by the limited statistics available.

Figure 4.18 shows distributions of the number of fakes per event as a function of η . A fake is defined as a tagged track that was not matched to a simulated muon. The figures on the right show which calorimeter “layer” was used for tagging the mis-identified track.

Comparing the distributions on the right and left it can be noticed that the “peaks” in the fake rate match the regions where the acceptance of the last calorimeter sampling is limited. Notice that due to the higher electronic noise, Ca10MuonTag presents a higher fake rate in the HEC. The performance results for these samples are summarised in Table 4.2.

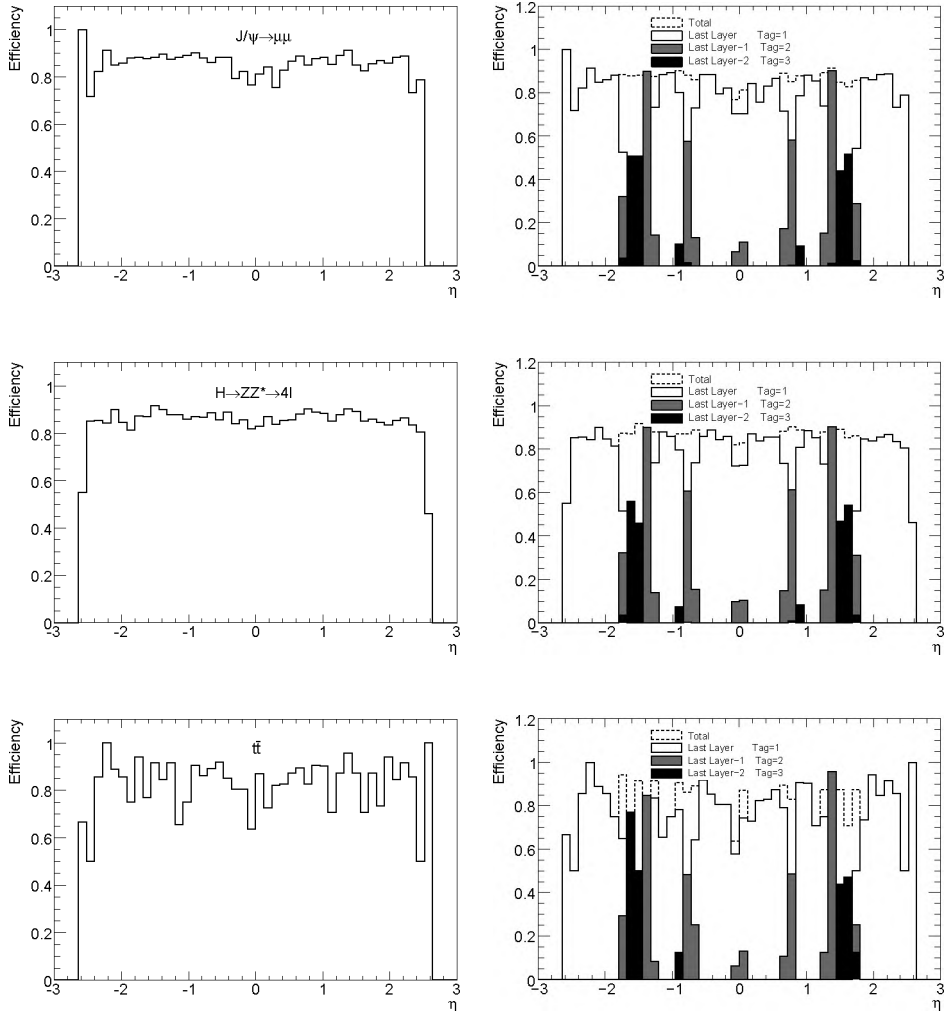


Figure 4.17: Efficiency versus η for different samples. Top: $pp \rightarrow J/\psi \rightarrow \mu^+ \mu^-$. Middle: $H(130) \rightarrow ZZ^* \rightarrow 4\ell$. Bottom: $t\bar{t}$. Figures on the right use a colour code to show in which calorimeter “layer” the track was tagged: white = “last”, grey = “last-1”, black = “last-2”. The dashed line represents the total sum over the three layers.

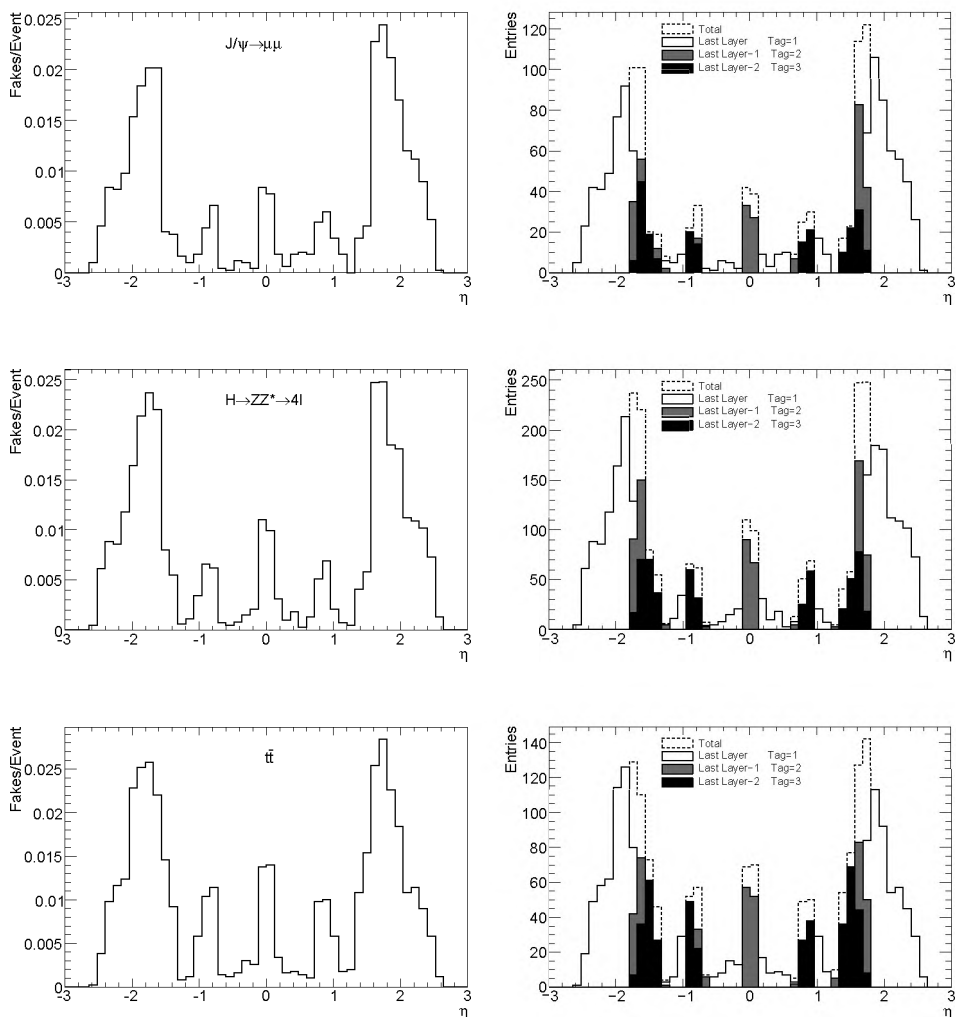


Figure 4.18: Fake rate versus η for different samples. Top: $pp \rightarrow J/\psi \rightarrow \mu^+\mu^-$. Middle: $H(130) \rightarrow ZZ^* \rightarrow 4l$. Bottom: $t\bar{t}$. Figures on the right show in which layer the misidentification occurred. The colour code shows in which calorimeter “layer” the track was tagged: white = “last”, grey=“last-1”, black=“last-2”. The dashed line represents the total sum over the three layers.

	$J/\psi \rightarrow \mu^+\mu^-$	$H \rightarrow 4\ell$	$t\bar{t}$
Comb. Rec.	3.42	5.20	12.08
Calo muon+GC	0.12	0.18	1.42
Total	3.54	5.38	13.50
Calo muon	10.37	3.62	21.17
Total	13.79	8.82	33.25

Table 4.3: Number of fakes in every 1000 events for the combined muon reconstruction and the increase when adding an extra muon found by CaloMuonTag, with and without the geometrical cut (GC) $|\eta| < 0.1$. A cut on $|\eta| < 2.5$ was used on the three samples. Additionally, in the J/ψ sample a cut on $p_T > 4$ GeV/c was applied while in the other two samples the cut was raised to $p_T > 7$ GeV/c.

4.5 Improvements to the muon reconstruction

This section studies the expected enhancements in the combined muon reconstruction chain due to the use of CaloMuonTag. For this, the Staco family is used. The samples used in this part of the study were reconstructed using ATHENA version 13.0.30 and produced centrally. In order to make the comparison between algorithms more accurate this time the samples were not overlaid with pileup or cavern background.

Before adding the muons identified in the calorimeter to the standard muon container, an overlap removal with the reconstructed electrons is performed. This is done in order to remove electrons that might have been wrongly identified as muons by CaloMuonTag. Additionally, only one muon identified in the calorimeters is added to the standard container, if it already contains either one or three muons. Thus, the additions of calorimeter muons will complete sets of two muons or four muons.

The muons in the $J/\psi \rightarrow \mu^+\mu^-$ sample have a lower p_T and are slightly less isolated than the muons originating in Z and W decays. Tighter cuts can be applied in high- p_T analyses. Hence, the following additional cuts are applied to the CaloMuonTag muons found in the $H \rightarrow 4\ell$ and $t\bar{t}$ samples:

- $p_T > 7$ GeV/c.
- $\log_{10}(E_T^{\text{iso}}/p_T) < -0.05$.

Table 4.3, shows the expected increase in fake rate in the muon container when following this strategy. Since most of the efficiency recovered by the calorimeter muons is found in the region around $|\eta| < 0.1$, a geometrical cut can be applied to the calorimeter muons.

Figure 4.19 shows the increase in efficiency when the calorimeter muons are added to Staco and to Staco+Mutag. Notice that in the case of the J/ψ sample, there is a 6%

increase in efficiency. The reason for this is that many of the low momentum muons in this sample cause marginal or no activity in the spectrometer, but they can still be identified by CaloMuonTag. In the case of the $H \rightarrow 4\ell$ sample, the drop in efficiency around $|\eta| < 0.1$ is recovered and the overall gain is of about 3%. In the case of the $t\bar{t}$ sample, many of the muons are not well isolated, which results in a reduction of the expected contribution of CaloMuonTag.

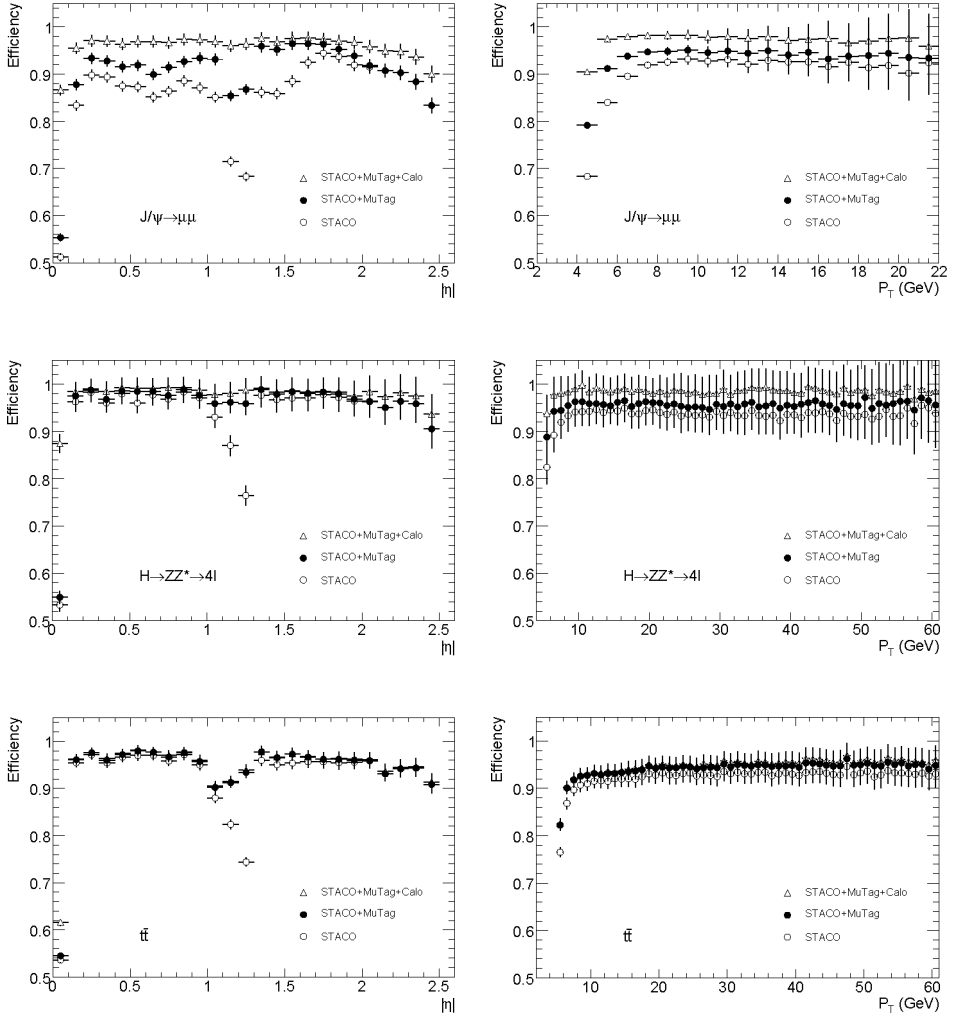


Figure 4.19: Reconstruction efficiency as a function of η (left) and p_T (right) for the algorithms: STACO, STACO+MuTag and when one extra CaloMuonTag muons is added to the samples: $J/\psi \rightarrow \mu^+\mu^-$ sample (top), $H \rightarrow 4\ell$ (middle) and $t\bar{t}$ (bottom). The errors shown are the square root of the sum of squares of weight for each bin.

4.6 Conclusions

Muon identification in the ATLAS calorimeters is a challenging task. The fine granularity of the TileCal and its low electronic noise makes it very suitable for muon identification. The identification is cleanest in the last sampling due to the screening effect of the rest of the samplings. In the HEC calorimeter, where the noise level is higher, muon identification is difficult. However, with a careful selection of the applied cuts, it is still possible to identify muons with good efficiency and reasonable fake rates even in the presence of the pileup expected at high luminosity. In the transition regions of the TileCal barrel-extended barrel and TileCal-HEC (barrel-endcap transition), the muon identification becomes even more challenging. Since less material is traversed in this region, the aforementioned screening effect is also reduced.

This chapter has shown that the identification of isolated muons in the calorimeters is not only possible, but it can be achieved with a high efficiency and reasonable fake rate. When in combination with other muon reconstruction and identification algorithms, it can help to recover muons that escape through gaps in regions where the muon spectrometer coverage is limited, or low momentum muons that do not cause enough activity. Eventually, one or more sectors of the muon spectrometer might present a reduced efficiency. In this case, muon identification in the calorimeters might be the only way of keeping good muon reconstruction performance inside the inner detector coverage. Hence, calorimeter identification makes the muon reconstruction software more robust.

To properly calibrate the `CaloMuonTag` algorithm access to high quality data will be needed. If for some reason any of the calorimeter modules is noisier than anticipated during simulation, `CaloMuonTag` might systematically tag tracks pointing to noisy cells as muons. Calibration studies can be performed by selecting samples with well isolated muons reconstructed by one of the combined algorithms (i.e. having an associated inner detector track). These isolated tracks can be used to determine the best set of cuts for `CaloMuonTag`.

When calorimeter muon identification is used in the context of a physics analysis, it is necessary to consider very carefully the associated fake rate. Detailed Monte Carlo studies are necessary to ensure that the introduction of fake muons will not bias the analysis. An example of such studies is presented in the next chapter.

CHAPTER 5

THE $H \rightarrow ZZ^{(*)} \rightarrow 4\ell$ ANALYSIS

The discovery of the Standard Model Higgs boson is the one of the most important goals of the LHC. The Higgs boson mass is a free parameter in the Standard Model, however there is strong evidence suggesting a low mass Higgs. Precision electroweak data [74] sets the Higgs mass in the range $114.4 - 144 \text{ GeV}/c^2$ at a 95% confidence level. In ATLAS, the channel $H \rightarrow ZZ^{(*)} \rightarrow 4\ell$, where the Higgs boson decays to two Z bosons (one of them off-shell), which decay further to either electrons or muons, presents the cleanest signature to measure the Higgs boson mass. The analysis presented in this chapter follows the guidelines found in [75]. In addition, it studies the improvements in the analysis when complementing the muon combined reconstruction with muons identified in the calorimeters by `CaloMuonTag`. As it will be shown, using calorimeter identified muons increases the signal selection efficiency while marginally increasing the reducible background, hence increasing the overall signal over background significance.

The good momentum resolution that can be achieved in the reconstruction of muons and electrons in ATLAS, leads to a narrow 4-lepton invariant mass peak. This can be used to obtain a good signal over background significance after the application of selection cuts. The main backgrounds for this channel are:

- Irreducible: $pp \rightarrow ZZ^{(*)} \rightarrow 4\ell$.
- Reducible: $pp \rightarrow Zb\bar{b} \rightarrow 4\ell$ and $pp \rightarrow t\bar{t} \rightarrow 4\ell$.

Other potential backgrounds are the $Zb\bar{b}$ and WZ with 3ℓ in the final state and Z +jets processes. Tight lepton isolation cuts can be used to reduce the $Zb\bar{b}$ and $t\bar{t}$ backgrounds to well below the $ZZ^{(*)}$ background.

5.1 Monte Carlo samples and trigger studies

5.1.1 Signal Monte Carlo samples

The Higgs signal samples were generated with PYTHIA version 6.3. A study of the signal cross sections at leading order (LO) and next-to-leading order (NLO) can be found in [15]. A total number of 40K events ($K = 1000$) were generated with a Higgs boson mass of $130 \text{ GeV}/c^2$. A filter acceptance (FA) requiring 4 leptons with $p_T > 5 \text{ GeV}/c$ within $|\eta| < 2.7$ was applied. A Higgs boson mass of $130 \text{ GeV}/c^2$ was chosen since it is favoured by the experimental constraints discussed in Section 1.1.7. Additionally, with this mass the channel presents good sensitivity.

FA	0.633
σ_{LO}	3.76 fb
σ_{NLO}	6.25 fb

Table 5.1: Four-lepton filter acceptance, LO and NLO cross sections for the signal with a Higgs boson mass of $130 \text{ GeV}/c^2$.

Process	Generator	FA	$\sigma(fb)$	Corrections	Events (K)
$q\bar{q} \rightarrow ZZ^{(*)} \rightarrow 4\ell$	PYTHIA 6.3	[4 ℓ] 0.219	158.8	+47.64	65
$gg \rightarrow Zb\bar{b} \rightarrow 2\ell b\bar{b}$	AcerMC-PYTHIA 6.3	[4 ℓ] 0.00942	52000	+8500	420
$gg \rightarrow Zb\bar{b} \rightarrow 2\ell b\bar{b}$	AcerMC-PYTHIA 6.3	[3 ℓ] 0.147	52000	+8500	200
$gg, q\bar{q} \rightarrow t\bar{t}$	MC@NLO-Jimmy	[4 ℓ] 0.00728	833000		380
$q\bar{q} \rightarrow WZ$	HERWIG-Jimmy	[3 ℓ] 0.0143	26500		70
$q\bar{q} \rightarrow Z \text{ inclusive}$	PYTHIA 6.3	[1 ℓ] 0.89	$1.6 \cdot 10^6$		470

Table 5.2: Monte Carlo background samples with the corresponding generators used, four-lepton filter acceptance, leading order cross section, corrections applied and number of events in thousands (K) for each sample. In $ZZ^{(*)}$, ℓ represents an e , a μ , or a τ ; for the remaining samples $\ell = e, \mu$.

Table 5.1 shows the filter acceptance, the LO and NLO cross sections for the signal sample used in this analysis. The cross sections are the sum of the contributions from the weak boson fusion (WBF) together with the gluon-gluon fusion process.

5.1.2 Background Monte Carlo samples

The background samples were produced using different Monte Carlo programs:

- The QCD $ZZ^{(*)}$ sample was generated with PYTHIA version 6.3.
- The $Zb\bar{b}$ background was generated using AcerMC [76] version 3.1. The parton distribution functions (PDF) set used was CTEQ6L with QCD scales $\mu_R = \mu_F = M_Z$. It was interfaced to PYTHIA 6.3 for showering and hadronisation.
- The $t\bar{t}$ sample was generated with MC@NLO [64] interfaced with HERWIG [65] and Jimmy [77].

Table 5.2 summarises the cross sections, filter acceptance, Monte Carlo generator used and number of events for the different backgrounds considered in the analysis. The cross sections were calculated at LO, except for the $t\bar{t}$ sample where the Monte Carlo generator already accounts for the NLO contributions. Notice that the cross sections in this table do not include the four lepton filter selection acceptance. The column ‘‘Corrections’’ summarises the corrections applied since some subprocesses were missing during the MC generation. For example, there was a missing quark box diagram in PYTHIA 6.3, so an additional 30 % has to be added to the $ZZ^{(*)}$ cross section. Additionally, the diagrams of the type $q\bar{q} \rightarrow Zb\bar{b}$ were missing in AcerMC 3.1, so a correction of 8500 fb is applied to account for this process. The last column of the table shows the number of events in each sample.

To evaluate the contribution of the NLO diagrams to the total cross section, the program MCFM [78] was used. The calculation was made using the CTEQ6M PDF set. The QCD

M_{ZZ^*} (GeV)	K-factor
(115, 125)	1.15
(125, 135)	1.21
(145, 155)	1.25
(155, 165)	1.34
(175, 185)	1.31
(195, 205)	1.32
(295, 305)	1.40

Table 5.3: K-factors for the $ZZ^{(*)}$ background.

coupling constant was calculated at the Z boson mass M_Z and the full Z/γ^* interference was included. When the final states had two or more jets inside a cone $\Delta R(jj) < 0.7$, the jets were merged into a single jet.

The $ZZ^{(*)}$ background

In the case of the $ZZ^{(*)}$ background, since the s -channel mechanism is very much suppressed in Z -pair productions, only the $q\bar{q} \rightarrow ZZ^{(*)}$ t -channel was considered. Although the Z/γ^* channel was also allowed, its contribution is heavily suppressed by the lepton filter. During the generation process both Z bosons were forced to decay into lepton pairs of electrons, muons or taus. The final four-lepton filter acceptance was 21.9%, substantially lower than in the signal case. Additionally, a lower cut $M_{Z^{(*)}} > 12 \text{ GeV}/c^2$ was applied to the off-shell Z boson mass.

For the calculation of the NLO cross section for the $ZZ^{(*)}$ process, the same kinematics selection on the Z boson masses used in PYTHIA were applied in MCFM. The calculated cross section is:

$$\sigma_{NLO} = 22.058_{-0.2}^{+0.1} \pm 0.714(PDF) \pm 0.037 \text{ pb.}$$

The K-factors (K_f) compare the cross section calculated at LO and NLO (σ_{NLO}/σ_{LO}). In this case they were found to depend on the $ZZ^{(*)}$ mass as shown in Table 5.3. The effective cross section used in the analysis is:

$$\begin{aligned} \sigma_{eff} &= \sigma_{LO} \cdot [BR(Z \rightarrow \ell\ell)]^2 \cdot FA \cdot (K_f + 0.3) \\ &= 34.82 \cdot (K_f + 0.3) = 52.58 \text{ fb,} \end{aligned}$$

where $\sigma_{LO} \cdot [BR(Z \rightarrow \ell\ell)]^2$ is the LO cross section from PYTHIA: $158.8 \pm 0.05 \text{ fb}$, which includes the $Z \rightarrow \ell$ branching ratio. The factor 0.3 represents the 30% correction applied to account for the missing quark box in PYTHIA.

The $Zb\bar{b}$ background

To generate the $(Z/\gamma^*)b\bar{b}$ sample additional selection cuts were used. A cut on the resonance mass at $M_{Z^{(*)}} > 30 \text{ GeV}/c^2$ was applied. Also, the transverse momentum of the b quark was chosen to be $p_T > 10 \text{ GeV}/c$. The quarks were forced to decay into leptons inside $|\eta| < 2.5$. The LO AcerMC cross sections for the gluon and quark process were:

$$\sigma_{gg \rightarrow (Z/\gamma^*)b\bar{b}} \times BR(Z \rightarrow \ell\ell) = 52.03 \pm 0.1 \text{ pb}$$

$$\sigma_{q\bar{q} \rightarrow (Z/\gamma^*)b\bar{b}} \times BR(Z \rightarrow \ell\ell) = 8.64 \pm 0.2 \text{ pb}$$

which include the $Z \rightarrow e^+e^-$ and $Z \rightarrow \mu^+\mu^-$ branching ratios.

The effective NLO cross section used for the $pp \rightarrow Zb\bar{b}$ process is therefore:

$$\sigma_{Zb\bar{b}} = (52.03 + 8.64) \times 1.424 = 86.39 \text{ pb.}$$

where 1.424 is the K_f calculated using MCFM. Taking into account the four-lepton filter acceptance in Table 5.2, the final cross section used in this analysis is:

$$\sigma_{eff} = \sigma_{LO} \cdot BR(Z \rightarrow e^+e^-, \mu^+\mu^-) \cdot FA \cdot K_f = 812.10 \text{ fb}$$

The WZ and $Zb\bar{b}$ backgrounds with 3ℓ in the final state

Other sources of potential background are the $Zb\bar{b}$ and the WZ with three leptons in the final state, however their contributions were found to be below the limit set to the $t\bar{t}$ contribution. For $Zb\bar{b}$ using the 3ℓ filter acceptance, the cross section used becomes:

$$\sigma_{eff} = \sigma_{LO} \cdot BR(Z \rightarrow e^+e^-, \mu^+\mu^-) \cdot FA \cdot K_f = 12.7 \cdot 10^3 \text{ fb}$$

In the case of WZ the cross section was calculated using a cut of 20 GeV for the off-shell Z, W masses. To account for the QCD uncertainties, the energy scale of the process was varied by a factor 2, resulting in an overall change in the cross section of 10%. The values obtained were:

$$W^- : \sigma_{NLO} = 21.684_{-0.9}^{+0.5} \pm 0.905(\text{PDF}) \pm 0.0026(\text{stat}) \text{ pb}$$

$$W^+ : \sigma_{NLO} = 34.752_{-0.9}^{+1.2} \pm 1.043(\text{PDF}) \pm 0.0039(\text{stat}) \text{ pb}$$

The effective cross section used in the analysis is:

$$\sigma_{eff} = \sigma_{NLO}(W^+Z + W^-Z) \cdot BR(W \rightarrow \ell\nu) \cdot BR(Z \rightarrow \ell\ell) \cdot FA = 26.41 \text{ fb}$$

Both $Zb\bar{b} \rightarrow 3\ell$ and the $WZ \rightarrow 3\ell$ backgrounds give negligible contributions. Therefore, no results on these backgrounds are presented in the remainder of the analysis.

The Z +jets background

The process Z +jets was also considered as a background. A proper study of this background would require a vast amount of statistics, which were not available for this analysis. However, using the available statistics of 470K events, none of them passed the lepton quality and p_T cuts discussed further in this chapter.

5.1.3 Trigger

An event needs to pass the trigger filters in order to be reconstructed. The first stage in the lepton trigger chain is the Level-one (L1) trigger. The L1 algorithms look for suitable lepton candidates in a small $\Delta\eta \times \Delta\phi$ regions known as regions of interest (RoI). The High Level Trigger runs its algorithms on the candidates found by the L1 trigger. The Level-two (L2) algorithms selects the events that will be considered by the Event Filter (EF). The EF algorithms, which are based on the final offline reconstruction algorithms, set the final event

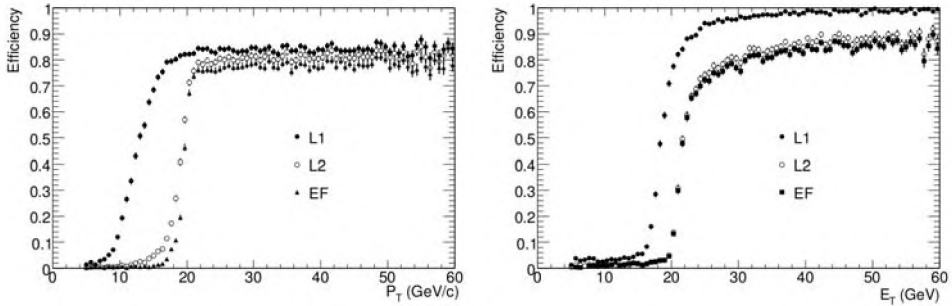


Figure 5.1: Trigger selection efficiency for muons (left) and electrons (right) as a function of p_T and E_T respectively. The errors shown are the square root of the sum of squares of weight for each bin.

Trigger Menu: $1\mu 20$ or $1e 22i$			
	$4e$	4μ	$2e 2\mu$
Before event selection	95.0 ± 0.4	96.1 ± 0.4	96.2 ± 0.4
After event selection	$> 99.8 \pm 0.2$	$> 99.8 \pm 0.2$	$> 99.8 \pm 0.2$

Table 5.4: Trigger selection efficiencies (in %) for the selected trigger menu before and after the analysis event selection.

selection. More details about the triggering process can be found in [79] for electrons and in [80] for muons.

Figure 5.1 shows the muon and electron trigger efficiency where the chosen trigger thresholds were $p_T^{thres} = 10$ GeV/ c and $E_T^{thres} = 25$ GeV. The L1 algorithm performance is close to 100%. However, in the case of muons the geometrical acceptance of the detectors used for triggering (TGCs and RPCs) is about 80%, which explains the reduced efficiency.

For this analysis the EF trigger menus chosen were: $1\mu 20$ and $1e 22$. In other words, each event must contain at least one muon with a transverse momentum above 20 GeV/ c , or an electron with a measured transverse energy above 22 GeV. Table 5.4 shows the EF efficiencies in each channel for the chosen menus. The efficiency is above 95% for the events in the sample, and is close to a 100% for those events passing the analysis selection criteria discussed later in this chapter.

5.2 Electron and muon reconstruction

In this section, the electron reconstruction is discussed. In addition, the CaloMuonTag improvements to the muon reconstruction are studied. For these studies the muon reconstruction chain `Staco+Mutag` was selected. Finally, a comparison of the fake rate for the different electron definitions and muon algorithms is presented.

5.2.1 Electron reconstruction performance

The ATLAS reconstruction software defines three different types of electrons: *Loose*, *Medium* and *Tight*. Details on these definitions and studies on their performance are found in [81].

A *Loose* electron is defined as a track reconstructed in the inner detector with an associated electromagnetic calorimeter cluster. The energy found in the electromagnetic cluster is required to be consistent with the expected energy deposited by an electron.

The *Medium* electron definition requires, in addition, a minimum number of hits in the pixel and SCT detectors and a cut on the impact parameter associated to the track: $d_0 < 10 \text{ mm}$. Also the shape of the shower of a *MediumElectron* is required to be different from the one associated to a $\pi^0 \rightarrow \gamma\gamma$ decay.

A *Tight* electron definition presents the most isolated identification and therefore best rejection against jets. However it also presents a lower efficiency than the previous definitions. The tight selection applies additional cuts to the number of hits in the B-Layer of the pixel detector and sets a maximum number of hits in the TRT. It also applies cuts to the difference in the position between the extrapolated candidate track and the actual position of the cluster in the calorimeter. Additionally, calorimeter isolation cuts inside a cone of $\Delta R < 0.2$ around the track are applied.

Figure 5.2 shows the electron identification efficiency as a function of η and E_T for the three electron definitions. The signal sample was used in order to obtain these results, selecting only events with 4 electrons in the final state.

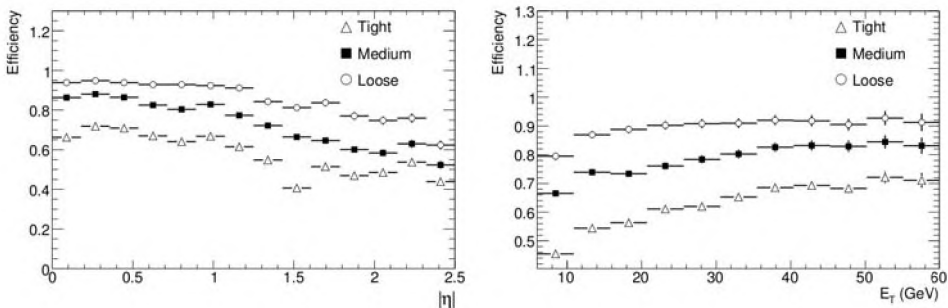


Figure 5.2: Electron reconstruction efficiency as a function of η and E_T for the three definitions using the signal sample. The errors shown are the square root of the sum of squares of weight for each bin.

5.2.2 Adding calorimeter identified muons to the analysis

Before using any of the muons identified by `CaloTrkMuId` in the analysis, several steps are taken to reduce the chances of adding wrongly identified muons to the selection. First, a cross-check with the set of reconstructed electrons in the event is performed. This reduces the possibility of adding tracks belonging to electrons being mis-tagged as muons. In addition, a maximum of one calorimeter identified muon is added each event only if there are already either one or three muons present in the container. This ensures that the calorimeter identified muons are added to the standard container only to complete the set of muons in the event. Also, specific cuts optimised to identify muons in Higgs decays are applied:

- $p_T > 7 \text{ GeV}/c$.
- $\log_{10}(E_T^{\text{iso}}/p_T) < -0.05$.

Figure 5.3 shows the η , p_T and CaloMuonTag tag distributions for the calorimeter muons added to the signal. Notice that the added calorimeter muons are found mostly around $|\eta| < 0.1$. Figure 5.4 shows the transverse momentum and tag distributions for CaloMuonTag mis-identified tracks. When comparing the distributions in the two figures, some ideas can be drawn in order to reduce the amount of fake muons:

- A geometrical cut can be set around $|\eta| < 0.1$.
- A cut on the CaloMuonTag tag can be used.
- Low- p_T tracks have higher chances of being mis-identified, therefore a suitable cut on the transverse momentum should be applied whenever possible. In this analysis a cut of $p_T > 7 \text{ GeV}/c$ proved to be enough.

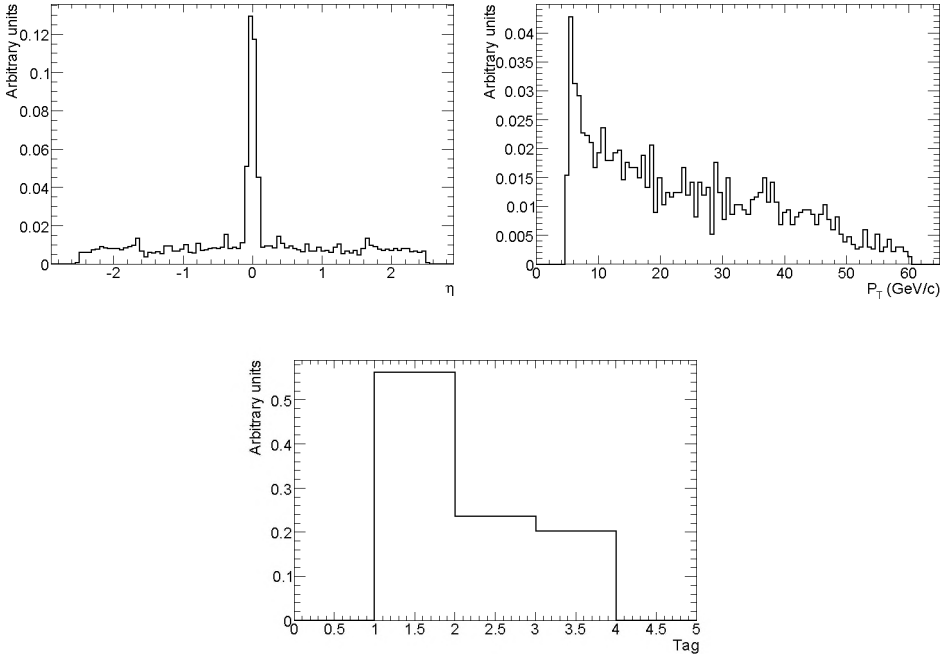


Figure 5.3: Distributions of η (left), p_T (right) and CaloMuonTag tag (bottom) for the selected CaloMuonTag muons added to the STACO+MuTag container for the signal sample.

Table 5.5 summarises the values of the fake rate associated to each algorithm for the different samples and the increase when CaloMuonTag muons are added. The results are shown with and without the application of a geometrical cut of $|\eta| < 0.1$. Here, the shown fake rate is the amount of tracks not matched to MC true muons inside a cone $\Delta R < 0.01$ in every 1000 events. Results obtained using the three electron definitions are added to the table for comparison. The cuts $p_T > 7 \text{ GeV}/c$ and $|\eta| < 2.5$ were applied to the leptons in

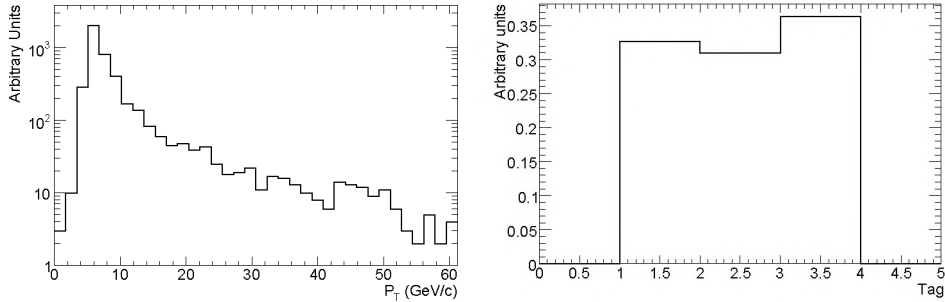


Figure 5.4: Distributions of p_T (left) and CaloMuonTag tag (right) for the CaloMuonTag mis-identified muons added to the $\text{STACO}+\text{MuTag}$ container for the signal sample.

all the samples. Notice that even without the application of the geometrical cut, the fake rate increase caused by CaloMuonTag is of the order of the fake rate associated to the *Medium* and well below the *Loose* electron definitions. When the geometrical cut is applied to the calorimeter muons, the increase of the fake rate in the container is marginal.

Figure 5.5 shows the efficiency gain in the background samples, as a function of both η and p_T , when combining MuTag and CaloMuonTag with Staco . The Figure 4.19 of the previous chapter shows the same results for the signal. Again, the largest gains are found around $\eta < 0.1$. In samples with non-isolated muons, such as in the $t\bar{t}$ and $Zb\bar{b}$ cases, the efficiency gain obtained from adding calorimeter muons is reduced.

	$H \rightarrow 4\ell$	$ZZ \rightarrow 4\ell$	$Zb\bar{b} \rightarrow 4\ell$	$t\bar{t} \rightarrow 4\ell$	$Z \rightarrow \mu^+\mu^-$ inc.
Comb. Rec.	5.20	2.39	14.14	36.59	1.78
Calo muon+GC	0.18	0.90	1.16	1.43	0.89
Total	5.38	3.29	15.30	38.02	2.67
Calo muon	3.62	5.11	19.13	27.88	16.37
Total	8.82	7.50	33.27	64.47	18.15
Elec. loose	70.21	62.82	130.59	254.11	36.58
Elec. medium	23.72	25.71	60.45	108.00	17.99
Elec. tight	0.32	0.93	13.65	30.6	0.50

Table 5.5: Number of fakes in every 1000 events for the combined muon reconstruction and the increase when using CaloMuonTag, with and without the geometrical cut (GC): $|\eta| < 0.1$. For comparison, the expected fake rate for the three different electron definitions is shown for the same samples. The cuts of $p_T > 7$ GeV/c and $|\eta| < 2.5$ were applied for the lepton selection.

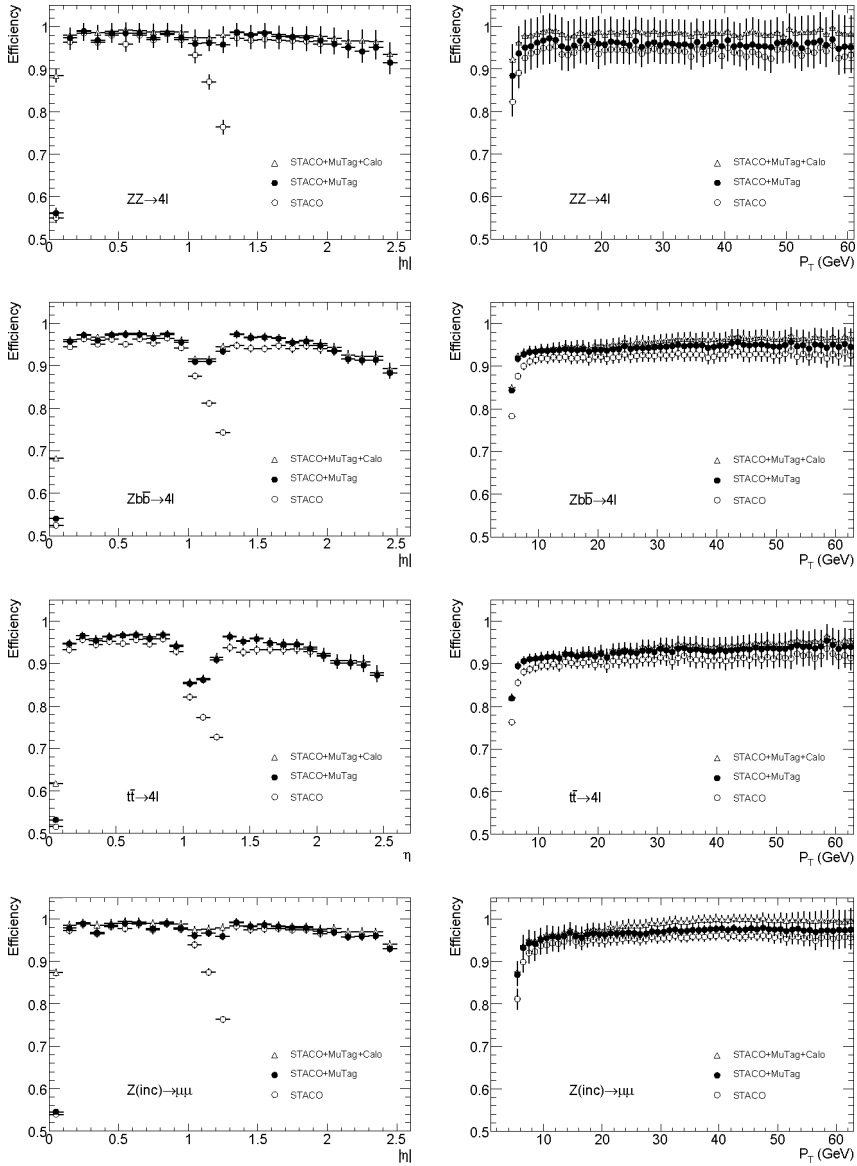


Figure 5.5: Reconstruction efficiency as a function of η (left) and p_T (right) for the algorithms: *STACO*, *STACO+MuTag*, and when one extra *CaloMuonTag* muons is added to the samples. Starting from top to bottom: $ZZ \rightarrow \mu^+\mu^-$, $Zb\bar{b} \rightarrow 4\ell$, $t\bar{t} \rightarrow 4\ell$ and $Z(\text{inc}) \rightarrow \mu^+\mu^-$. The errors shown are the square root of the sum of squares of weight for each bin.

5.3 Reducible background rejection

This section presents a study on the isolation and impact parameter cuts that are chosen in order to reduce the $Zb\bar{b}$ and $t\bar{t}$ backgrounds. Muons originating in Z boson decays are expected to be more isolated than muons produced in heavy quark leptonic decays. Also, since the b and c quarks live long enough to decay at some distance from the interaction point, the particles product of their decay can be associated to secondary vertices.

To be safe against the large uncertainties on the production cross sections for $Zb\bar{b}$ and $t\bar{t}$ backgrounds, the cuts are chosen such that the reducible background rate is not higher than one third of the $ZZ^{(*)}$ rate.

5.3.1 Lepton isolation

Both track isolation and calorimeter isolation criteria are used as discriminants. The track isolation is defined as the sum of the transverse momenta of all the tracks inside a cone $\Delta R = \sqrt{\Delta\eta^2 + \Delta\phi^2} < 0.2$ around the lepton track. For this, the track of the lepton considered is not included in the sum. For electrons, in order to remove tracks associated to *bremstrahlung* photo-conversions from the sum, only tracks with at least one hit in the first pixel detector layer (B-layer) are used in the calculation. The calorimeter isolation discriminant is defined as the sum of the energy measured in the different calorimeters inside the same cone size. Again, the energy deposited associated to the lepton considered for isolation is excluded from the calculation.

Figure 5.6 shows the rejection power of the $Zb\bar{b}$ background as a function of the selection efficiency for the signal. Figure 5.7 shows that if the isolation parameter (either p_T or E_T) is normalised to the transverse momentum of the lepton, the discrimination power of the isolation cut improves. Figure 5.8 shows the calorimeter isolation energy for both muons and electrons. Figure 5.9 shows normalised track isolation distributions for both types of leptons.

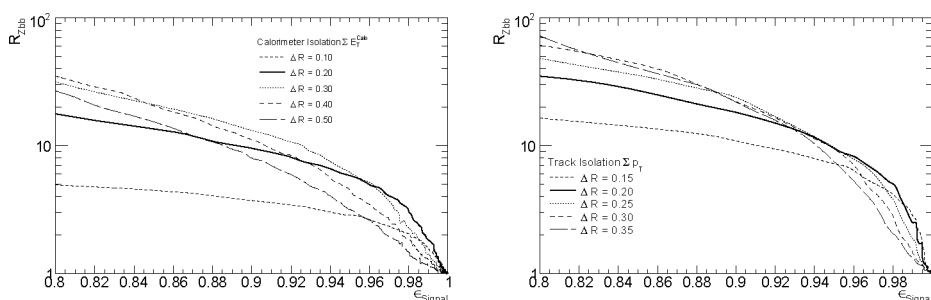


Figure 5.6: $Zb\bar{b}$ rejection versus the $H \rightarrow 4\mu$ selection efficiency for various calorimeter (left) and track (right) isolation cone sizes.

5.3.2 Impact Parameter

The leptons produced in $t\bar{t}$ and $Zb\bar{b}$ processes have as decay product b -quarks originating in secondary vertices. Hence, further background rejection can be achieved by imposing a cut on the impact parameter (d_0). To minimise the effect of the uncertainty in the d_0 calculation

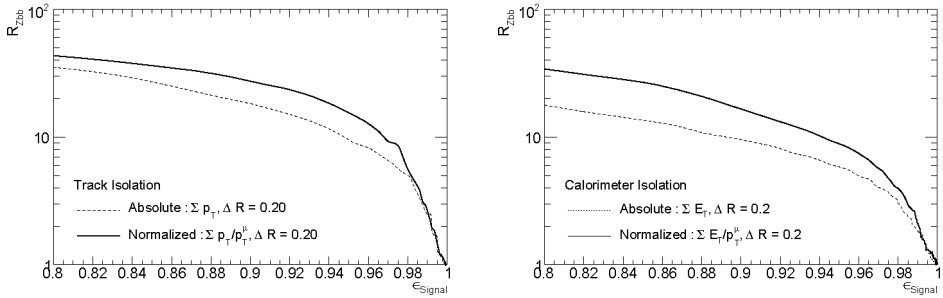


Figure 5.7: Comparison of track (left) and calorimeter (right) $Zb\bar{b}$ rejection versus $H \rightarrow 4\mu$ for standard and normalised isolation energies calculated in a $\Delta R=0.2$ cone around the muon track.

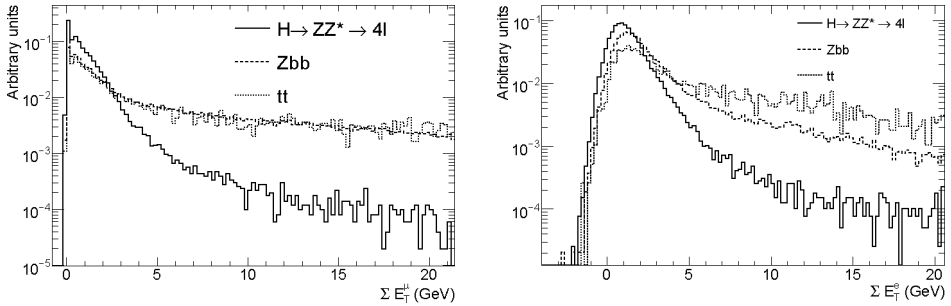


Figure 5.8: Calorimeter isolation energy inside $\Delta R=0.2$, for muons (left) and electrons (right), for the signal, the $Zb\bar{b}$ and $t\bar{t}$ backgrounds.

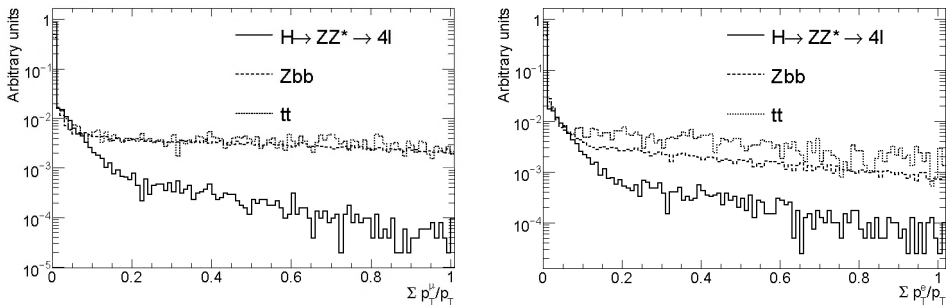


Figure 5.9: Normalised track isolation energy inside $\Delta R=0.2$, for muons (left) and electrons (right), for the signal the $Zb\bar{b}$ and $t\bar{t}$ backgrounds.

the impact parameter significance (d_0/σ_{d_0}) is used instead. The error in the vertex position is $15 \mu\text{m}$ along the transverse x and y coordinates. To have the best possible accuracy, the impact parameter is calculated with respect to the primary vertex. The primary vertex is found by fitting several tracks extrapolated back to the beam spot. Figure 5.10 shows

distributions of impact parameter significance for muons and electrons.

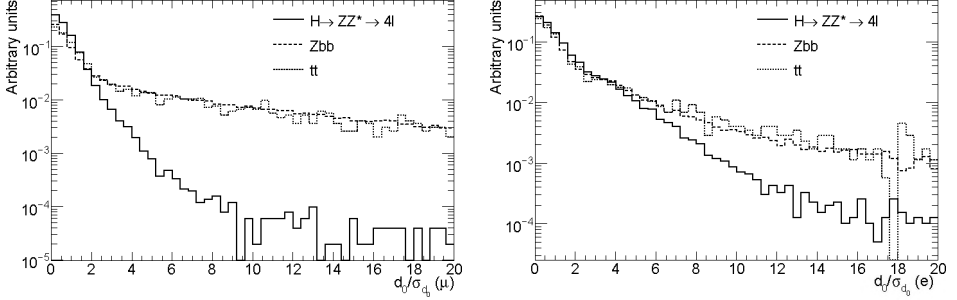


Figure 5.10: Impact parameter significance for muons (left) and electrons (right) in signal and reducible background events .

5.3.3 Selection Cuts

The set of cuts on the lepton isolation energy and impact parameters was chosen to guarantee that at least 90% of the signal events pass the selection criteria. The final cuts used in the analysis are:

- Track isolation: $\Sigma p_T / p_T < 0.15$.
- Calorimeter isolation: $\Sigma E_T / p_T < 0.23$.
- Impact parameter significance (d_0 / σ_{d_0}): lower than 3.5 for muons and 6 for electrons.

For the electrons, a higher value on the impact parameter significance cut is chosen since *bremsstrahlung* causes a smearing on the electron impact parameter distribution.

Figure 5.11 shows the distributions and cuts applied on the isolation variables used as discriminants. Figure 5.12 shows distributions for the impact parameter significance for the lepton in the event with the largest d_0 .

5.4 Event Selection and mass reconstruction

Only events passing the trigger criteria and containing at least 4 reconstructed leptons with $p_T > 5 \text{ GeV}/c$ and within $|\eta| < 2.5$ are considered. In order to minimise the inclusion of mis-tagged electrons tracks, the set of reconstructed electrons and muons are cross-checked and any overlap removed. After the event preselection, the leptons are sorted into pairs. The leptons in each pair must pass different p_T cuts. Kinematic cuts are applied to the di-lepton invariant mass in each pair so that the high- p_T pair successfully reconstructs an on-shell Z , whilst the low- p_T pair reconstructs the off-shell $Z^{(*)}$. After the Z boson mass cuts are applied, the leptons must pass the isolation and vertexing criteria described in the previous section. For the computation of the signal significance over the remaining background, a final cut on the invariant mass of the lepton quartet in a window around the expected Higgs mass is applied.

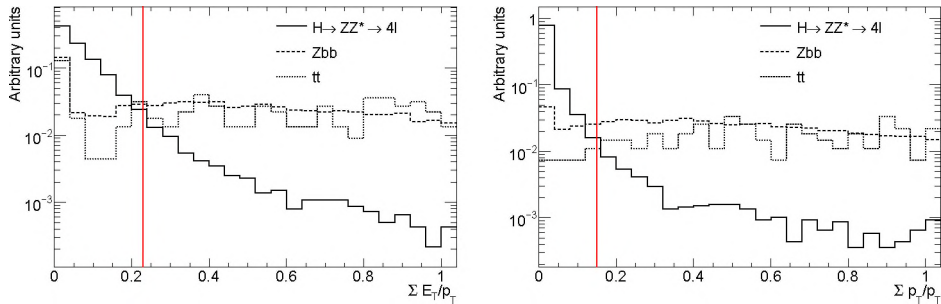


Figure 5.11: Lepton normalised calorimeter (left) and track (right) isolation energy inside $\Delta R=0.2$ for the signal, the $Zb\bar{b}$ and $t\bar{t}$ backgrounds. The vertical line shows the value of the cut applied in the event selection.

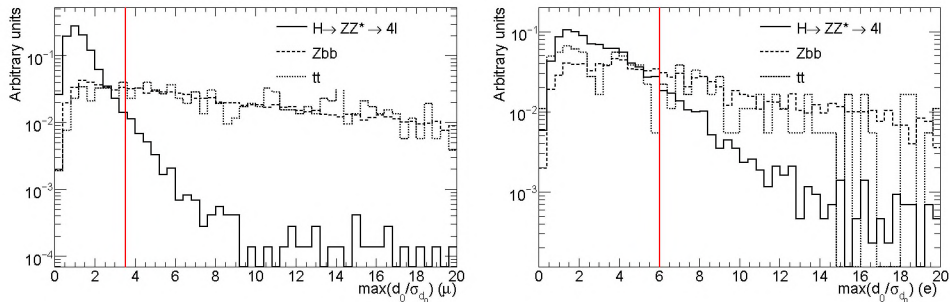


Figure 5.12: Maximum impact parameter significance for muons (left) and electrons (right) in signal and reducible background events. The vertical line shows the value of the cut applied in the event selection.

5.4.1 Lepton pairing, isolation and vertexing

Leptons passing the trigger and preselection criteria are grouped in pairs of the same flavour and opposite sign. The leptons in the first pair are required to have a transverse momentum above $20 \text{ GeV}/c$, while the leptons in the second pair must have a transverse momentum of at least $7 \text{ GeV}/c$. This criteria together with the cuts applied are summarised in Table 5.6. Additionally, when the high- p_T pair is formed by electrons, which are required to be consistent with at least the *MediumElectrons* criteria described in Chapter 3.

In the case of muons, the reconstruction chain *Muonboy+Staco+Mutag* is used. This chain presents reconstruction efficiencies above 95% for the samples considered. However, the fact that four well isolated muons are required for this analysis, means that the efficiency in the muon reconstruction will scale up to the power of four. This emphasises the importance of calorimeter muon identification in this channel. Furthermore, since calorimeter muon identification is performed only over well isolated tracks, the increase in the background selection is very small for $Zb\bar{b}$ and $t\bar{t}$. The improvements in the 4μ and $2e2\mu$ channels caused by *CaloMuonTag* muons are studied. In order to minimise the addition of mis-identified muons, a *CaloMuonTag* muon is only added to complete the lepton quadruplet in the event. *CaloMuonTag* muons used, are selected following the criteria described in

Section 5.2.2 with the additional isolation cut $\log_{10}(E_T/p_T) < -0.05$ described in the same section. Since most of the gain obtained using `CaloMuonTag` is found around $\eta < 0.1$, a geometrical cut can be applied reducing dramatically the amount of fakes added to the standard muon container.

In events with more than 4 reconstructed leptons, where more than one lepton quadruplet is possible, the one chosen for the analysis is the one with the high- p_T pair with an invariant mass closest to the nominal Z mass, and a low- p_T pair formed using the largest possible p_T lepton pair with same flavour and opposite sign.

5.4.2 Higgs mass reconstruction

In this analysis the high- p_T lepton pair is associated to the decay product of the on-shell Z , and the low- p_T pair to the decay of the off-shell Z . A cut around the Z -mass is applied to the di-lepton invariant mass of the first pair: $|M_{12} - M_Z| < 15 \text{ GeV}/c^2$. Also, the momentum of the reconstructed leptons of the first pair is corrected using the convolution of a nominal Z Breit-Wigner distribution with a gaussian distribution. The values for the mean and σ used for the gaussian distribution are obtained fitting the reconstructed invariant mass of the lepton pair. A lower cut is applied to the di-lepton invariant mass of the low- p_T pair, $M_{34} > 20 \text{ GeV}/c^2$. Table 5.8 summarises the kinematic cuts applied. Unfortunately these two cuts are uncorrelated and although about 85% of the generated signal events pass both individual cuts, only 70% of the events pass both cuts at the same time. Figure 5.13 shows distributions for the di-lepton invariant mass for MC true leptons in Z and $Z^{(*)}$ decays.

The two pairs of leptons associated to the Z and $Z^{(*)}$ bosons are combined to reconstruct the Higgs mass. A final cut of $\pm 2\sigma_{M_H}$ around the reconstructed invariant mass of the lepton quartet is applied before computing the signal over background significance. The σ_{M_H} is obtained fitting the invariant mass in the gaussian region of the distribution for each decay channel independently. Fitted distributions of the lepton quartet invariant mass are shown in Figure 5.14. For the $4e$ invariant mass distribution, the effect of the electron energy loss due to *bremsstrahlung* processes causes the invariant mass distribution to be non-gaussian. This also produces a shift on the reconstructed Higgs invariant mass. This effect can clearly be noticed. Table 5.9 presents the values of σ_{M_H} used in the analysis for each channel.

5.4.3 Event selection results

The cuts described in the previous sections are applied in the following order:

Pairing
Four leptons with $ \eta < 2.5$,
Two pairs of leptons (p_{12} , p_{34}): same flavour and opposite charge.
Leptons in first pair with $p_T > 20 \text{ GeV}/c$. in second pair with $p_T > 7 \text{ GeV}/c$,

Table 5.6: Pairing of the leptons to reconstruct the $Z, Z^{(*)}$ bosons and cuts applied.

<p>Isolation and vertexing</p> <p>Isolation ($\Delta R < 0.20$): Calorimeter $\Sigma E_T / p_T < 0.23$ Track $\Sigma p_T / p_T < 0.15$</p> <p>Calo-μ ($\Delta R < 0.45$): $\log_{10}(E_T / p_T) < -0.05$</p> <p>Lepton with highest impact parameter: muons: $d_0 / \sigma_{d_0} < 3.5$ electrons: $d_0 / \sigma_{d_0} < 6.0$</p>

Table 5.7: Isolation and vertexing cuts applied in the analysis.

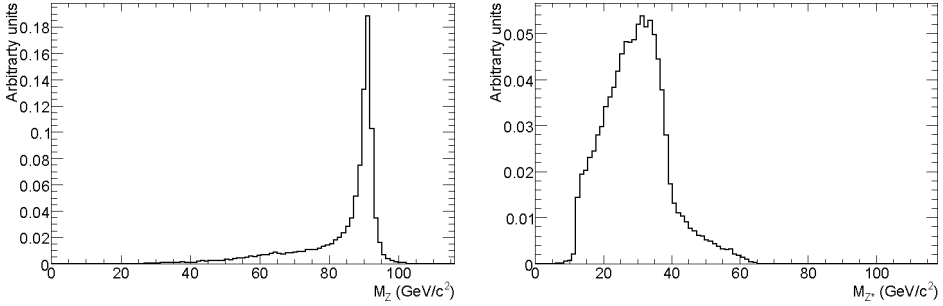


Figure 5.13: MC true leptons di-mass reconstruction for the generated on-shell Z boson (left) and off-shell $Z^{(*)}$ (right).

1. Events passing the trigger criteria.
2. Events with four leptons inside the η and p_T preselection cuts.
3. Lepton pairing.
4. Di-lepton invariant mass cuts
5. Calorimeter isolation.
6. Track isolation.

<p>Kinematic Cuts</p> <p>$M_{12} - M_Z < 15 \text{ GeV}/c^2$ $M_{34} > 20 \text{ GeV}/c^2$ $M_H \pm 2\sigma_{M_H}$</p>

Table 5.8: Kinematic cuts applied to the reconstructed bosons.

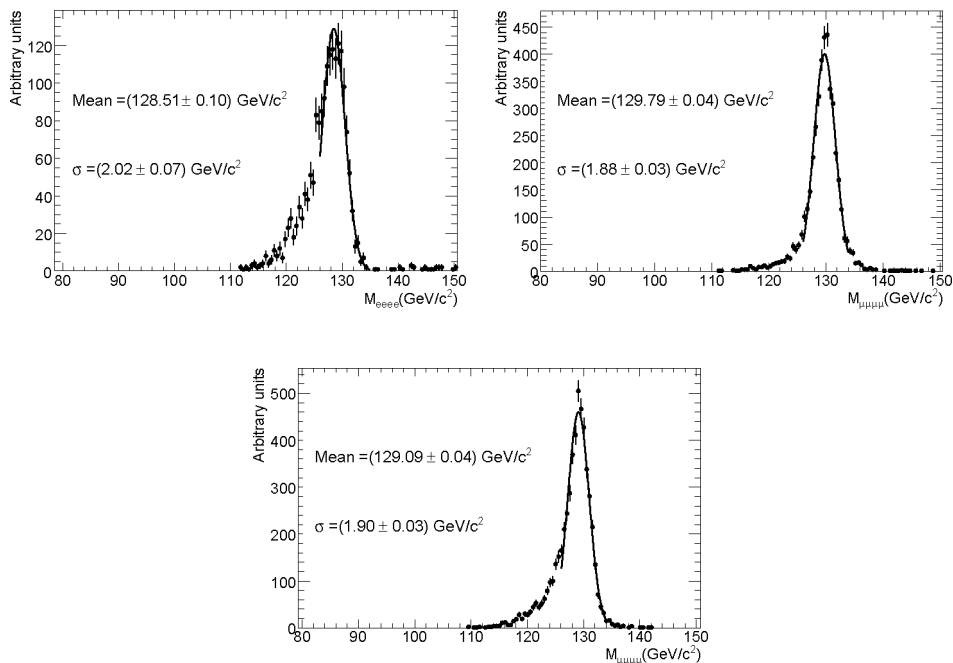


Figure 5.14: Reconstructed 4-lepton invariant mass after application of the Z-mass constraint fit for the 4e (left), 4μ (right) and 2e2μ (bottom) channels. The errors shown are the square root of the sum of squares of weight for each bin.

7. Impact parameter significance cuts for muons and electrons.

8. 4-lepton invariant mass cut around the Higgs mass considered in the analysis.

The fraction of events (in %) passing each of the cuts for the signal is shown in Table 5.10. These fractions represent the percentage with respect to the number of generated events in each of the different channels. In the last row, the result obtained after the application of the geometrical cut $|\eta| < 0.1$ to the calorimeter muons is shown. For comparison purposes the last two columns of Table 5.10 show the results when the analysis is done without complementing the muon reconstruction using calorimeter muons.

The net improvement in the number of events passing all the cuts when using calorimeter identified muons is 14% in the 4μ channel and 6% in the 2e2μ channel. When a geometry cut $|\eta| < 0.1$ is applied, the gain is 10% and 4% respectively.

	GeV/c²	
σ_{M_H}	4e	2.0
	4μ	1.9
	2e2μ	1.9

Table 5.9: Resolution of the reconstructed four lepton invariant mass in each channel.

The reconstruction efficiency is lower for electrons than for muons, especially when the calorimeter muons are used. This causes the fraction of events in the $4e$ channel passing the lepton preselection and pairing criteria to be much lower than in the case of the 4μ channel as shown in Table 5.10.

Tables 5.11, 5.12 and 5.13 show the fraction (in %) of the events passing each cut with respect to the total number of events in each background sample considered: $ZZ^{(*)}$, $Zb\bar{b}$ and $t\bar{t}$ respectively. The results obtained when the geometrical cut is applied to the calorimeter muons are shown in the last row. The last two columns show the results when the calorimeter muons are not included in the analysis. In the case of the $t\bar{t}$ background sample the available statistics were not enough to determine the fraction of events that would pass all the selection cuts.

Table 5.14 presents the number of background events expected in each channel, as well as the total sum for an integrated luminosity of 30 fb^{-1} . The last row shows the signal over background significance in each decay channel and for the combination of these channels. The significance was calculated as:

$$\sigma = \frac{S}{\sqrt{S+B}}$$

where S is the number of signal events and B stands for the sum of the number of events passing all cuts. Notice the increase in significance when the calorimeter identified muons are included in the analysis. Figure 5.15 shows the expected invariant mass reconstruction for the signal and the main backgrounds, using the same integrated luminosity. These results show that the discovery of a light Higgs boson in the $H \rightarrow ZZ^{*} \rightarrow 4\ell$ channel with a 5σ significance will be possible in ATLAS at an integrated luminosity of 30 fb^{-1} .

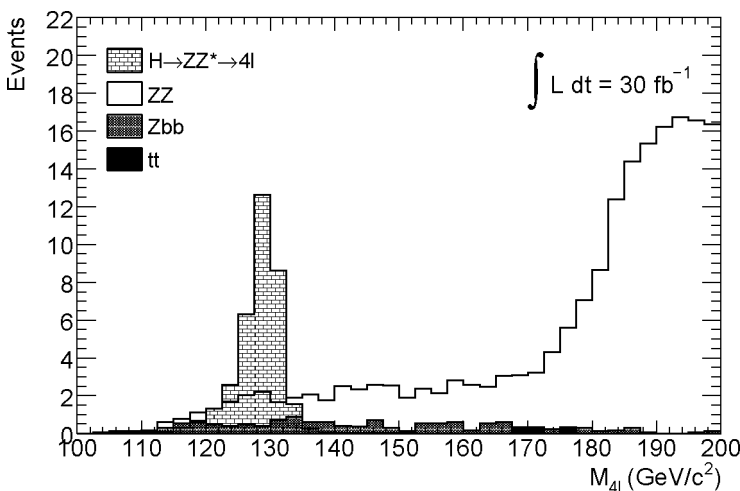


Figure 5.15: Four lepton invariant mass for signal and background with an integrated luminosity of 30 fb^{-1} .

Signal						
Selection cut		with calo muons			w/o calo muons	
		4e	4 μ	2e2 μ	4 μ	2e2 μ
Trigger selection	1	95.0	96.1	96.2	96.8	96.5
Lepton preselection	2	66.6	85.9	74.0	74.1	69.4
Lepton quality and p_T	3	43.4	71.3	55.5	62.3	52.3
Z's mass cuts	4	22.2	51.2	33.2	44.7	31.2
Calo Isolation	5	22.2	46.9	29.9	40.1	28.2
Tracker Isolation	6	20.4	43.9	28.8	38.4	27.1
IP cut	7	18.3	42.1	26.7	36.8	25.4
Higgs Mass cut	8	14.4	36.0	21.7	31.5	20.5
$ \eta < 0.1$			34.7	21.3		

Table 5.10: Fraction of events (in %) selected after each event selection cut. The efficiencies are calculated with respect to the fraction of events in which the Higgs decays into the corresponding channel passing the generator filter. For comparison, the last two columns present the results obtained when no calorimeter muons are used in the analysis. The final fractions, after all cuts, when applying a geometrical cut of $|\eta| < 0.1$ to the calorimeter muons, are given in the last row.

ZZ						
Selection cut		with calo muons			w/o calo muons	
		4e	4 μ	2e2 μ	4 μ	2e2 μ
Trigger	1	97.8	97.5	97.7	97.7	97.8
Preselection	2	15.5	20.1	34.9	17.3	32.3
Lepton quality and p_T	3	11.8	18.2	29.8	15.9	27.9
Z mass cuts	4	10.4	16.8	26.5	14.7	24.8
Calo Isolation	5	10.4	15.8	25.4	13.9	23.8
Track Isolation	6	10.0	15.4	24.9	13.5	23.3
IP cut	7	8.8	14.8	22.7	13.0	21.3
Higgs Mass window	8	$8.3 \cdot 10^{-2}$	0.13	0.17	0.12	0.16
$ \eta < 0.1$			0.13	0.17		

Table 5.11: Fraction of events (in %) selected after the application of each selection cut for the ZZ^(*) background process. For comparison, the last two columns present the results obtained when no calorimeter muons are used in the analysis. The final fractions, after all cuts, when applying a geometrical cut of $|\eta| < 0.1$ to the calorimeter muons, are given in the last row.

Zbb						
Selection cut		with calo muons			w/o calo muons	
		4e	4 μ	2e2 μ	4 μ	2e2 μ
Trigger	1	93.3	92.4	93.0	93.4	93.4
Preselection	2	6.3	11.9	17.7	9.0	14.9
Lepton quality and p_T	3	0.73	3.91	4.21	3.35	3.84
Z mass cuts	4	0.20	1.38	1.18	1.15	1.0
Calo Isolation	5	0.20	$9.7 \cdot 10^{-2}$	0.22	$8.4 \cdot 10^{-2}$	0.20
Track Isolation	6	$3.9 \cdot 10^{-2}$	$3.8 \cdot 10^{-2}$	$5.9 \cdot 10^{-2}$	$3.4 \cdot 10^{-2}$	$5.3 \cdot 10^{-2}$
IP cut	7	$1.9 \cdot 10^{-2}$	$1.2 \cdot 10^{-2}$	$2.5 \cdot 10^{-2}$	$1.1 \cdot 10^{-2}$	$2.1 \cdot 10^{-2}$
Higgs Mass window	8	$1.9 \cdot 10^{-3}$	$1.5 \cdot 10^{-3}$	$3.9 \cdot 10^{-3}$	$1.2 \cdot 10^{-3}$	$2.9 \cdot 10^{-3}$
$ \eta < 0.1$			$1.2 \cdot 10^{-3}$	$3.1 \cdot 10^{-3}$		

Table 5.12: Fraction of events (in %) selected after the application of each selection cut for the $Zb\bar{b}$ background process. For comparison, the last two columns present the results obtained when no calorimeter muons are used in the analysis. The final fractions, after all cuts, when applying a geometrical cut of $|\eta| < 0.1$ to the calorimeter muons, are given in the last row.

tt						
Selection cut		with calo muons			w/o calo muons	
		4e	4 μ	2e2 μ	4 μ	2e2 μ
Trigger	1	74.5	81.2	78.7	83.4	80.20
Preselection	2	4.52	6.8	17.8	4.3	15.2
Lepton quality and p_T	3	0.18	1.49	2.09	1.22	1.88
Z mass cuts	4	$2.8 \cdot 10^{-2}$	0.33	0.23	0.27	0.20
Calo Isolation	5	$2.8 \cdot 10^{-2}$	$2.9 \cdot 10^{-3}$	$2.1 \cdot 10^{-2}$	$1.8 \cdot 10^{-3}$	$1.8 \cdot 10^{-2}$
Track Isolation	6	$1.6 \cdot 10^{-3}$	$2.6 \cdot 10^{-4}$	$1.0 \cdot 10^{-3}$	$2.6 \cdot 10^{-4}$	$1.0 \cdot 10^{-3}$
IP cut	7	$1.1 \cdot 10^{-3}$	-	$2.6 \cdot 10^{-4}$	-	$2.6 \cdot 10^{-4}$
Higgs Mass window	8	-	-	-	-	-

Table 5.13: Fraction of events (in %) selected after the application of each selection cut for the $t\bar{t}$ background process. For comparison, the last two columns present the results obtained when no calorimeter muons are used in the analysis.

	4e	4 μ	2e2 μ	total
Signal	4.26	10.77	12.88	27.91
ZZ	1.30	2.10	2.63	6.03
Zbb	0.47	0.35	0.94	1.77
Significance (σ)	1.96	3.23	3.46	5.12
Significance (no calo muons) (σ)	1.96	3.02	3.39	4.94

Table 5.14: Expected number of events and significance ($\sigma = S/\sqrt{S+B}$), in each channel and the combined total, for an integrated luminosity of 30 fb^{-1} . For comparison, the last row shows the significance obtained in the analysis when not using calorimeter identified muons.

	4e	4 μ	2e2 μ
No Pileup+CB	14.5	36.0	21.7
Pileup+CB	13.0	31.4	18.2

Table 5.15: Selection efficiencies after all cuts for each of the three decay channels. The results are for samples with and without the overlaid pileup and cavern background.

Pileup and cavern background

Overlaying pileup and cavern background with the MC signal sample has several effects that degrade the selection efficiency. The lepton reconstruction efficiency suffers, while the lepton reconstruction fake rate increases. It also makes the accurate determination of the primary vertex more challenging. The most critical effect having a direct impact on the analysis, is that leptons produced in Z decays are not as well isolated. The selection efficiency for the three different decay channels when the effects of pileup and cavern background are considered, are listed in Table 5.15. The net result is a degradation of the selection efficiency of around 10% in each channel. However, the re-optimisation of the cuts can be used to recover part of the loss in efficiency.

5.5 Systematics Uncertainties

In this section a study on the systematic uncertainties associated to the signal and background efficiencies is presented. The theoretical uncertainties are presented first, followed by a discussion on the impact of experimental systematic uncertainties. The results are summarised in Table 5.16 for the signal and main backgrounds in the different decay channels. A 3% uncertainty on the luminosity was assumed for the calculation of the total systematic uncertainties.

For the calculation of the NLO cross sections, the QCD renormalisation and factorization scales were varied independently from 0.5 to 2 times the energy scale, resulting in a variation of 10% in the cross sections obtained. The uncertainties on the QCD energy scale reflect the omission of higher order diagrams in the calculation of the cross sections. The uncertainties on the PDF were estimated using different sets of CTEQ6M functions.

The systematics in the lepton reconstruction determine the source of experimental un-

	$Zb\bar{b}$	$ZZ^{(*)}$	H	$Zb\bar{b}$	$ZZ^{(*)}$	H	$Zb\bar{b}$	$ZZ^{(*)}$	H
	$4e$			4μ			$2e2\mu$		
E. scale (+)	+1.5	+0.1	+0.9	+2.4	+0.4	+1.3	+1.9	+0.1	+0.9
E. scale (-)	-1.1	-0.2	-0.5	-2.3	-0.3	-2.5	-1.7	-0.2	-1.4
Resolution	-0.5	-0.1	-0.4	+0.1	-0.1	-2.6	-0.2	-0.1	-0.5
Rec. efficiency	-1.0	-0.7	-0.5	-3.8	-4.0	-3.8	-2.0	-2.1	-1.7
Luminosity	3			3			3		
Total	3.6	3.1	3.2	5.4	5.0	6.0	4.1	3.7	3.8

Table 5.16: Systematic uncertainties in % for selection efficiencies in the three different channels for signal and backgrounds.

certainties for the $H \rightarrow 4\ell$ analysis. The systematics arise from errors in the determination of the lepton energy scale, as well as from errors in the determination of the lepton reconstruction and identification efficiency. In this analysis the experimental uncertainties were estimated varying the reconstructed quantities. The amount used for these variations were suggested by the lepton reconstruction performance groups.

Lepton energy scale. The main source of uncertainties in the determination of the electron energy scale, are possible errors in the calibration of the EM calorimeter. In this study, the E_T of the reconstructed electrons was varied by $\pm 0.5\%$. In the case of muons, the main source of uncertainties in the momentum determination is due to the imperfect knowledge of the complex toroidal magnetic field. To estimate this uncertainty the p_T of the reconstructed muons was varied by $\pm 1\%$.

Lepton reconstruction efficiency. Performance group studies have set the uncertainties in the lepton reconstruction at 0.2% for electrons and 1% for muons.

Lepton energy resolution. To estimate possible errors in the estimation of the amount of material considered for the lepton energy reconstruction, the lepton energy distributions are smeared using a gaussian distribution. The electrons energy was smeared using a $\sigma_{ET} = 0.0073 \cdot E_T$. When this smearing is applied to a sample of single electrons generated with $E_T = 50$ GeV the reconstructed transverse energy resolution degraded by 10%. For muons, an additional term was added to the smearing to account for misalignment uncertainties. The total smearing used, $\sigma_{1/p_T} = 0.011/p_T \oplus 0.00017$, has the effect of a 10% increase in the muon nominal resolution.

Material effects in electron efficiency

The uncertainties in electron efficiency depend largely on the amount of material considered to be traversed by the electron when travelling through the inner detector and electromagnetic calorimeter. As discussed in [81], variations on the amount of material considered, change the shapes of the discriminant variables used for the electron identification. The uncertainty in the reconstruction efficiency, due to these effects, is estimated to be about 2%. However, the true systematic uncertainty in the reconstruction efficiency, due to the variations in the amount of material considered, can only be accurately estimated from data.

CHAPTER 6

CONCLUSIONS

The question of the existence of the Higgs boson has evaded high energy physics experiments for many years. The LHC experiment will bring unprecedented insights into the world of particle physics. It will either confirm the existence of the Higgs particle or push the allowed mass range to limits where new theories will be needed to explain the experimental observations. ATLAS, a multi-purpose detector, will profit from the large centre of mass energy and high luminosity that the LHC experiment will deliver.

Good lepton reconstruction is important for most physics analyses in ATLAS. In the case of muons, the ATLAS reconstruction software implements several algorithms which can be grouped as:

- *Standalone*: Algorithms that reconstruct the tracks using only the hit information provided by the muon spectrometer.
- *Combined*: Which match the standalone tracks to the inner detector tracks producing new re-fitted tracks.
- *Taggers*: Which match inner detector tracks to segments found in the spectrometer but were not used in the reconstruction of standalone tracks.

A different approach for muon identification, which is independent to those mentioned above, is to match inner detector tracks to energy deposit patterns in the calorimeter consistent with a *minimum ionising particle*. This thesis described the implementation of a calorimeter tagger which complements the muon reconstruction in the regions where the spectrometer presents design limitations. This algorithm can also be used to recover those low-momentum muons that produce marginal activity in the spectrometer. Calorimeter taggers make muon identification more robust. In the eventuality that one or more sectors of the muon spectrometer are less efficient, muon identification in the calorimeters might be the only way to guarantee a good muon reconstruction efficiency.

The $H \rightarrow ZZ^{(*)} \rightarrow 4\ell$ analysis is one of the most important channels for Higgs studies in ATLAS. The impact of the use of the calorimeter tagger in this channel was studied. A final improvement of 14% in the 4μ and 6% in the $2e2\mu$ channels was found. Since most of the efficient gain lies around $|\eta| < 0.1$. If the contribution of the tagger is limited to this region, an improvement of 10% in the 4μ and 4% in the $2e2\mu$ channels can still be expected, while the added fake rate is negligible.

REFERENCES

- [1] http://en.wikipedia.org/wiki/Particle_physics. 1
- [2] A. Salam Glashow, S. L.S. Weinberg. Elementary particle theory. 3
- [3] S. Weinberg. *The Quantum Theory of Fields*. University of Candbridge Press Syndicate, 1995. ISBN 0-521-55001-7. 3
- [4] R. Feynman. *QED: The strange theory of light and matter*. Princeton Univ. Press., 2006. ISBN 0-691-12575-9. 4
- [5] M. Gell-Mann. *The Quark and the Jaguar*. Owl Books, 1995. ISBN 978-0805072532. 5
- [6] S.F. Novaes. Standard model: An introduction. hep-ph/0001283 2000. 6
- [7] P. W. Higgs. Broken symmetries and the masses of gauge bosons. *Phys. Rev. Lett.*, 13:508–509, 1964. 8
- [8] F. Englert and R. Brout. Broken symmetry and the mass of gauge vector mesons, 1964. 8
- [9] S. Weinberg. A model of leptons. *Phys. Rev. Lett.*, 19:1264–1266, 1967. 9
- [10] K. Riesselmann. Limitations of a standard model Higgs boson, 1997. hep-ph/9711456. 9, 10
- [11] R. Barate et al. Search for the standard model Higgs boson at LEP. *Phys. Lett.* , B565:61–75, 2003. 11, 12
- [12] The LEP Electroweak Working Group. A Combination of Preliminary, Electroweak Measurements and Constraints on the Standard Model, 2007. LEP EW WG Plots for the Winter 2007. 11
- [13] Q. Jianming. Higgs searches at the fermilab tevatron ppbar collider. arxiv:0812.3979, 2008. 12
- [14] ATLAS Collaboration. Expected performance of the atlas experiment, detector, trigger and physics. CERN-OPEN-2008-020, Geneva, 2008. 12, 15, 59
- [15] B. Mellado et al. Higgs production cross-sections and branching ratios for the atlas higgs working group, 2007. ATLAS Note ATL-COM-PHYS-2007-024. 13, 79
- [16] Djouadi A. Brein, O. and Harlander R. Nnlo qcd corrections to the higgs-strahlung processes at hadron colliders. *phys. lett.* b579, 2004. 14

- [17] A. Djouadi et al. HDECAY: A program for Higgs boson decays in the Standard Model and its supersymmetric extension. *Comput. Phys. Commun.*, 108:56–74, 1998. [15](#)
- [18] LHC Study Group. The large hadron collider: Conceptual design. CERN-AC-95-05-LHC. [17](#)
- [19] ATLAS Collaboration. The atlas experiment at the cern large hadron collider, 2008. [17](#)
- [20] CMS Collaboration. the compact muon solenoid: Technical proposal. CERN-LHCC-94-38. [17](#)
- [21] ALICE Collaboration. Alice: Technical proposal for a large ion collider experiment at the cern lhc. CERN-LHCC-95-7. [17](#)
- [22] S. Amato et al. Lhcb technical proposal. CERN-LHCC-98-04. [17](#)
- [23] V. Berardi et al. TOTEM: Technical design report. Total cross section, elastic scattering and diffraction dissociation at the Large Hadron Collider at CERN. CERN-LHCC-2004-002. [17](#)
- [24] O. Adriani et al. Technical design report of the LHCf experiment: Measurement of photons and neutral pions in the very forward region of LHC. CERN-LHCC-2006-004. [17](#)
- [25] ATLAS Collaboration. Inner Detector: Technical Design Report. CERN/LHCC/97-016/017 (1997). [20](#)
- [26] ATLAS Collaboration. Atlas pixel detector: Technical design report. CERN/LHCC/98-013 (1998). [20](#)
- [27] M. S. Alam et al. The atlas silicon pixel sensors, 2001. [20](#)
- [28] A. Abdesselam et al. The barrel modules of the atlas semiconductor tracker, 2006. [22](#)
- [29] A. Abdesselam et al. The atlas semiconductor tracker end-cap module, 2007. [22](#)
- [30] F. Campabadal et al. Beam tests of atlas sct silicon strip detector modules, 2005. [22](#)
- [31] K. Romaniouk et al. Trt drift tubes, 2008. [23](#)
- [32] ATLAS Collaboration. Liquid argon calorimeter technical design report. CERN/LHCC/96-041, 1996. [24](#), [66](#)
- [33] ATLAS Collaboration. Tile calorimeter technical design report. CERN/11205 LHCC/96-042, 1996. [26](#)
- [34] A. Artamonov et al. The atlas forward calorimeters, 2007. [27](#)
- [35] ATLAS Muon Collaboration. Atlas muon spectrometer technical design report. CERN/LHCC/97-22, 1997. [28](#), [29](#)
- [36] ATLAS Collaboration. Magnet system technical design report. CERN/LHCC/97-18, 1997. [30](#)
- [37] A. Yamamoto et al. The atlas central solenoid, 2008. [30](#)

-
- [38] ATLAS Collaboration. Central solenoid technical design report. CERN/LHCC/97-21, 1997. 30
- [39] A. Dudarev et al. Construction of the atlas toroid magnet system, 2008. 30, 31, 47
- [40] ATLAS Collaboration. Barrel toroid technical design report, 1997. 30
- [41] ATLAS Collaboration. End-cap toroid technical design report, 1997. 30
- [42] A. Yamamoto et al. Progress in the atlas central solenoid, 2000. 30
- [43] Central Trigger Groups. The central trigger system of the atlas first level trigger, 2008. 31
- [44] ATLAS Collaboration. High-Level Trigger, Data Acquisition and Controls Technical Design Report, 2003. 31
- [45] ATLAS Collaboration. ATLAS Computing Technical Design Report, ATLAS TDR. CERN-LHCC-2005-022, 2005. 33
- [46] G. Barrand et al. GAUDI - A software architecture and framework for building HEP data processing applications, 2001. 33
- [47] T. Cornelissen et al. Concepts, Design and Implementation of the ATLAS New Tracking (NEWT). 34, 35, 36
- [48] ATLAS Collaboration. The global χ^2 fitter in atlas. CHEP'07. Journal of Physics: Conference Series 119 (2008) 032013. 35
- [49] A. Salzburger et al. The atlas tracking geometry description. ATL-SOFT-PUB-2007-004; ATL-COM-SOFT-2007-009, 2007. 35
- [50] R. O. Duda and P. E. Hart. Use of the hough transformation to detect lines and curves in pictures. *Commun. ACM*, 15(1):11–15, 1972. 37
- [51] A. Salzburger. The atlas track extrapolation package. ATL-SOFT-PUB-2007-005. 37, 38, 39, 41, 42
- [52] Price P. J. Dormand, J. R. A family of embedded runge-kutta formulae, 1980. 37
- [53] V. L. Highland. Some practical remarks on multiple scattering, 1975. 38
- [54] G. Molière. Theorie der Streuung schneller geladener Teilchen I. Einzelstreuung am abgeschirmten Coulomb-Feld, *Z. Naturforschung 2a*, 1947, and Theorie der Streuung schneller geladener Teilchen II. Mehrfach- und Vielfachstreuung, *Z. Naturforschung 3a*. 38
- [55] W. M. Yao et al. PDG. *Journal of Physics G*. 33. 1. 2006. 40
- [56] H. Bethe. Zur theorie des durchgangs schneller korpuskularstrahlen durch materie, 1930. 39
- [57] W. Lohmann, R. Kopp, and R. Voss. Energy loss of muons in the energy range 1-10 000 gev, 1985. 39
- [58] L.D. Landau. On the energy loss of fast particles by ionisation, 1944. 39

- [59] S. Agostinelli et al. GEANT4: A simulation toolkit. *Nucl. Instrum. Meth.*, A506:250–303, 2003. [40](#)
- [60] J. Boudreau and V. Tsulaia. The geomodel toolkit for detector description. Proc. of CHEP2004, 2004. [40](#)
- [61] S. Hassani et al. A muon identification and combined reconstruction procedure for the ATLAS detector at the LHC using the (MUONBOY, STACO, MuTag) reconstruction packages. *Nucl. Instrum. Meth.*, A572:77–79, 2007. [44](#), [55](#)
- [62] T. Lagouri et al. A muon identification and combined reconstruction procedure for the ATLAS detector at the LHC at CERN. *IEEE Trans. Nucl. Sci.*, 51:3030–3033, 2004. [44](#)
- [63] S. Torbjorn et al. High-energy-physics event generation with pythia 6.1. *Comput. Phys. Commun.*, 135:238–259, 2001. [44](#)
- [64] S. Frixione and B. R. Webber. The mc@nlo event generator, 2002. hep-ph/0207182. [44](#), [80](#)
- [65] G. Corcella et al. Herwig. hep-ph/0210213. [44](#), [80](#)
- [66] D. Adams et al. Atl-soft-2003-007 2003. [44](#)
- [67] K. Nikolopoulos et al. Event-by-event estimate of muon energy loss in ATLAS. *IEEE Trans. Nucl. Sci.*, 54:1792–1796, 2007. [46](#)
- [68] S. Tarem et al. Nuclear Science Symposium Conference Record, 2007. [55](#)
- [69] ATLAS Collaboration. Mutag. <http://indico.cern.ch/getFile.py/access?contribId=9&resId=1&materialId=slides&confId=35502>. [55](#)
- [70] K. Assamagan et al. Muons in the ATLAS Calorimeter: Energy Loss and Muon Tagging, 2008. [59](#), [62](#)
- [71] S. Baranov et al. Estimation of radiation background, impact on detectors, activation and shielding optimization in atlas. CERN-ATL-GEN-2005-001 (2005). [61](#)
- [72] ATLAS Collaboration. ATLAS tile calorimeter - Technical Design Report ATLAS-TDR-003. CERN-LHCC-96-042, 1996. [62](#)
- [73] ATLAS Collaboration. Atlas liquid-argon calorimeter - technical design report. ATLAS-TDR-002 CERN-LHCC-96-041, 1996. [62](#)
- [74] The LEP ElectroWeak Working Group. "<http://lepewwg.web.cern.ch/LEPEWWG/>". [79](#)
- [75] ATLAS Collaboration. Chapter: Search for the standard model $h \rightarrow 4\ell$ with the atlas detector. , expected performance of the atlas experiment, detector, trigger and physics. CERN-OPEN-2008-020, Geneva, 2008. [79](#)
- [76] B. Kersevan and E. Richter-Was. The monte carlo event generator acermc 2.0 with interfaces to pythia 6.2 and herwig 6.5, 2004. hep-ph/0405247. [80](#)
- [77] J. M. Butterworth et al. Multiparton interactions in photoproduction at hera. *Z.Phys.C72:637-646*,1996. [80](#)

- [78] J. Campbell et al. Production of a z boson and two jets with one heavy quark tag. *Phys. Rev. D*, 73:054007, 2006. [81](#)
- [79] R. Goncalo et al. Overview of the high-level trigger electron and photon selection for the atlas experiment at lhc. CERN-ATL-DAQ-CONF-2005-036. [83](#)
- [80] A. Sidoti et al. The atlas muon trigger slice, 2007. ATLAS Note ATL-PUB-MUON-2007-005. [83](#)
- [81] ATLAS Collaboration. Chapter: Electron identification. expected performance of the atlas experiment, detector, trigger and physics. CERN-OPEN-2008-020, Geneva, 2008. [84](#), [100](#)

SUMMARY

The Standard Model of particle physics is one of the most successful theories in physics. Almost all of its predictions have been confirmed experimentally. It describes three of the four known fundamental interactions of elementary particles, grouping together two major quantum field theories: electroweak and Quantum Chromodynamics. These are field theories which are consistent with both special relativity and quantum mechanics. The mechanism known as *spontaneous symmetry breaking*, which allows particles to acquire mass, is central to the theory. This mechanism introduces a new particle called the Higgs boson and introduces mass terms in the Standard Model Lagrangian. The Higgs is the only particle predicted by the theory not yet discovered. Although the Standard Model does not predict the mass of the Higgs boson itself, there is both experimental and theoretical evidence suggesting that its mass should lie in the range of $114 < m_H < 144 \text{ GeV}/c^2$, with a strong theoretical limit at $1 \text{ TeV}/c^2$.

The Large Hadron Collider and its detectors constitute the world's largest high energy physics experiment. It will collide beams of protons (and heavy ions) that will be accelerated in opposite directions. It will provide proton-proton collisions with a centre of mass energy of 14 TeV and an instant luminosity of $10^{34} \text{ cm}^{-2} \text{ s}^{-1}$. 1232 superconducting dipole magnets will generate a 8.46 Tesla magnetic field, which will bend the trajectory of the particles keeping the beams inside the tunnel.

The beams will collide at four different points in the tunnel every 25 ns. At each point one of the main LHC experiments is located. ATLAS situated at "point 1", is a general purpose detector that will profit from the large centre of mass energy and high luminosity that will be provided by the LHC experiment. The innermost part is formed by the inner detector tracker, which is used for the reconstruction of tracks belonging to charged particles generated in the collisions. The trajectories will be bent by the magnetic field generated by the superconducting solenoid magnet which surrounds the inner detector. The calorimeter envelopes both the solenoid and the inner tracker. The electromagnetic calorimeter is designed to measure the energies of electrons and photons, whilst the hadronic calorimeter will measure the energy of jets associated to quark or tau decays. Finally, the muon spectrometer will allow high precision measurements of the muon momenta using the bending power of the toroidal magnet system.

One of the most interesting analysis that may contribute to the Higgs discovery in ATLAS is $H \rightarrow ZZ^{(*)} \rightarrow 4\ell$. Here, the Higgs decays into a pair of Z bosons which decay further into two pairs of either electrons or muons. Despite its low production cross section, this channel presents the cleanest signature due to the low background associated to the four leptons final state. In order to perform a good physics analysis on this channel, it is paramount to have good electron and muon reconstruction performance. The muon spectrometer will provide great muon reconstruction, especially in combination with the tracks reconstructed in the inner detector. However, it has hardware limitations which reduce the

reconstruction efficiencies in certain regions. Also, in their way through the calorimeters, muons will lose an average of 3 GeV of energy. Hence, low transverse momentum muons ($p_T = 2 - 5 \text{ GeV}/c$) will cause marginal activity in the spectrometer. The muon *taggers* attempt to recover these muon by matching tracks reconstructed in the inner tracker to segments found in the muon spectrometer.

Alternatively, calorimeter muon taggers use the distinctive energy deposition patterns in the calorimeter to identify muons. These algorithms build discriminants that separate the tracks belonging to isolated muons amongst the tracks reconstructed in the inner detector. Since muons behave as *minimum ionising particles* in the relevant energy range, their interaction with the material in the calorimeter is very weak. However, energy deposition of the muons is well above the electronic noise, which allows their identification.

Algorithms for muon identification in the calorimeters are completely independent of the muon system. They provide an unbiased cross check with the spectrometer results. In addition, these algorithms make the muon identification more robust. Should any of the muon stations malfunction, muon identification in the calorimeter might be the only way to guarantee a good reconstruction efficiency

This thesis introduces the implementation of a calorimeter muon tagger for muon identification in the calorimeters. The algorithm starts by preselecting a subset of the tracks reconstructed in the inner detector. It applies cuts on quantities such as the impact parameter or the minimum number of hits found in each the inner tracker subdetectors. This is done to ensure candidate tracks where generated at the primary vertex. Additionally, it applies cuts in the track isolation and calorimeter isolation parameters. 95% of isolated muons pass this preselection while ensuring a fast execution of the algorithm.

After the preselection is done, all the candidate tracks are extrapolated through each calorimeter sampling. The algorithm collects the energies in the cells crossed by the track and computes the parametrised energy loss in every sampling. It applies veto cuts rejecting tracks with large deposits, which are not consistent with the expected values for muons. Pions and other hadrons typically lose large amounts of energy in at least one of the hadronic samplings. Also, by vetoing in the EM calorimeter, the algorithm rejects punch-through electrons that arrive at the hadronic calorimeter. Finally, the algorithm applies threshold cuts above the electronic noise to identify the muon tracks, which depend on the length of the section of the calorimeter cell crossed by the track.

The analysis of the $H \rightarrow ZZ^{(*)} \rightarrow 4\ell$ channel is presented as an example of how muon identification in the calorimeters can be used to improve physics analyses with multi-muon final states. The main backgrounds for this channel are the *irreducible* $pp \rightarrow ZZ^{(*)} \rightarrow 4\ell$ and the *reducible*: $pp \rightarrow Zb\bar{b} \rightarrow 4\ell$ and $pp \rightarrow t\bar{t} \rightarrow 4\ell$. In order to reach a good signal over background significance, the following selection criteria can be used:

- The requirement of two lepton pairs of same flavour leptons and opposite charge.
- The application of impact parameter and track isolation cuts.

A final improvement of 14% in the 4μ and 6% in the $2e2\mu$ channels was found. Most of the recovered efficiency lies around $|\eta| < 0.1$. If the contribution of the tagger is limited to this region, an improvement of 10% in the 4μ and 4% in the $2e2\mu$ channels can still be expected, while the added fake rate is negligible.

SAMENVATTING

Het Standaard Model van de deeltjesfysica is een van de meest succesvolle theorieën van de natuurkunde. Vrijwel alle voorspellingen van het model zijn experimenteel bevestigd. Het model beschrijft drie van de vier bekende fundamentele interacties tussen elementaire deeltjes en verenigt twee belangrijke quantum veldentheorieën, die van de electrozwakke wisselwerking en quantum chromodynamica. Centraal in de theorie staat het mechanisme van spontane symmetrie breking, waardoor deeltjes een massa kunnen krijgen. Dit mechanisme introduceert een nieuw deeltje, het Higgs boson en daarmee massa termen in de Lagrangiaan van het Standaard Model. Het Higgs deeltje is het enige deeltje van de theorie wat nog niet ontdekt is. Alhoewel het Standaard Model de massa van het Higgs deeltje niet voorspelt, kunnen we uit theoretisch en experimenteel bewijs verwachten dat de massa zich moet bevinden tussen $114 < m_H < 144 \text{ GeV}/c^2$, met een harde bovengrens aan de massa van $1 \text{ TeV}/c^2$.

De Large Hadron Collider met de bijbehorende detectoren vormen het grootste deeltjesfysica experiment ter wereld. In de LHC zullen bundels protonen (en zware ionen) in tegengestelde richting versneld worden en botsen. De proton-proton botsingen zullen bij een zwaartepuntsenergie van 14 TeV plaatsvinden en met een luminositeit van $10^{34} \text{ cm}^{-2} \text{ s}^{-1}$. 1232 supergeleidende dipool magneten zullen een veld van 8.46 Tesla genereren om de deeltjes binnen de tunnel om te buigen.

De bundels zullen iedere 25 ns op vier verschillende plaatsen in de tunnel botsen. Op ieder punt staat een van de LHC experimenten. ATLAS, de detector in “point 1” is een algemene detector die gebruik zal maken van de hoge botsingsenergie en luminositeit van de LHC. Het binnenste deel van ATLAS bestaat uit de inner detector die gebruikt wordt voor de reconstructie van geladen sporen die uit de botsingen komen. De sporen worden afgebogen in het veld van een supergeleidende solenoïde magneet, die zich om de inner detector bevindt. De calorimeter omringt de solenoïde en innerdetector. De electromagnetische calorimeter meet de energie van electronen en fotonen, terwijl de hadronische calorimeter de energie van jets afkomstig van quarks of het verval van taus. De muon spectrometer tenslotte maakt een precisie meting van de momenta van muonen mogelijk door de buiging in een toroïde magneet systeem.

Een van de meest interessante metingen die kan bijdragen aan de ontdekking van het Higgs deeltje is $H \rightarrow ZZ^{(*)} \rightarrow 4\ell$. Het Higgs deeltje vervalt hierbij in een paar Z bosonen, die ieder op hun beurt in een paar muonen of electronen vervallen. Ondanks de lage werkzame doorsnede voor dit proces, is het het schoonste kanaal dankzij de lage achtergrond in de vier lepton eindtoestand. Voor deze analyse is een goede electron en muon reconstructie essentieel. De muon spectrometer levert een uitstekende muon reconstructie, zeker in combinatie met sporen uit de inner detector. Er zijn echter delen van de detector waar het muon systeem niet voldoende dekking biedt voor een efficiënte reconstructie. Ook is het zo dat muonen gemiddeld 3 GeV energie in de calorimeters verliezen. Daardoor

zullen veel muonen met laag transvers momentum ($p_T = 2 - 5 \text{ GeV}/c$) geen of slechts een marginaal signaal in de muon spectrometer geven. Muon taggers proberen deze muonen toch te identificeren door sporen uit de inner detector aan segmenten in de muon spectrometer te koppelen.

Als alternatief gebruiken calorimeter muon taggers het typische energiepatroon van muonen in de calorimeter om ze te identificeren. Deze algoritmen selecteren sporen van geïsoleerde muonen uit de sporen die in de inner detector gevonden zijn. Muonen van deze energie gedragen zich als minimaal ioniserender deeltjes (mips) en hebben slecht weinig interactie met het materiaal van de calorimeter. Ze laten echter wel genoeg energie achter om duidelijk zichtbaar te zijn tussen de elektronische ruis, en kunnen op deze manier geïdentificeerd worden.

Algoritmen voor het vinden van muonen met de calorimeter zijn volledig ontkoppeld van het muon systeem. Ze vormen een onafhankelijke validatie van de resultaten van de muon spectrometer. Daarnaast maken zij de muon reconstructie meer robuust. Indien een van de muon detectoren uitvalt, zou muon reconstructie in de calorimeter de enige manier zijn om de algehele efficiëntie op peil te houden.

Dit proefschrift beschrijft een implementatie van een calorimeter muon tagger. Het algoritme begint met de selectie van een aantal sporen in de inner detector. Het selecteert hier op grootheden als de impact parameter van het spoor of een minimaal aantal hits in de diverse onderdelen van de inner detector. Op deze wijze worden alleen kandidaat sporen uit de primaire vertex gekozen. Vervolgens wordt een minimale isolatie van het spoor ten opzichte van andere sporen en energiedeposities in de calorimeter geëist. Met dit snelle algoritme wordt 95% van de geïsoleerde muonen gevonden.

Na deze voorslectie worden de sporen geëxtrapoleerd door de lagen van de calorimeter. Het algoritme houdt de energie in de cellen rond het spoor bij en berekent ook het verwachte energieverlies. Sporen met grote energiedeposities worden verworpen omdat deze niet overeenkomen met de verwachting voor muonen. Pionen en andere hadronen laten over het algemeen een grote hoeveelheid energie achter in tenminste een van de lagen van de hadronische calorimeter. Electronen die de hadronische calorimeter bereiken laten veel energie in de electromagnetische calorimeter en worden ook verworpen. Tenslotte selecteert het algoritme energiedeposities die duidelijk boven het ruisniveau liggen en afkomstig van muonen zijn. De minimale waarde is afhankelijk van de lengte van het spoor in de calorimeter cel.

De analyse van het $H \rightarrow ZZ^{(*)} \rightarrow 4\ell$ kanaal is een voorbeeld van hoe muon identificatie in de calorimeter kan bijdragen tot verbetering van een analyse met meerdere muonen in de eindtoestand. De belangrijkste achtergronden voor dit kanaal zijn het irreduceerbare $pp \rightarrow ZZ^{(*)} \rightarrow 4\ell$ kanaal en de reduceerbare $pp \rightarrow Zb\bar{b} \rightarrow 4\ell$ en $pp \rightarrow t\bar{t} \rightarrow 4\ell$ kanalen. Om een duidelijk signaal boven de achtergrond te krijgen, kunnen we de volgende snedes maken:

- Twee lepton paren van hetzelfde type en tegengestelde elektrische lading.
- Eisen aan de impact parameters en de isolatie van de sporen.

Een verbetering van 14% in het vier muon kanaal en van 6% in het twee muon, twee electron kanaal wordt bereikt. De grootste winst in efficiëntie is voor $|\eta| < 0.1$. Wanneer wij het gebruik van de tagger tot dit gebied beperken, zien wij een verbetering van 10% voor het vier muon en 4% voor het twee muon, twee electron kanaal. De toename in de achtergrond is in dit geval te verwaarlozen.

ACKNOWLEDGEMENTS

First of all I would like to thank both Nicolo de Groot and Sijbrand de Jong for giving me the opportunity to join the department of High Energy Physics at Radboud. It has been a life changing experience and I can honestly say that I have grown both at a personal and professional level. Special thanks to Peter Kluit whose guidance and advice have made this research possible.

I would also like to thank the department's secretariat team: Anelies, Marjo and Gemma; who made all the administrative obstacles much smoother. Thanks as well to the rest of the department that were always open to questions and discussions. Also thanks to Peter Klok for your friendship and those memorable runs!

I'll always remember the first year in Nijmegen sharing the office with three great office mates Qin, Tamas and Miran. I will always miss those fascinating chats about politics, economy and life in general (everything but physics really!) What about those ping-pong games that made the best coffee breaks! Also thanks to my friends at the *Wasps* rugby club in Nijmegen, as well as Juanjo, Carmen, Javier, Lara and (more recently) Miguel and Ana for making my life in The Netherlands much more enjoyable.

The time I spent at CERN marked me deeply as a scientist, being surrounded by such outstanding people was an amazing experience from which I tried to squeeze as much as I possibly could. Jochem, my personal Athena tutor, I cannot thank you enough for the time you spent helping me, but above all, for being a good friend. Zdenko and Aras, who reminded us that there is more to life than working long hours every day. I was also very lucky to share my days at CERN with the Nikhef crowd: Eric, Alex and the adopted Carolina and Nicola.

Papá, Mamá, gracias por vuestro apoyo. Para mí ambos sois dos espejos de honestidad en los que algún día me gustaría verme reflejado. Y Carla, mi hermana pequeña, tu dedicación, rectitud y voluntad de trabajo siempre son una fuente de inspiración. And of course thanks to my lovely Caroline for all your patience and love: Tú eres la luz que guía mis pasos.

CURRICULUM VITAE

Gustavo Ordóñez Sanz was born on July 2nd 1978 in Madrid and grew up in Majadahonda where he went to primary and secondary schools. He did his first year of Chemistry at Complutense University of Madrid before moving to the Autonomous University of Madrid to study Physics. In his last year he studied at the Superior Institute of Technology in Lisbon as an Erasmus student. In 2002 he obtained his degree in Theoretical Physics. He began his professional career in the field of Material Science R&D. In 2003 he was offered a Research Scholarship in High Energy Physics at LIP in Lisbon. Later, he briefly worked as an IT consultant in Madrid. In November 2004 he joined the Radboud University in Nijmegen to work as a junior researcher on the ATLAS experiment. Currently he works as a Quantitative Analyst in the financial sector.

